A Model and Performance Based Analysis of $Cu/CeO_2/ZrO_2$ for Methanol Synthesis from Syngas

Shadi Jaber

A Thesis
in
The Department
of
Chemical and Materials Engineering

Presented in Partial Fulfillment of the Requirements

For the Degree of Master of Applied Science (Chemical Engineering) at

Concordia University

Montreal, Quebec, Canada

October 2023

CONCORDIA UNIVERSITY
School of Graduate Studies

This is to certify that the thesis prepared

By: Shadi Jaber

Entitled: A Model and Performance Based Analysis of $Cu/CeO_2/ZrO_2$ for Methanol Synthesis from Syngas

and submitted in partial fulfillment of the requirements for the degree of

Master of Applied Science (Chemical Engineering)

complies with the regulations of the University and meets the accepted standards with respect to originality and quality.

Signed by the final examining committee:

Supervisor, Dr. Melanie Hazlett
Department of Chemical and Materials Engineering

Examiner, Dr. Yaser Khojasteh
Department of Chemical and Materials Engineering

Examiner, Dr. Ivan Kantor
Department of Chemical and Materials Engineering

Approved by

Graduate Program Director, Dr. Sana Jahanshahi Anbuhi

Month day, year: 11/06/2023

Dean, Dr. Mourad Debbabi

Abstract:

A Model and Performance Based Analysis of $Cu/CeO_2/ZrO_2$ for Methanol Synthesis from Syngas

Shadi Jaber

Meeting the ever-increasing energy demands while adhering to strict environmental regulations remains a significant global challenge. Methanol (CH_3OH) is a significant sustainable chemical feedstock resulting from thermo-catalytic CO_2 hydrogenation through heterogeneous catalysis. It serves as a vital fuel for internal combustion engines and fuel cells while also serving as a foundational molecule for the synthesis of various chemicals and sustainable fuels such as Dimethyl ether and biodiesel. The catalytic synthesis of methanol from CO_2 typically requires high temperatures due to the high molecular stability of CO_2. However, although higher temperatures facilitate the activation of CO_2, a significant increase in the unwanted formation of CO through the reverse water-gas shift (RWGS) reaction is enhanced as well, thereby reducing the selectivity of methanol.

This research focuses on the synthesis of methanol from syngas, with specific emphasis on the catalyst type and the associated reaction kinetics and thermodynamics. It explores a novel catalyst, $Cu/CeO_2/ZrO_2$ that exhibits superior performance in terms of methanol yield and selectivity in addition to a delayed crossover temperature, the temperature beyond which the selectivity of CO is higher than that of methanol, when compared to the commercial catalyst $Cu/ZnO/Al_2O_3$. A distinctive aspect of this study is the modification of catalyst kinetics through a set of sensitivity analysis and design specs performed in the ASPEN PLUS V.12 software to align with documented lab and experimental results. This is followed by a scale-up of the chemical process to evaluate the catalyst's performance on an industrial level in comparison to the commercial catalyst currently in use, where the $Cu/CeO_2/ZrO_2$ catalyst prevailed as well in terms of methanol yield and selectivity.

The kinetic model studied is based on a dual-site LHHW adsorption mechanism where CO and CO_2 adsorb competitively on one site (σ_1) and H_2 and H_2O adsorb competitively on a second site (σ_2), with the dissociation of H_2 over metallic cupper. The adsorbed hydrogen preferentially hydrogenates the carbon atom giving rise to the formate route, where methanol can be formed either via the direct route (directly from CO_2) or via the indirect one (CO obtained from the reverse water gas shift, RWGS, reaction). This work also encompasses the diverse formulations of driving force expressions, which are contingent upon the specific rate-determining step of the particular reaction. Additionally, the investigation considers optimal reactor dimensions and conditions for the catalyst's optimal performance and assesses the physical properties of both the new and commercial catalysts and their economic viability within the industry, taking into account factors such as reactor size, temperature, and pressure.

Overall, this research delves into the thermodynamics, kinetics, and reactor design associated with methanol synthesis from syngas, investigating the performance of a newly developed catalyst on an industrial scale, while considering its economic feasibility compared to the existing commercial catalyst.

Acknowledgments

I would like to express my profound gratitude to my supervisor Dr. Melanie Hazlett, who has been an unwavering pillar of support and guidance throughout my Master's journey. Her expertise, patience, and insightful critiques have been invaluable to my academic growth.

I would like to express my deep and heartfelt gratitude for my parents for their unwavering support and unconditional love. Their hard work and persistence in life paved the way for countless opportunities for my siblings and I to pursue whatever we aspire to and I'm forever in their debt. My thanks go out to my brothers as well for being there to share life's ups and downs with and for pushing me to be my better self.

I also would like to extend my thanks to Alireza Lotfollahzade Moghaddam, Azam Movasati, Farah Mufarrij and Mourad El Helou for reaching out and offering a helping hand when needed.

Dedication

To my beloved parents,

This thesis stands as a testament to your unwavering love, support, and belief in me. Your sacrifices, guidance, and encouragement have been the guiding lights in my journey, illuminating the path towards achieving this milestone. Your example has taught me resilience, perseverance, and the value of hard work. This accomplishment is not just my own, but a reflection of your enduring faith in my potential and the strength of your unconditional love. I dedicate this work to you, with all my love and gratitude, as a symbol of my appreciation for everything you have done for me.

Thank you for being my pillars of strength and my greatest inspirations.

Table of Contents

List of Figures

List of Tables

List of Symbols

Symbol	Definition
K_c	Equilibrium constant based on concentrations
K_{eq}	Equilibrium constant based on partial pressures
K_i ; b_i	Adsorption equilibrium constant
k_r	Reaction rate constant
k_A	Adsorption rate constant of substance A
k_{-A}	Desorption rate constant of substance A
k_j example: k_1, k_2, k_3 driving force	Specific rate constant of reaction
r_{Rxn}	Rate of reaction
r_{AD}	Rate of adsorption
r_{-i}	Rate of detachment
$-r_i$	Rate of disappearance
σ_j; s_j	Adsorption site
ϑ_V	Vacant site
P_A	Partial pressure
ΔC_p	Heat capacity
[A]	Concentration of substance A
W	Catalyst weight
V	Reactor volume
A	Reactor area
ρ	Apparent density
LP	Low pressure
MP	Medium pressure
HP	High pressure

CHAPTER 1: INTRODUCTION

Energy is a primary requirement for our civilization to support economic and social progress and enable a high quality of life. The global population continues to increase, and with it the standard of living, leading to an increase in energy demand in most countries. These countries heavily rely on fossil fuels such as coal, natural gas, and petroleum, which accounts for 82% of global energy [1], [2], as an easily accessible and a cheap source to supply their demand. These non-renewable fuels, release a lot of carbon dioxide,(CO_2) , and other pollutants into the atmosphere upon combustion (e.g. carbon monoxide or CO, and nitrogen oxides or NO_x) [3]. Substantial physical evidence demonstrates that CO_2 is the single most important climate-relevant greenhouse gas (GHG) in Earth's atmosphere [4]. This is because unlike water vapor, CO_2 does not condense and precipitate from the atmosphere at current climate temperatures. Noncondensing greenhouse gases make up 25% of the total terrestrial greenhouse effect, where CO_2 accounts for 20% by itself, while the other 5% are from minor GHGs and aerosols such as O_3, N_2O, CH_4 and chlorofluorocarbons. These non-condensing gases play a vital role in maintaining a stable temperature structure which in turn sustains the current levels of atmospheric water vapor and clouds that account for the remaining 75% of the greenhouse effect.

The continuing increase in CO_2 levels due to human activities and excess burning of fossil fuels will lead to substantial and irreversible changes to the world's climate [4], [5]. Transportation and energy sectors are considered major air pollution sources as they still heavily rely on fossil fuels to satisfy their needs [6]. Based on the Intergovernmental Panel on Climate Change (IPCC) 50% of the net global GHG emissions is attributed to the energy and transport sectors alone [7]. In order to mitigate the harmful effects of high CO_2 emissions and adhere to environmental regulation, countries have turned to carbon capture and storage(CCS), in addition to carbon capture and utilization(CCU), or both (CCUS) [8].

It has been claimed that the selective removal, capture, of CO_2 from industrial gas streams can be accomplished via membrane separations, chemical absorption on solvents, physical adsorption on zeolites, solid amines, and metal-organic frameworks (MOF) [9]. The CO_2 captured can then be transported for geological storage, or for CO_2 utilization. However, in the light of the increasing demand for energy, green fuels are being searched intensively to limit the dependency of fossil fuels [10], and perhaps the best use of the captured CO_2 would be transforming it to high value energy products.

Methanol, CH_3OH, is one of the target fuels identified by the Co-Optima initiative for use in internal combustion engines and fuel cells [11]. As a renewable fuel, it is formed from the chemical recycling of carbon dioxide from natural and industrial resources over multi-component catalyst in which both metal and oxide phases are present [3], [12]. Furthermore, methanol is also an alternative building block to produce chemicals, olefins (ethylene and propylene) and subsequently any derived hydrocarbon product. Finally, dimethyl ether (DME) which is one of the most promising clean burning fuels for a wide range of applications, is produced by the bimolecular dehydration of methanol. Such versatile uses for methanol explains the significant increase in market demand from 6% in 2011 to 22% in 2016 [5].

Numerous catalysts have been researched and tested in the area of CO_2 hydrogenation to methanol. These studies proved that Cu-based catalysts are the most suitable for methanol synthesis as they provide the necessary active site for the CO_2 conversion to take place. However, not all the catalysts share the same performance in terms of stability, methanol selectivity and methanol yield.

The objective of this thesis is to evaluate the performance of a novel $CuO/ZrO_2/CeO_2$ catalyst reported in the literature and compare its performance to the industrially used $CuO/ZnO/Al_2O_3$ catalyst for methanol synthesis, particularly looking at CO_2 rich inlet streams for renewable methanol production. To accomplish this, the kinetics of a new catalyst $CuO/ZrO_2/CeO_2$ for the CO_2 hydrogenation to methanol was modeled and simulated using the Aspen Plus software. Next, a comparison is conducted between both catalysts based on their performance on an industrial level which is done in a simulation environment using Aspen Plus.

The contents of this thesis are divided into 5 chapters as follows:

The first chapter of this thesis is the introduction.

The second chapter covers a literature review done on both the commercial $CuO/ZnO/Al_2O_3$ catalyst, and the novel $CuO/ CeO_2 /ZrO_2$ catalyst for the methanol synthesis process while showcasing recent developments in this area. Particularly, methanol is discussed as a potential renewable energy source and product for carbon utilization. The thermodynamics of methanol synthesis are briefly reviewed. The main focus of the review is on catalysts for methanol synthesis, mainly on copper-based catalysts including the commercial $CuO/ZnO/Al_2O_3$ catalyst, and the novel $CuO/CeO_2/ ZrO_2$ catalyst. The activity and mechanism for CO_2 hydrogenation for these catalysts are highlighted and further the structural and chemical properties contributing to the activity are discussed.

In the third chapter, the model development methodologies are detailed. Particularly, the thermodynamic modeling of CO_2 conversion to methanol is presented. Some background on kinetic rate laws and intrinsic kinetics for catalytic reactions is outlined, and their application to methanol synthesis. Details of how the kinetic model for the new catalyst was implemented in Aspen Plus is given, and how the kinetics were varied to match the experimental results from literature.

The fourth chapter goes over the results and discussion. Specifically, the kinetic model validation is showcased, and the performance of the commercial $CuO/ZnO/Al_2O_3$ and $CuO/CeO_2/ZrO_2$ are compared on an industrial level via an Aspen Plus simulation. Furthermore, an energy and economical analysis is done to demonstrate the saving incurred from using $CuO/CeO_2/ZrO_2$ over the commercial catalyst.

The fifth chapter outlines the conclusions of this thesis and future recommendations.

CHAPTER 2: LITERATURE REVIEW

2.1 Methanol as an alternative energy source

2.1.1 Energy consumption trends and CO_2 emissions

Energy and the environment are two of the most pressing challenges facing the world today, where the need to satisfy the high demand for energy while abiding with the environmental regulations has always been contradictory. Countries have long depended on fossil fuels as a source of energy since the industrial revolution, continuing to this day. For instance, the construction of the steam engine and its popular operations caused a rapid increase in coal demand and consumption. Next, the development of the internal combustion engine and automobile manufacturing technologies promoted the development of the petroleum and chemical industry as the need to refine gasoline for the use in those engines grew. As a consequence of the rapid growth of established industries and the expansion of emergent sectors, natural resource consumption increased dramatically, and the development of such resources was significantly intensified [13]. Throughout this long industrialization period greenhouse gases such as CO_2 were emitted without much governance, leading to environmental problems such global warming and ecological degradation. It wasn't until 2015, that the United Nation Climate Change Conference adopted the Paris Agreement pledging to cut greenhouse gas emissions and reduce the risks and impacts of climate change by maintaining the increase in the global average temperature to well below 2°C above pre-industrial levels [14].

Figure 1(a-b) demonstrates the global primary energy consumption trends by source over the past 5 decades. As shown in Figure 1-a, fossil fuels like coal, oil, and natural gas have long been and still are to this day the main sources of energy given that they are simple to extract and have a significant amount of energy. Even though there is an increasing trend in energy consumption from other green sources such as biofuels, wind, solar, nuclear and hydropower, it's still not even close to the energy consumption trends of fossil fuels. Figure 1-b shows the catastrophic total energy consumption growth from around 66,429 TWh (terawatt-hour) in 1970 to 177,057 TWh in 2021 according to statistical data estimated from the Energy Institute Statistical Review of World Energy [15]. Growing energy consumption makes it more difficult to shift our energy systems away from fossil fuels and towards low-carbon alternatives. This is because new low-carbon energy must not only cater to this growing demand but also replace the current fossil fuels sources in our energy mix.

a)

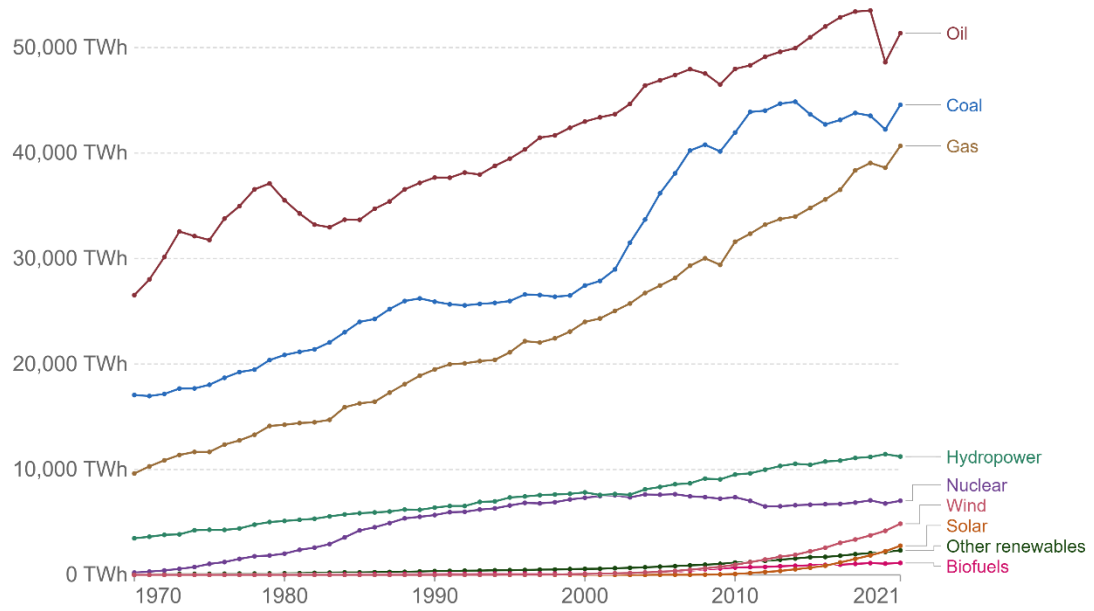

b)

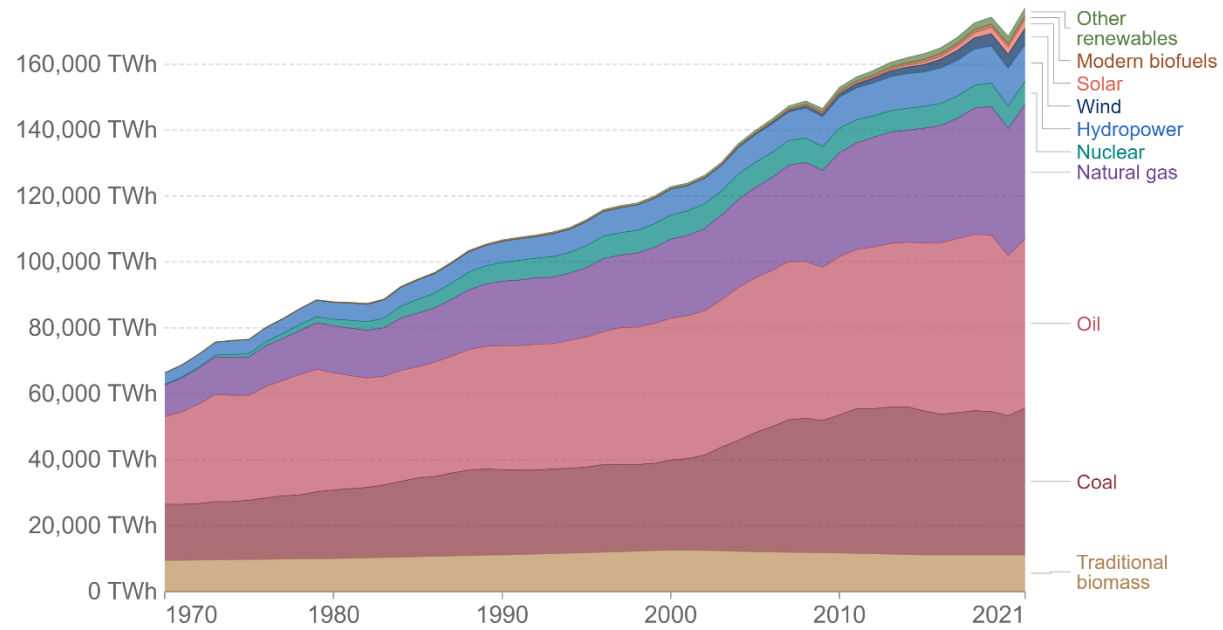

Figure 1-a)Primary global energy consumption by source b) Total global energy consumption by source [1]

As global and national energy systems have transitioned over centuries and decades, the contribution of different fuel sources to CO_2 emissions has changed accordingly. Figure 2 below breaks the absolute and relative contribution of CO_2 emissions by source, into oil, coal, gas, flaring, and cement production. CO_2 emissions from solid and liquid fuel dominate with 14.98 and 11.84 billion tonnes of CO_2 being released from coal and oil consumption in 2021 alone. The contribution from gas production in 2021 was also

notable as well with 7.92 tonnes being released. The contribution of cement or flaring remain low at a comparably global level. Such high and increasing amount of CO_2 emissions each year contribute to air pollution and climate change and promote global warming.

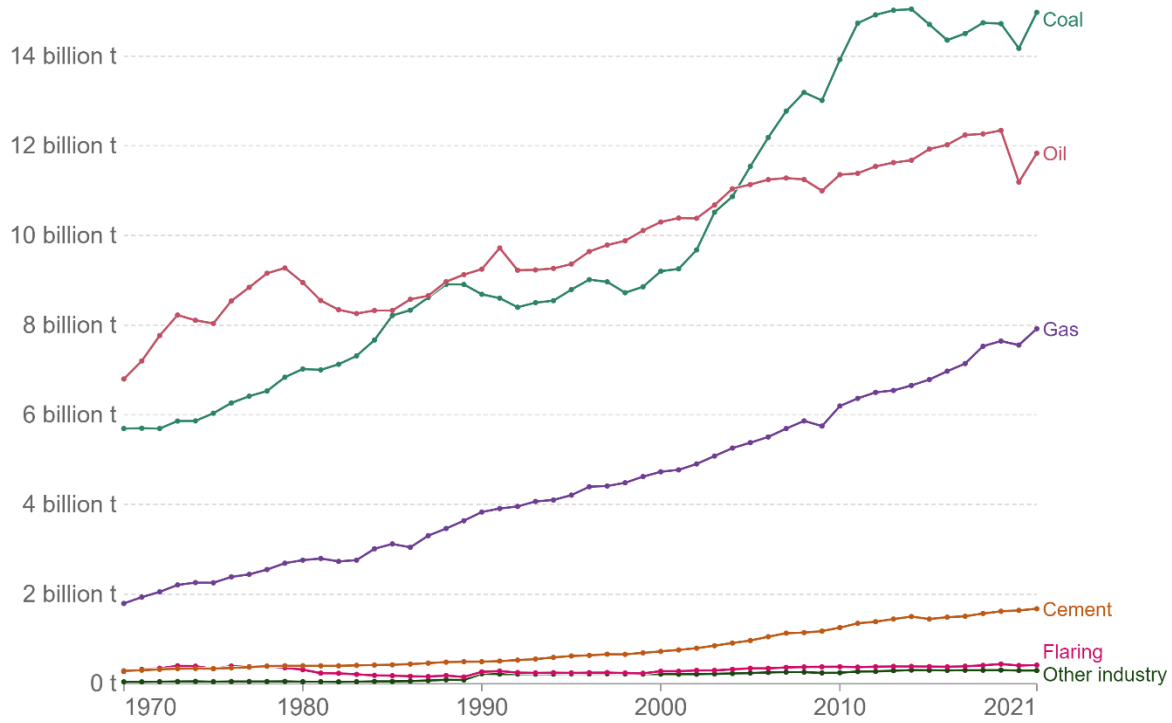

Figure 2-Global CO_2 emission by fuel and industry [16]

It's essential to explore all viable alternative green energy options if a shift from CO_2 emitting fuels is to take place. While hydro and geothermal energy are employed in suitable geographical locations, significant new sources are limited. Furthermore, solar and wind energy hold a great potential and are being increasingly utilized, however their widespread adoption to a degree that would replace fossil fuels is extremely unlikely. Hydrogen (H_2) is another source of energy that burns clean and is produced from water electrolysis, a process that does not produce CO_2 nor involve a source of fossil fuel. However, due to hydrogen's volatile nature (boiling point = -253℃), it should be handled and transported using extreme safety measures rendering it's use to store energy and acting as a fuel inconvenient [17].

CO_2 capture and utilization has emerged as one of the most attractive solutions to mitigate global warming caused by the rising atmospheric CO_2 concentration while offering an alternative energy source to satisfy the global energy demand. Carbon capture can provide low-carbon heat and power, reduce emissions from industries, and enable the extraction of CO_2 from the atmosphere, thus helping to address climate concerns.

2.1.2 CO_2 capture and storage

CO_2 capture technologies have been heavily studied and researched in an attempt to cut back on CO_2 emissions. For instance, Amine scrubbing is a well-developed technology for post-combustion CO_2 capture [18]. It relies on thermal swing regeneration and uses chemical solvents, such as amines, to absorb CO_2 from flue gas. The temperature of the stripper controls the effect of the thermal swing, but it is limited by the thermal degradation of the amine [19] which can result in solvent loss, equipment corrosion and generation of volatile degradation compounds. Piperazine derivatives have shown faster absorption rates and greater resistance to thermal degradation, making them promising solvents for CO_2 capture [19], [20].

Adsorption-based capture technologies emerged as a potential to reduce energy penalties and equipment costs compared to amine-based solvent capture processes. These techniques involve the interaction and bonding of CO_2 molecules with adsorbent materials such as molecular sieves, calcium oxides, zeolites, and activated carbon [21]. Hybrid adsorbents, obtained through the loading of amines onto porous materials, aim to improve selectivity towards CO_2 while reducing corrosivity and heat-consuming regeneration [18]. The adsorbed CO_2 can then be recovered either by swinging the temperature (TSA) or the pressure (PSA) of the system containing the CO_2- saturated sorbent [21].

The Ca-looping (CaL) technology, which uses CaO based material as sorbents, has recently emerged as a potentially feasible process for post combustion CO_2 capture [22]. Limestone's ($CaCO_3$) low cost, wide availability, and it's role as a precursor to CaO, gives calcium looping an advantage over other technologies [23]. However, CaO sorbent are said to show fast deactivation after multiple carbonation/calcination cycles. High-performance synthetic sorbents are being developed to improve durability and cost-effectiveness. Techniques such as sol-gel synthesis, precipitation, and coating are being explored to enhance CO_2 uptake capacity [24].

Chemical Looping Combustion (CLC) is a high-temperature post combustion CO_2 capture technology which involves both a fuel reactor and an air reactor, with a heterogenous oxygen carrier circulating between them [25]. The oxygen carrier is usually a metal oxide which undergoes reduction to metal while the fuel undergoes oxidation to CO_2 and water which can be easily removed by condensation. The commonly used transition metals are Ni, Cu, Mn, or Fe. The metal is then oxidized in a different stage and re-introduced back in the process. This process generates pure CO_2 without any combustion products thus saving energy consumption for separation [18], [21].

Membrane separation techniques involve the use of selective membranes to separate CO_2 from flue gas or even natural gas. The membrane, which is the most crucial component of this process, is comprised of a composite polymer with a thin selective layer attached to a thicker, non-selective, and inexpensive layer that offers mechanical support to the membrane. Membranes offer compact size, waste-free operation, and lack of a regeneration step. However, challenges such as mass transport phenomena and scalable manufacturing methods need to be addressed for industrial application [18], [21], [26].

These are some of the best CO_2 capture techniques currently being explored, each with its own advantages and challenges. Further research and development are needed to optimize these techniques and make them more cost-effective and scalable for widespread implementation.

2.1.3 CO_2 utilization

Among the CO_2 utilization routes, thermal catalytic conversion (hydrogenation) into fuels and chemicals is the most attractive option [27]. This approach represents a strategy that addresses two goals at once. It has the potential to transform the current linear pattern of carbon usage into a self-sustaining loop, leading to a reduction in CO_2 emissions and consequently the mitigation of climate change, and a decreased

reliance on fossil fuels [27], [28]. When considering potential options for chemical storage, a liquid form is generally more favored than a gaseous one for the majority of applications. Especially within the transportation industry, shifting from energy dense liquid fuels derived from fossil fuels such as gasoline, diesel, and kerosene, to alternative sustainable and renewable liquid fuels is highly desirable. This would permit the use of existing infrastructure with minimal adjustments [27]. Among the available options that meet this criterion, methanol, which is the most basic liquid compound comprising just one carbon atom, can be readily synthesized through the hydrogenation of CO_2 in pure form or even from syngas ($CO/CO_2/H_2$).

Table 1 shows the properties of methanol compared to gasoline and diesel. Methanol holds several advantages, and it has the potential to be used as an energy carrier. Its elevated octane rating makes it an excellent candidate for enhancing or substituting gasoline in internal combustion engines (ICE) [3], [5], [28]–[31]. The octane number can describe fuel performance under low severity conditions (600 revolution per minute (rpm) and 45℃ air temperature), research octane number (RON), or under more severe conditions (900 rpm and 149℃ air temperature), motor octan number (MON) [32]. Furthermore, methanol's larger vaporization heat, and the much better resistance to knock makes it preferable over gasoline for use in compact, turbocharged, high-power-density engines that employ direct injection with stoichiometric combustion [31], [33]. Additionally, methanol can be effectively utilized in modified diesel engines and can power direct methanol fuel cells (DMFC), directly converting methanol's chemical energy into electrical power at ambient temperatures [30], [34].

Table 1-The properties of methanol, gasoline and diesel. Adapted from ref [31]

Fuel Property	Methanol	Gasoline	Diesel
Formula	CH_3OH	C_{5-12}	C_{10-26}
Molecular weight	32	95-120	180-200
Oxygen content	50%	0	0
Stoichiometric air/fuel ratio	6.45	14.6	14.5
Low calorific value (MJ/kg)	19.66	44.5	42.5
High calorific value (MJ/kg)	22.3	46.6	45.8
Freezing point (℃)	−98	−57	−1 to −4
Boiling point (℃)	64.8	30-220	175-360
Flash point (℃)	11	−45	55
Auto-ignition temperature	465	228-470	220-260
Research octane number	108.7	80-98	-
Motor octane number	88.6	81-84	-
Cetane number	3	0-10	40-55
Inflammability limit	6.7-36	1.47-7.6	1.85-8.2
Specific heat (20℃)(kJ/kg K)	2.55	2.3	1.9
Latent heat (kJ/kg)	1109	310	270
Viscosity (20℃) (cP)	0.6	0.29	3.9

Beyond its role as a fuel, methanol is a crucial raw material for multiple chemicals such as formaldehyde, acetic acid, and methyl tert-butyl ether (MTBE) [30], [31], [35]. Through the methanol-to-olefins process (MTO), it can yield light olefins including ethylene and propylene, fundamental components in polymers (particularly polyethylene and polypropylene), in addition to any hydrocarbon or product currently derived from petroleum oil [30], [31], [35]. Furthermore, methanol can even be converted into gasoline through the methanol-to-gasoline (MTG) if needed [30], [34].

Derived from methanol through a simple dehydration process, dimethyl ether (DME) is a gaseous substance that can be conveniently liquefied under moderate pressure, similar to liquefied petroleum gas (LPG) [10], [36], [37]. DME, boasting remarkable qualities as a diesel fuel alternative with a high cetane rating and minimal soot emissions, has garnered substantial attention. It's also a viable replacement for LPG in various applications like heating and cooking [10], [36], [37]. Furthermore, both methanol and DME serve as exceptional fuels for generating electric power in gas turbines [3], [30], [34].

Considerable efforts have been dedicated to addressing the challenge of securing a stable hydrogen supply necessary for the hydrogenation of CO_2. The utilization of renewable energy sources such as solar, wind power, photovoltaic cells, and geothermal power has become imperative for producing H_2 via water electrolysis [5], [8]. Furthermore, water-splitting techniques employing photocatalytic, photoelectrochemical, or alternative photochemical processes have contributed to this progress as well [8]. Other than electrolysis, hydrogen could be obtained from biomass valorization processes including pyrolysis and gasification to produce syngas (a mixture of H_2, CO, and CO_2).

2.2 Methanol Synthesis Thermodynamics

A conversion reaction involving CO_2 as a single reactant can be energy demanding since the CO_2 molecule by itself is chemically and thermodynamically stable [38], [39] ,[12] and thus can't dissociate easily. Upon introducing hydrogen which has a higher Gibbs free energy as a co-reactant, it becomes thermodynamically easier [5]. However, in the absence of a catalyst, the synthesis remains quite difficult and also produces several by-products, and that's why the successful development of active catalysts allowed the CO_2 conversion to high value products such as methanol via hydrogenation to become one of the most promising CCUS processes [39], [40]. 4

Both homogeneous and heterogeneous catalysts have been researched for the CO_2 hydrogenation process. Heterogeneous catalysts are presently employed in the industrial synthesis of methanol from syngas, and they are preferable due to their favorable attributes such as affordability, stability, ease of separation, manageable handling, catalyst reusability, and reactor design [34], [40].

Copper based catalysts have been extensively studied for the CO_2 conversion to methanol, with $Cu/ZnO/Al_2O_3$ being the most studied and currently used catalyst in the industry [5]. Three main reactions, shown below (reactions 1-3), occur on the surface of this catalyst which are the exothermic CO_2 and CO hydrogenation to methanol (CO_2 HYD and CO HYD, respectively), in addition to the endothermic reverse water gas shift reaction (RWGS).

Reaction (1), CO_2 HYD	$CO_2 + 3H_2 = CH_3OH + H_2O$	$\Delta H_{298\,K} = -49.4$ kJ mol^{-1}
Reaction (2), CO HYD	$CO + 2H_2 = CH_3OH$	$\Delta H_{298\,K} = -90.4$ kJ mol^{-1}
Reaction (3), RWGS	$CO_2 + H_2 = CO + H_2O$	$\Delta H_{298\,K} = +41.0$ kJ mol^{-1}

As the catalytic hydrogenations of both CO_2 and CO for the production of CH_3OH are exothermic, these reactions will have higher equilibrium conversion for CO_2 and CO at lower temperatures. Additionally, elevated temperatures (100-500 ℃) lead to higher H_2 consumption, triggering the reverse water-gas shift reaction, consequently reducing CH_3OH yield favoring instead CO as a product. Thus, optimal conditions for the hydrogenation process involve elevated pressure and lower temperatures, promoting a more favorable chemical reaction and ultimately increasing the methanol, CH_3OH yield [40], [41].

The effectiveness of CO_2 conversion to CH_3OH relies on the utilization of a suitable catalyst or catalytic setup e.g., reactor type, operating conditions, etc. Challenges in methanol synthesis arise from extreme reaction temperatures to get suitable catalyst kinetics, resulting in inadequate product selectivity upon thermodynamic conversion. Further different catalysts may be more selective towards the desired product, methanol, while many catalysts allow production of both methanol and carbon monoxide through their reaction mechanisms. These factors hinder the heterogeneous CO_2 reduction process. Progress in understanding reaction mechanisms, active site structures, and advancements in catalyst preparation significantly drive catalyst development for selective methanol production.

2.3 Catalysts for Methanol Synthesis

The ideal catalyst for CO_2 hydrogenation needs to exhibit three specific capabilities: (i) the capacity to adsorb and activate CO_2, stabilizing active intermediates for methanol production rather than the RWGS reaction to form CO, (ii) the ability to break down the H-H bond within H_2, facilitating its interaction with intermediates for methanol synthesis, and (iii) the capability to counteract the deactivation from water adsorption on active sites [42].

2.3.1 Cu-based catalysts

Copper-containing catalysts have been thoroughly investigated for CO_2 transformation to methanol using thermal catalysis, with research in this field remaining active. Substantial focus is placed on (i) identifying the active sites, (ii) establishing the connection between catalytic structure and activity, and (iii) enhancing the understanding of reaction mechanisms [5].

Experimental findings backing metallic copper's (Cu) role as the active site stem from investigations on specific crystal orientations such as Cu(100), Cu(110), and polycrystalline Cu films exposing Cu(111) facets within. These studies reveal the sensitivity of the reaction to the catalyst's structure and display turnover frequencies (TOF) for methanol synthesis relating to those observed with industrial catalysts [29], [43].

Figure 3 demonstrates the several proposed reaction mechanisms of methanol formation from CO_2 over a Cu-based catalyst. The conversion of CO_2 into methanol via hydrogenation over a Cu-based catalyst was initially thought to proceed through the formate mechanism. Researchers Grabow and Mavrikakis [29] utilized density functional theory (DFT) calculations to explore methanol production on commercially used Cu-based catalysts, particularly focusing on the Cu (111) site within $Cu/ZnO/Al_2O_3$. This investigation employed both CO_2 and CO as reactants to delineate the roles of each component in the process. Subsequently, they constructed a microkinetic model based on the DFT calculations.

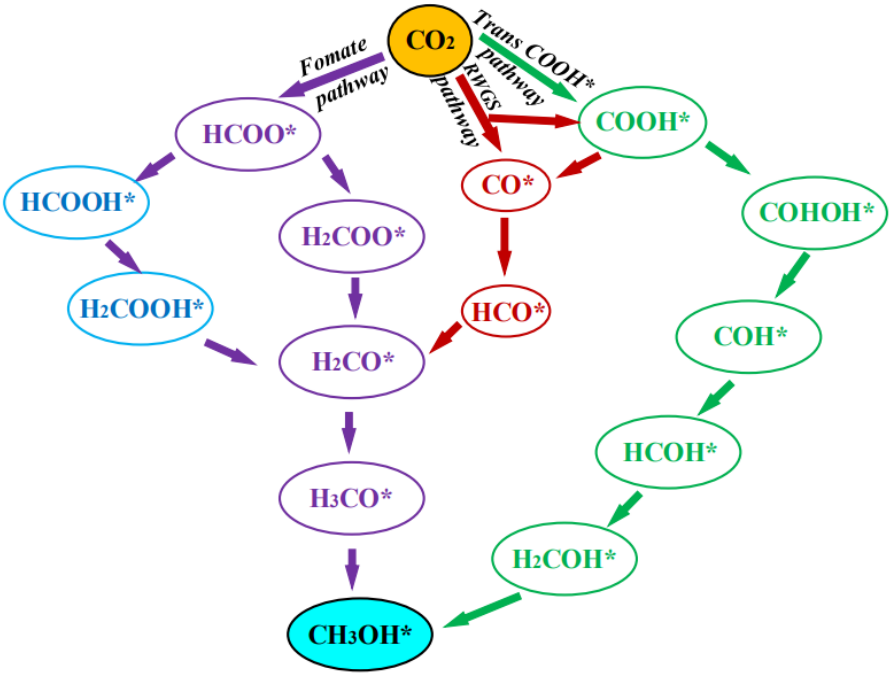

Figure 3-Schematic representation of several proposed reaction mechanism of methanol formation from CO_2. Adapted from ref [44].

Grabow and Mavrikakis [29] considered two possibilities for the formate pathway to take place. They considered an adsorbed HCOO* species where the stepwise hydrogenation takes place at the O atom of the HCOO* leading to formic acid (HCOOH*) formation as in the reaction: $CO_2* \rightarrow HCOO* \rightarrow HCOOH* \rightarrow CH_3O_2* \rightarrow CH_2O* \rightarrow CH_3O* \rightarrow CH_3OH*$. Alternatively, they considered the stepwise hydrogenation of the HCOO* at the C atom leading to dioxymethylene (HCOOH*) formation as in the reaction: $CO_2* \rightarrow HCOO* \rightarrow H_2COO* \rightarrow H_2CO* \rightarrow H_3CO* \rightarrow CH_3O*$ [29]. However, the potential energy surface calculations proved that the hydrogenation of the O atom in $HCOO*$ is both thermodynamically and kinetically preferable over the hydrogenation of the C atom where the $HCOOH*$ product is the more stable one. The rate-determining (RDS) step was determined to be the hydrogenation of CH_3O* for a CO_2-rich feed. However, the formation of CH_3O* serves as the RDS when dealing with a CO-rich feed.

Furthermore, the DFT calculations revealed that CO_2 hydrogenation contributes to around 2/3 of the methanol product. Intriguingly, this outcome contradicted the findings of the potential energy surface (PES) analysis, which suggested that methanol production should be more dominant from CO hydrogenation. This apparent inconsistency can be rationalized by considering the greater exothermic nature of CO hydrogenation compared to CO_2 hydrogenation and the high energy barrier associated with CO_2 hydrogenation, notably the hydrogenation of CH_3O* and the hydrogenation of $OH*$ leading to H_2O* formation. These observations can be linked to the promoting effect of CO on CO_2 hydrogenation. CO* is predominantly utilized in the production of $HCO*$, and it serves as a hydrogen donor, assisting in CO_2 hydrogenation. This phenomenon highlights the complex interplay of reaction pathways influenced by the presence of CO and the intricate balance between exothermicity and energy barriers.

On another note, Zhao et al. [45] emphasized the significant role of water in the process of methanol synthesis stating that the formation of hydrocarboxyl (*trans-COOH**) species on the Cu (111) site becomes more kinetically favored than the formation of formate species in the presence of water. This transformation occurs through a hydrogen transfer mechanism. This intermediate then undergoes a stepwise conversion process, leading to the formation of dihydroxycarbene *(COHOH*)* → hydroxymethylidyne *(COH*)* → hydroxymethylene *(HCOH*)* → hydroxymethyl *(H_2COH*)*, ending in the production of methanol. This finding was validated using both computational and experimental techniques. The DFT calculation highlighted that the decomposition of COHOH* into COH* and OH* constitutes the RDS in this progression.

Furthermore, Higham et al.[43] explored the process of methanol synthesis on alternative Cu catalyst facets, specifically Cu (100) and Cu (110) surfaces using density functional calculations. Their findings suggest that these two facets demonstrate enhanced activation of CO_2 when compared to Cu (111). Methanol synthesis is conceivable through the involvement of *HCOO** and *COOH** intermediates. Moreover, the barrier energy for the initial hydrogenation step on these facets demonstrates notably lower values, indicating enhanced catalytic performance in terms of CO_2 dissociation and hydrogenation.

An agreement between all three low index facets is observed with regards to methanol formation, with *CH_2OH** hydrogenation being less kinetically demanding and more exothermic than the corresponding process for *CH_3O**. Hence, it appears that the overall hydrogenation activity does have similarities for all three surfaces.

2.3.2 Cu based catalyst support:

The support for copper-based catalysts is of extreme significance and interest in the research community. These supports serve to enhance the dispersion of active metal, Cu, where Cu is reduced to form Cu^0 and Cu^+ predominantly, which are considered pivotal active sites for driving methanol synthesis. This prompts the possibility of the reaction occurring on either one or both of these sites [44]. Furthermore, it has been documented that interactions between the active metal and its support interfacial sites may induce modifications in the catalyst surface's reaction environment, altering aspects such as surface acidity or basicity, as well as oxygen vacancy concentrations, through synergistic interactions with supplementary additives [42], [44].

2.3.2.1 Cu/CeO_2/ZrO_2 (CCZ):

CeO_2-ZrO_2 supported catalysts have attracted attention due to their superior redox property, oxygen storage capacity, and thermal resistance. These catalysts have been studied for various catalytic reactions, including CO oxidation, CO hydrogenation, CO/CO_2 hydrogenation, and CO_2 reforming of methane. They are also used for the purification of vehicle exhaust [46], [47]. Pokrovski et al [48], [49] investigated the effect of Ce addition into zirconia on the activity of CO hydrogenation for Cu/ZrO_2 catalyst. Lee et al. [50] prepared Cu/$Ce_xZr_{1-x}O_2$ catalyst using a two-step precipitation method and used it for syngas hydrogenation to methanol. These studies highlight the potential of CeO_2-ZrO_2 supported catalysts in various catalytic applications.

Shi et al [46] synthesized a $Cu_{30}Ce_{35}Zr_{35}O$ with a CeO_2/ZrO_2 ratio = 1 catalyst by a co-precipitation method. This catalyst was then compared to a Cu-Ce and Cu-Zr mixed oxides in the form of $Cu_{30}Ce_{70}O$ and $Cu_{30}Zr_{70}O$ in addition to other CeO_2/ZrO_2 ratios of $Cu_{30}Ce_xZr_yO$ mixed oxide catalysts prepared using the same method and calcined at 350℃ .

2.3.2.1.2 Catalyst Activity:

The activity of CO_2 hydrogenation over various catalysts was evaluated at T=250℃ and P= 3MPA where the experimental results showed that $Cu_{30}Ce_{35}Zr_{35}O$ displayed the best performance in terms of CO_2 conversion and methanol space time yield (STY) while also showing a high CH_3OH selectivity. For all the binary and ternary catalysts, CH_3OH and CO were the only carbon-containing products at the corresponding experimental condition.

2.3.2.1.3 Structural and textural properties of the catalyst

Scanning electron microscope (SEM) imaging showed that the $Cu_{30}Ce_{35}Zr_{35}O$ catalyst displayed more pores and defects on its surface compared to $Cu_{30}Ce_{70}O$ and $Cu_{30}Zr_{70}O$**.** The X-ray diffraction (XRD) experiments showed that the intensity of CuO peaks in $Cu_{30}Ce_{35}Zr_{35}O$ weakens, indicating a decrease in the crystallization degree of CuO and an increase in the dispersion of CuO [46], [47]. This can be attributed to the larger Brunauer-Emmett-Teller (BET) specific surface area of $Cu_{30}Ce_{35}Zr_{35}O$. Wang et al [47] studied the effect of calcination temperature on the CCZ catalyst along the temperature of 350-500 ℃. The results showed an increase in BET surface area in addition to an increase in dispersion and particle size up to a calcination temperature of 450℃.

After reduction with hydrogen, the CuO phase disappears and the characteristic diffraction peaks of Cu^0 metal appear [46], [47]**.** It is well known that the Cu^0 species play an important role in CO_2 hydrogenation to methanol and thus the higher concentration of Cu^0 species and higher dispersion of Cu^0 are expected to show higher activity in CO_2 hydrogenation to methanol [46], [47], [51]. H_2 reduction however didn't affect the crystalline phases of ZrO_2, CeO_2, and their composite oxides**.** The adsorption/desorption isotherms and pore size distribution curves of the calcined samples shown in Figure 4-a) indicate the presence of mesopores which is evident by the hysteresis formed. The region of multilayer adsorption is formed at $P/P_0 \cong 0.2$ for the ternary catalyst and at $P/P_0 \cong 0.4$ for the two binary catalysts suggests a broader mesopore distribution for the former. Furthermore, Figure 4-b) shows that the ternary catalyst exhibits extra peaks indicating the existence of larger pores compared to the two binary catalysts [46].

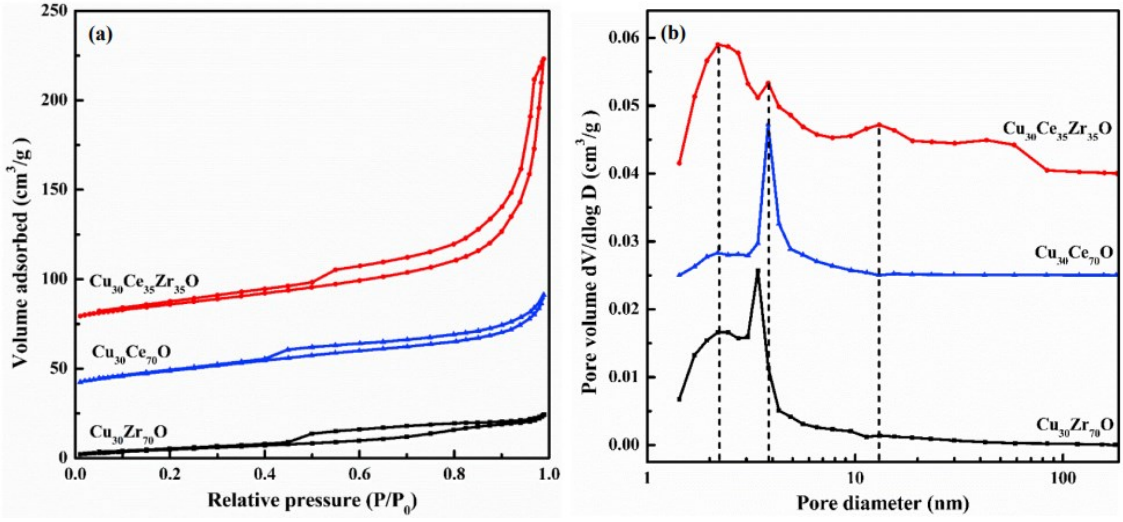

Figure 4- a) Adsorption isotherms b) Pore size distribution curves. Reprinted with permission from ref [46].

2.3.2.1.4 Surface chemical property of the catalyst:

XPS characterization was used to detect the surface chemical states and compositions of the three samples. The peaks for $Cu2p_{3/2}$ and $Cu\ 2p_{1/2}$ indicated the presence of Cu^{2+} species, and the binding energy peak for Cu^{2+} in $Cu_{30}Ce_{70}O$ and $Cu_{30}Ce_{35}Zr_{35}O$ shifts slightly to lower binding energy compared to $Cu_{30}Zr_{70}O$, suggesting enhanced reduction capacity of the catalyst. Surface segregation of CuO occurs in $Cu_{30}Ce_{35}Zr_{35}O$, leading to higher surface CuO contents compared to the bulk CuO content. According to Wang et al., better reducibility is accompanied with the higher ratio of $Cu^0/(Cu^{2+}+Cu^0)$ [47]. Cu^0 species play an important role in CO_2 hydrogenation to methanol and consequently the higher concentration and dispersion of Cu^0 species the higher the catalyst in CO_2 hydrogenation to methanol [46], [47], [50], [51]. Ce 3d core level spectra showed the presence of Ce^{3+} and Ce^{4+} in $Cu_{30}Ce_{35}Zr_{35}O$, and Zr 3d core level spectra confirm the presence of zirconium valence as +4 in $Cu_{30}Zr_{70}O$ and $Cu_{30}Ce_{35}Zr_{35}O$ as reported elsewhere [47], [50], [51].

The O 1s spectra indicates the existence of various types of oxygen species with different chemical states. These results provide insights into the surface chemistry and composition of the catalysts. Two types of O species are observed, low binding energy peak corresponding to lattice O^{2-} and high binding energy peak related to surface O^- species [46], [51]. The low binding energy peak of $Cu_{30}Ce_{70}O$ and $Cu_{30}Ce_{35}Zr_{35}O$ shifts towards a higher binding energy compared to $Cu_{30}Zr_{70}O$, indicating the transfer of bulk lattice O^{2-} to the catalyst surface. The high binding energy shoulder for $Cu_{30}Ce_{70}O$ and $Cu_{30}Ce_{35}Zr_{35}O$ shifts to a higher binding energy compared to $Cu_{30}Zr_{70}O$, suggesting the formation of more OH- groups and oxygen vacancies on the supported metal oxide surfaces [46], [51].

2.3.2.1.5 Reduced $Cu_{30}Ce_{35}Zr_{35}O$ catalyst:

The reduced $Cu_{30}Ce_{35}Zr_{35}O$ catalyst exhibits peaks assigned to $Cu\ 2p_{3/2}$ and $Cu\ 2p_{1/2}$, indicating the presence of Cu^0 species. No satellite peaks are observed, indicating complete reduction of CuO. The chemical states of Ce, Zr, and O show no significant change during the reduction process

The reducibility of the oxide catalysts was investigated and their H_2-temperature programed reduction (TPR) profiles are given. For the TPR test it was determined that the reducibility of $Cu_{30}Ce_{35}Zr_{35}$ and $Cu_{30}Ce_{70}$ are much higher than $Cu_{30}Zr_{70}$ since the reduction peaks occur at lower temperatures. The reduction peaks were attributed to the CuO species, where the CuO content which could be easily reduced in $Cu_{30}Ce_{35}Zr_{35}$ is higher than that of the two binary catalysts. This signifies that more metal Cu active species can participate in the CO_2 hydrogenation reaction.

2.3.2.1.6 Reduction profiles of oxide catalysts:

The H_2-TPR profiles of the oxide catalysts, Figure 5, showed reduction peaks below 500 °C, corresponding to CuO reduction. The profiles can be deconvoluted into two Gaussian peaks, with the low-temperature peak (β) attributed to surface-dispersed CuO reduction or Cu^{2+} ions and the high-temperature peak (γ) associated with bulk CuO reduction [46], [47], [50], [51]. $Cu_{30}Ce_{35}Zr_{35}O$ exhibits two reduction peaks at lower temperatures than the binary catalysts indicating higher reducibility as shown in Figure 5. The reducibility of $Cu_{30}Ce_{35}Zr_{35}O$ is particularly excellent, with peak positions slightly shifting to lower temperatures and a higher content of easily reducible CuO species. This is consistent with the XPS results, suggesting that $Cu_{30}Ce_{35}Zr_{35}O$ can be completely reduced at the temperature used in the study, allowing more metal Cu active species to participate in the CO_2 hydrogenation reaction [46].

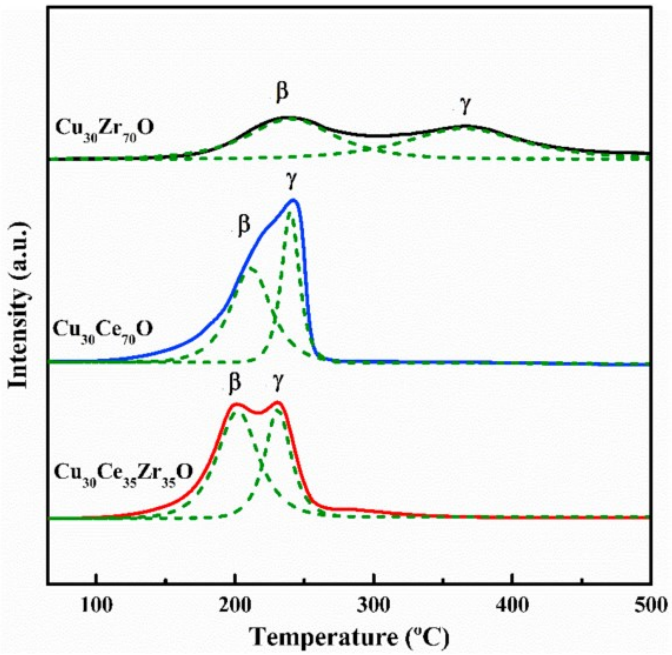

Figure 5-H_2-TPR profiles of the catalysts. The solid curves are experimental curves, and the broken curves are Gaussian multi-peak fitting curves. Reprinted with permission from ref [46].

2.3.2.1.7 Surface Basicity of the catalyst:

The CO_2-temperature programmed desorption (TPD) curves of the reduced catalysts show three peaks representing different types of basic sites: weak, moderate, and strong. The weak basic sites are surface hydroxyl groups, the moderate basic sites are metal-oxygen pairs (M-O), and the strong basic sites are coordinatively unsaturated O^{2-} ions. The catalyst with a higher amount of Zr^{4+} has stronger basic sites, while the catalyst with a higher amount of Ce^{4+} has more weak and moderate basic sites.

2.3.2.1.8 The effects of physicochemical properties on the catalytic performance

Physico-chemical properties of catalysts impacted catalytic performance. $Cu_{30}Zr_{70}O$ had the lowest CO_2 conversion due to larger crystallite size and poorer dispersion of CuO. $Cu_{30}Zr_{70}O$ had fewer external and easily reducible CuO, limiting Cu^0 active species and reducing CO_2 conversion. $Cu_{30}Zr_{70}O$ exhibited the highest CH_3OH selectivity due to maximum strong basic sites and abundant H_2CO adsorption [42], [46]. $Cu_{30}Ce_{70}O$ had better CuO dispersion and higher amount of easily reducible CuO, resulting in higher CO_2 conversion [46], [52], [53].

$Cu_{30}Ce_{35}Zr_{35}O$ showed the highest CO_2 conversion and CH_3OH selectivity due to synergetic effect of Cu_Ce_Zr, highly dispersed CuO species, and incorporation of Zr^{4+} into CeO_2 lattice.

The Cu/ZrO_2-based catalysts for CO_2 hydrogenation involve two active centers: metallic Cu and ZrO_2 support. Cu sites adsorb H_2 and provide H species, while ZrO_2 support adsorbs and activates CO_2 molecules for stepwise hydrogenation to CH_3OH [46], [51]. The reaction mechanism involves adsorption and dissociation of H species on Cu sites, and adsorption and activation of CO_2 molecules on Ce and/or Zr oxide surface sites. $Cu_{30}Ce_{35}Zr_{35}O$ catalyst shows the highest CO_2 conversion and CH_3OH yield due to

more Cu active sites, oxygen vacancies, weak and moderate basic sites, and the introduction of strong basic sites.

2.3.2.1.9 Mechanism Proposed:

In the previous discussion of the mechanism, the Cu phases were responsible for both H_2 dissociation and activation of CO_2 molecules. For this catalyst system, it has been suggested that the Cu sites are still responsible for H_2 dissociative adsorption, while the Ce and/or Zr oxide surface sites are responsible for the adsorption and activation of CO_2 molecules [46], [47]. The adsorbed and dissociated H species then spill over to the adsorbed CO_2, leading to the formation of HCOO. Further hydrogenation of HCOO results in the formation of H_2COO and H_2CO, which can then be hydrogenated to form H_3CO and CH_3OH or dissociate to generate CO.

According to Wang et al [47] two types of formate species (bidentate *bi-HCOO** and monodentate *m-HCOO**) are observed under $CO_2 + H_2$ when active hydrogen (H*) spillover from Cu^0 species takes place. Both of these species can be directly converted into the desired product, CH_3OH, through hydrogenation. However, there is a notable difference in the hydrogenation process: *bi-HCOO** undergoes immediate hydrogenation, while *m-HCOO** first needs to accumulate to a certain concentration before it undergoes the hydrogenation process. These two formate species yield distinct methoxy products upon further hydrogenation. To elaborate, *t-OCH_3* species are predominantly formed from the hydrogenation of *bi-HCOO*, and they can subsequently undergo further hydrogenation to produce CH_3OH, which is the desired end product. Conversely, the *b-OCH_3* species originate from the hydrogenation of *m-HCOO* species and are subsequently further hydrogenated to eventually yield the target product, CH_3OH. It should be noted that the monodentate formate (*m-HCOO**) species are not observed on Cu/CeO_2 and Cu/ZrO_2 ,which indicates that *m-HCOO** species are exclusively bonded on Ce-Zr/Cu-CeZr solid solution. A simple reaction pathway is demonstrated in Figure 6 and can be described as $CO_2 \xrightarrow{H} HCOO \xrightarrow{H} H_2COO \xrightarrow{H} H_2CO \xrightarrow{H} H_3CO \xrightarrow{H} CH_3OH$ [46].

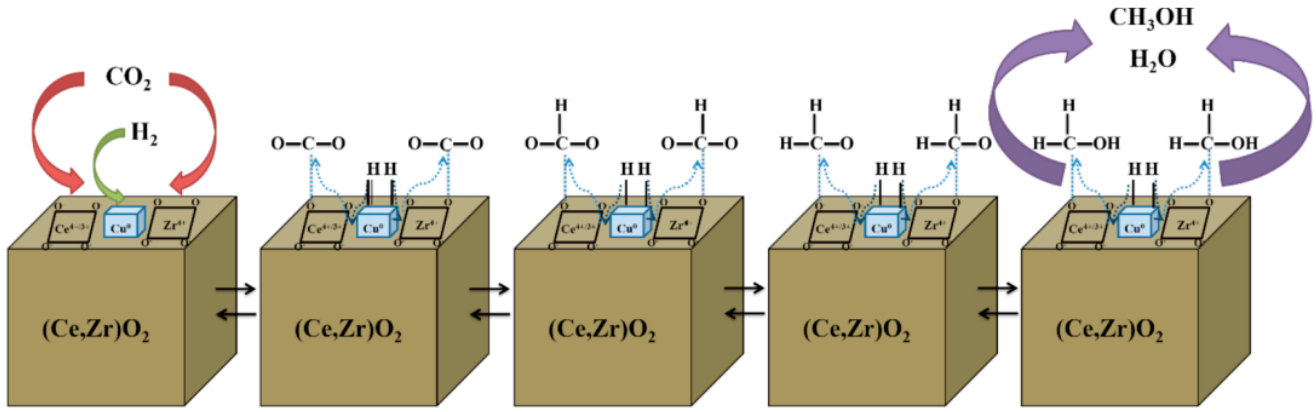

Figure 6-The bifunctional mechanism for CH_3OH synthesis from CO_2 hydrogen over Cu30CexZryO catalysts. Reprinted with permission from ref [46].

2.3.2.1.10 CO hydrogenation to methanol

Pokrovski and Bell [49] performed a study on the factors influencing the activity of $Cu/Ce_xZr_{1-x}O_2$ for methanol synthesis via CO hydrogenation. The reactions were carried out using a total reactant gas flow of 60 cm^3/min (at STP) with a H_2/CO ratio of 3/1 over a 0.15g of catalyst at total pressure of 3.0 MPa.

TPD results showed that the amount of CO adsorbed per unit area increased monotonically with increasing cerium content, whereas the amount of H_2 adsorbed reached a maximum at Ce/Zr = 1. The desorption of H_2 was not accompanied by a release of water which suggests that the hydrogen desorption occurred via the decomposition of surface hydroxyl groups formed on reduction in H_2 as shown in Figure 7 below:

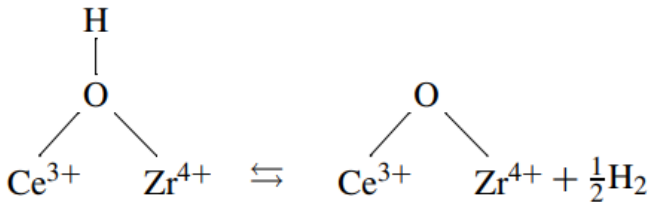

Figure 7-Hydrogen desorption mechanism over Ce/Zr species. Reprinted with permission from ref [49].

The CO conversion to methanol increased over the temperature range of 473–523 K, accompanied by decreased methanol selectivity. The methanol productivity of 3 wt% $Cu/Ce_xZr_{1-x}O_2$ reached a maximum versus Ce content [48]–[50].

The nature of surface species and the dynamics of CO adsorption and hydrogenation were studied using in situ infrared spectroscopy. The infrared spectra of CO adsorbed on $Cu/Ce_x Zr_{1-x}O_2$ showed bands corresponding to different modes of b-HCOO–Zr and CH_3O–Zr species, as well as carbonate and carboxylate species [48], [49]. Other weak bands were assigned to C–O stretching vibrations of terminal (t-OCH_3) and bridged (b-OCH_3) methoxide species on Zr. The formate species absorbed on Ce^{3+} cations were characterized by absorption bands corresponding to bidentate formate species. The increase in Ce content led to an increased intensity of the bands corresponding to bidentate formate and methoxide species.

After CO adsorption, H_2 was introduced to the CO/He mixture with a H_2/CO molar ratio of 3/1 resulting in the occurrence of t-CH_3O and b-CH_3O species on Zr^{4+} and Ce^{3+} cations [49]. The intensities of bands for b-HCOO species decreased, while the intensities of bands for methoxy species, CH_3O, increased with increasing cerium content. Various carbonate and carboxylate species were observed during CO adsorption and hydrogenation. Reduction of formate to methoxide species resulted in the formation of Ce^{4+} species**.**

The relative rates of consumption of formate and methoxide species were evaluated by switching from a CO/H_2 mixture to one containing only H_2. The intensity of the b-HCOO bands decreased more rapidly compared to the bands for methoxide species when the feed was switched , indicating that the RDS of methanol synthesis from H_2/CO was the elimination of surface methoxide species as reported by [48], [54]. The rates of CHOO and CH_3O consumption increased with increasing Ce content up to a maximum at x = 0.5 when Zr/Ce =1. The rate of CHOO hydrogenation to methoxide was higher than the rate of methoxide elimination, regardless of catalyst composition which indicates that the RDS did not change with catalyst composition.

The presence of Ce^{3+}–O(H)–Zr^{4+} species on the oxide surface contributed to increased hydrogen adsorption [49], [50]. The increased adsorption of hydrogen on the surface of $Cu/Ce_xZr_{1-x}O_2$ was attributed to the migration of H atoms spilled over from Cu particles and their reaction with Ce^{4+}–O–Zr^{4+} pairs to form Ce^{3+}–O(H)–Zr^{4+} structures [49], [50] as can be shown in Figure 8 where the oxygen vacancy is represented by a square. The higher concentration of bridging hydroxyl species on the surface of $Ce_xZr_{1-x}O_2$ and the higher Brønsted acidity of Ce^{3+}–O(H)–Zr^{4+} species are believed to be the primary origins of the higher activity of 3 wt% $Cu/Ce_xZr_{1-x}O_2$. The incorporation of Ce cations into the framework of ZrO_2 enhances the adsorption of CO and H_2. The observed maximum in the area-based methanol activity occurs at Zr/Ce = 1 [46], [49], [50].

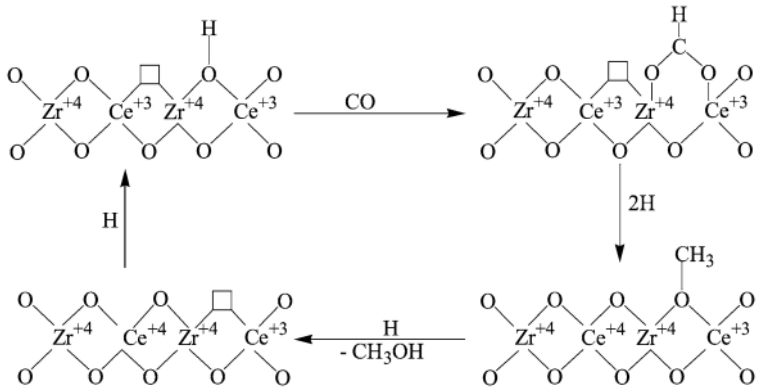

Figure 8-Proposed reaction scheme of CO hydrogenation to methanol on $Cu/Ce_xZr_{1-x}O_2$. Reprinted with permission from ref [49]

Rhodes et al. [54], [55] studied the significant role that the zirconia phase plays in influencing catalyst activity. For instance, $Cu/m\text{-}ZrO_2$ (where $m\text{-}ZrO_2$ represents monoclinic zirconia) has been shown to exhibit much greater activity for methanol synthesis compared to $Cu/t\text{-}ZrO_2$ (where $t\text{-}ZrO_2$ represents tetragonal zirconia), even when both catalysts have equivalent zirconia surface areas and similar concentrations of dispersed copper. This difference is primarily attributed to the presence of oxygen vacancies on the surface of $m\text{-}ZrO_2$ which facilitate the reaction between CO and nearby hydroxyl groups, leading to the formation of formate species. Furthermore, they provide additional sites for the activation and storage of hydrogen. These unique properties result in higher CO adsorption capacities and increased rates of methoxide species elimination on $Cu/m\text{-}ZrO_2$ in comparison to $Cu/t\text{-}ZrO_2$.

2.3.2.1.11 Methanol Dehydration to DME

Typically, methanol dehydration is catalyzed by the acidic sites present on a catalyst. Yoo et al [50] conducted an NH_3-TPD and an activity analysis on $Cu/Ce_{1-x}Zr_xO_2$ which indicated that the overall surface acidity of $Cu/Ce_{1-x}Zr_xO_2$ increased as the Zr content (x) increased. With the rising x value in the $Cu/Ce_{1-x}Zr_xO_2$ catalysts, there was a noticeable increase in methanol dehydration, DME formation, where this phenomenon was primarily driven by the variations in the surface acidity of the catalysts which is evident in Figure 9 below.

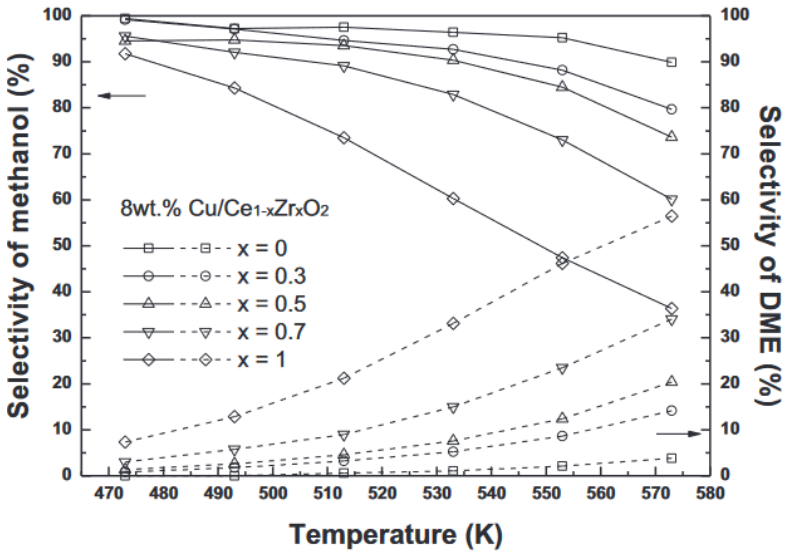

Figure 9-Selectivity of methanol and DME over 8wt% $Cu/Ce_{1-x}Zr_xO_2$ catalyst. Reaction conditions: $CO/CO_2/H_2/N_2$ =19/9.5/66.5/5, P=30 bar, w=0.75 g_{cat} s/ml. Reprinted with permission from ref [50]

Given the influence of CO_x mobility on activity, it was anticipated that the primary sequence of CO_x hydrogenation over $Cu/Ce_{1-x}Zr_xO_2$, particularly when x = 0.3 or 0.5, where oxygen vacancy concentration was elevated, comprised the subsequent elementary steps:

1. Hydrogen (H_2) chemisorption takes place on the copper (Cu) site.
2. CO_x species are adsorbed onto the oxygen vacancy sites of the $Ce_{1-x}Zr_xO_2$ support.
3. CO_x then migrates to adjacent H-Cu sites.
4. Reduction of CO_x occurs into methanol through the hydrogen that had chemisorbed onto the copper.
5. A fraction of the produced methanol undergoes dehydration to yield dimethyl ether (DME) on the acidic surface sites of the $Ce_{1-x}Zr_xO_2$ support.

2.3.2.1.12 Kinetic modeling

Potot et al. [56] have investigated the kinetics of the conversion of CO_2 to methanol using a $Cu/CeO_2/ZrO_2$ catalyst. In their study, they examine the relative impact of CO_2 and CO hydrogenation, distinguishing between direct and indirect pathways in methanol synthesis. Their findings indicate that the indirect pathway, involving CO hydrogenation, becomes more favorable at high temperatures. Consequently, their research provides a valuable tool in the form of a kinetic model, which can be employed for the design of reactors and processes based on novel catalysts. Importantly, it deepens our comprehension of the underlying reaction mechanisms discussed earlier, serving as a foundation for further advancements in catalyst development. The kinetic model is further illustrated in section 2.4.

2.3.2.2 $CuO/ZnO/Al_2O_3$

In the industrial low-pressure methanol synthesis process using syngas, $Cu/ZnO/Al_2O_3$ catalysts are predominantly employed where the typical range of the catalyst composition is 50-60% Cu, 20-30% Zn and 5-10% Al_2O_3 [57]. The most successful catalytic results have been achieved with $Cu/ZnO/Al_2O_3$ catalysts prepared through the coprecipitation method, involving the use of copper, zinc, and aluminum

nitrates, along with alkali bicarbonates or carbonates as basic precipitants. These hydroxy carbonates are then transformed into metal oxides through subsequent heating. The final active catalyst is obtained by reducing CuO to metallic copper under a diluted H_2 flow at elevated temperatures before introducing the syngas mixture [58].

The role of metallic copper (Cu^0) in the reaction mechanism has been extensively debated in the literature for the past two decades and remains a topic of discussion. Presently, it is widely acknowledged that the active sites for the methanol synthesis reaction on Cu/ZnO-based catalysts are metallic copper clusters [57][4,5]. It has been speculated that the primary function of ZnO is to enhance the copper dispersion in the calcined catalyst, thus providing a greater number of active sites for reaction [58]. However, many studies have shown that the ZnO not only act as a support or to increase copper dispersion but also interacts with the active sites as a promoter [58]–[63].

Al_2O_3 is known to be useful for inhibiting metal particle sintering, accelerating the adsorption and activation of CO because of its disorder and defect surface domain [64]. It also improves the catalyst stability and exploitation of the active sites of Cu during the reaction [40]. In the $Cu/ZnO/Al_2O_3$ system, Al_2O_3 can form zinc aluminate to prevent the agglomeration of active and stabilize the highly dispersed Cu/ZnO structure [65].

2.3.2.2.1 Morphology:

While highly dispersed Cu particles or small Cu clusters on ZnO may have a different morphology in model laboratory catalysts, in industrial catalysts, the Cu and ZnO particles are mixed, with ZnO acting as a spacer to prevent sintering of Cu particles [61], [62], [66], [67] .The formation of the Cu-Zn surface alloy in industrial catalysts is responsible for promoting methanol synthesis activity from CO_2 and H_2 [59], [61], [62]. In a study by Behrens et al., the micrographs showed that the vast majority of Cu nano particles, (NPs), were faulted and exhibited planar extended defects, stacking faults, and twin boundaries that ran through the whole particle [59]. The NP shapes were generally spherical, with surface steps caused by the curvature of the particle. Stepped surface facets and twin boundaries were found to create inward curvatures and distinctive surface ensembles, even on flat surfaces of larger Cu nanoparticles. The Zn was observed to be alloyed into those Cu steps. These defects on the catalyst surface proved to be the reason behind the high activity measured using high-resolution transition electron microscopy (HRTEM).

On the other hand, it is proven that ZnO's influence on the catalytic performance extends beyond the creation of defective Cu nanoparticles or the effective stabilization of Cu within the wurtzite-type ZnO structure. This oxide also triggers the Cu-ZnO synergy and the Strong Metal-Support Interaction (SMSI) upon reduction in hydrogen. SMSI commences with the partial reduction of the oxide support, which is expressed in either morphological and/or electronic changes [59], [68]. For the morphological changes, an increase in adhesion occurs, contingent on the wetting characteristics of the oxide [68]. Whereas in the case of electronic changes, electrons move from the oxide support to the metal through the interface. When the oxide is mobile, there is even the potential for partially reduced oxide to migrate across the metal particle.

In addition to the thermodynamically stable wurtzite ZnO structure found on the Cu surface, layered overgrowth composed of ZnO are said to form and surround the Cu nanoparticles in the form of metastable layered, graphitic, polymorph [68]. For this polymorph, Zn is located on top of oxygen and each atom has a three-fold coordination graphitic as shown in Figure 10.

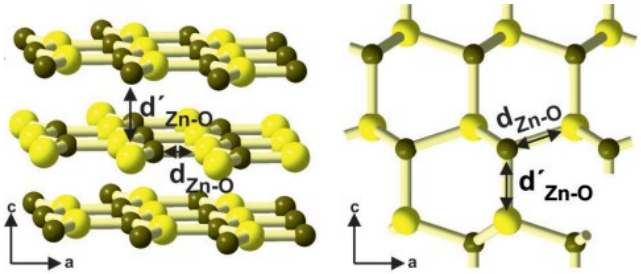

Figure 10-Comparison of the graphitic and wurtzite ZnO poly morphs: ball-stick model of the ideal "graphitic" ZnO in the h-BN structure and wurtzite ZnO viewed along the crystallographic b axis. Small balls: Zn atoms, Large balls: O atoms. Reprinted with permission from ref [68].

Extended exposure to electron-beam irradiation triggered morphological changes in the metastable graphite like ZnOx polymorph. This transformation, observed through a series of high-resolution transmission electron microscopy (HR-TEM) images, can be divided into three distinct stages as shown in Figure 11. Firstly, there is the initiation of overgrowth, causing the surface of the Cu particle to de-wet. Secondly, the metastable rock-salt ZnO polymorph begins to crystallize. Thirdly, this crystalline structure undergoes a further transformation into the thermodynamically stable wurtzite ZnO structure due to continued exposure to the electron beam. Consequently, the electron beam treatment of the metastable ZnO_x serves as a means to overcome the energy barrier that separates different ZnO polymorphs, facilitating the phase transformation. Furthermore, the presented data show the occurrence of a layered ZnO overgrowth on Cu particles after reduction in hydrogen as can be observed in Figure 12.

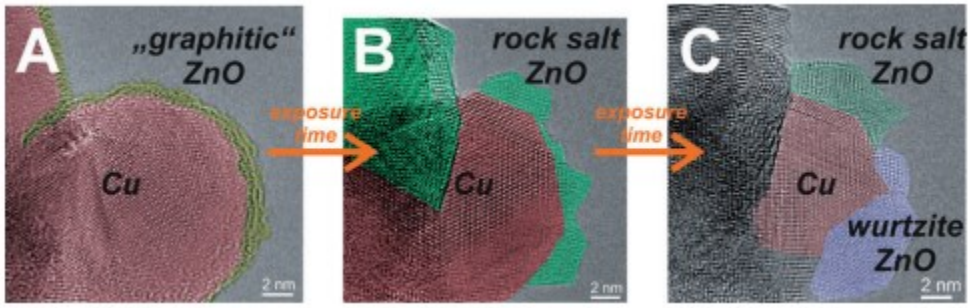

Figure 11-Transformation from graphitic-like ZnOx to the wurtzite structure. A-C) HRTEM images of Cu/ZnO/Al_2O_3 after different times of electron beam exposure. The colors indicate the different state during phase transformation. The red-colored sites correspond to Cu particles. Yellow indicates graphitic-like ZnOx. Green highlights the rock salt ZnO and blue regions correspond to the wurtzite ZnO structure. Reprinted with permission from ref [68].

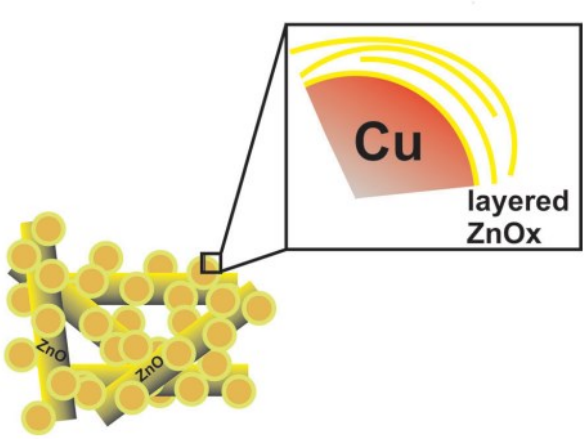

Figure 12- Illustration of Cu/ZnO/Al_2O_3 after reduction inn hydrogen. The inset emphasizes the distorted ZnO overlayer observed on the Cu particles. Reprinted with permission from ref [68].

2.3.2.2.2 Active Sites:

Extensive studies have been carried out to reveal the structure sensitivity by examining the activity of single crystals such as Cu(100), Cu(110), and Cu(111). Results indicate that CO_2 hydrogenation to CH_3OH is structure-sensitive to the Cu facet and surface structure. As for the Cu/ZnO catalysts, the interface is crucial for CH_3OH synthesis [5], [59], [69]. Generally, two possible active sites are proposed at the interface, though there are intense debates regarding the exact nature of the interfacial sites. One possibility is the synergy between Cu and ZnO at the interface as proposed by Kattel et al [60]. Cu−Zn surface alloy sites are the other possibility, the formation of which might promote the partial reduction of ZnO particles to the $Zn^{\delta+}$ state, or modification of Cu surfaces with metallic Zn [59].

The catalytically active state of Zn and Cu in methanol synthesis was found to be metallic, with formate intermediates bound to Zn atoms. An industrial Zn-deposited Cu(111), Zn/Cu(111), was studied by Nakamura et al and Fujitani et al, and was found to be a good model for Cu/ZnO methanol synthesis catalysts in terms of turnover frequency (TOF) and activation energy [69], [70]. When comparing Zn/Cu(111) to clean Cu(111) , infrared reflection absorption spectroscopy(IRAS) showed common peaks between the two samples assigned for formate species. However, Zn/Cu(111) showed additional peaks that were assigned to bridging bidentate formate species and methoxy species adsorbed on a Cu-Zn as shown in Figure 13. Thus the Cu-Zn site on Zn/Cu(111) was identified as the active site for methanol synthesis, promoting the hydrogenation of formate to methoxy species [69], [70].

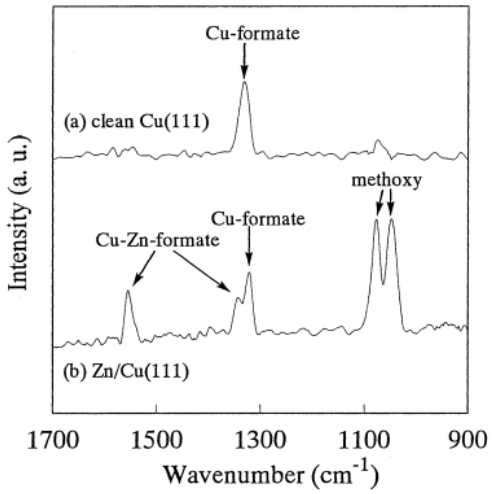

Figure 13-In situ IR absorption spectra of formate species and methoxy species on clean Cu(111) and Zn/Cu(111) during CO_2 hydrogenation. Reprinted with permission from ref [61].

A similar study was conducted by Behrens er al. [59], where a flat Cu(111) surface representing the ideal defect-free catalyst, and a stepped Cu(211) surface were used to demonstrate the effect of surface defects. Both samples showed the same reaction pathway for CO_2 and CO hydrogenation, however the energies of the intermediates and the transition states were stabilized considerably for the Cu(211) surface compared with the Cu(111) as shown in Figure 14. The steps in Cu(211) were said to lower the adsorption energies of the intermediate compared to the flat surface rendering them more active than terraces. Incorporating Zn into the Cu(211), CuZn(211), increased the adsorption strength of the intermediates leading to an increase in methanol synthesis. The order of activity for CO_2 as well as for CO hydrogenation was CuZn(211) > Cu(211) > Cu(111). The most active surface was therefore found to be a Cu step with Zn alloyed into it.

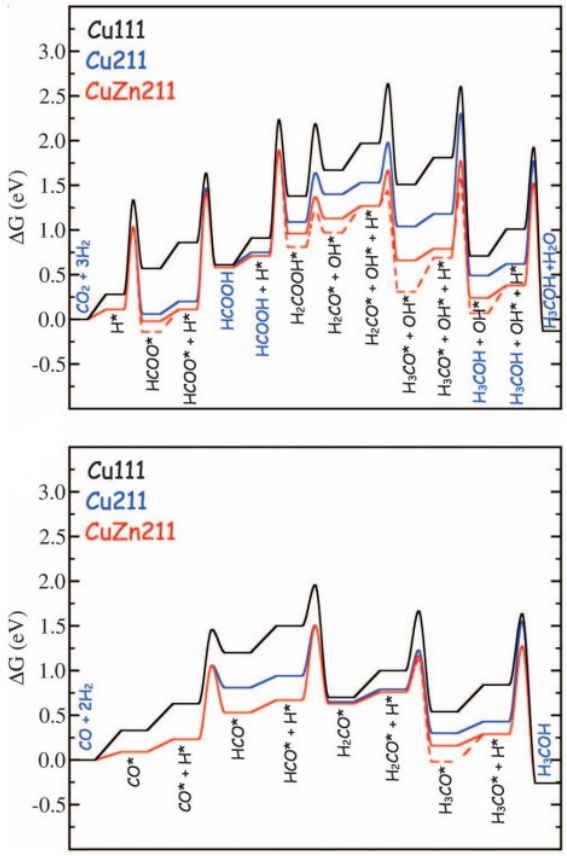

Figure 14- Gibbs free energy diagram of Cu(111), Cu(211) and CuZn(211) obtained from DFT calculations for CO_2 and CO hydrogenation on close-packed(black), stepped(blue), and Zn substituted steps(red). The dashed lines represent the Cu steps where Zn substitution took place. Reprinted with permission from ref [59].

Kattel et al conducted comparisons between ZnCu(111), ZnO/Cu(111), and ZnCu(211) model surfaces. Based on X-ray photoelectron spectroscopy (XPS) measurements, and density functional theory (DFT) results, they reached the conclusion that Zn in ZnCu and Zn/Cu systems undergo surface oxidation to ZnO during the CO_2 hydrogenation reaction, which results in an increase in methanol synthesis activity. Thus, ZnO-Cu interface promotes the formation of multiple active sites and therefore the synergy between Cu and ZnO at the interface should account for the methanol synthesis activity [60].

2.3.2.2.3 Catalyst Activity:

High activity was generated by two factors:

First, the presence of structural defects at the Cu surface is required [59], [66], [67], [71] such as the presence of steps, which can be stabilized by bulk defects like stacking faults or twin boundaries terminating at the surface, in addition to the presence of lattice strains at the Cu surface area [67], [71]. These microstructural features can be seen in Figure 15, and they play a major role in increasing the catalyst activity by providing a stronger binding of the intermediates and lowering the energy barriers between them [59].

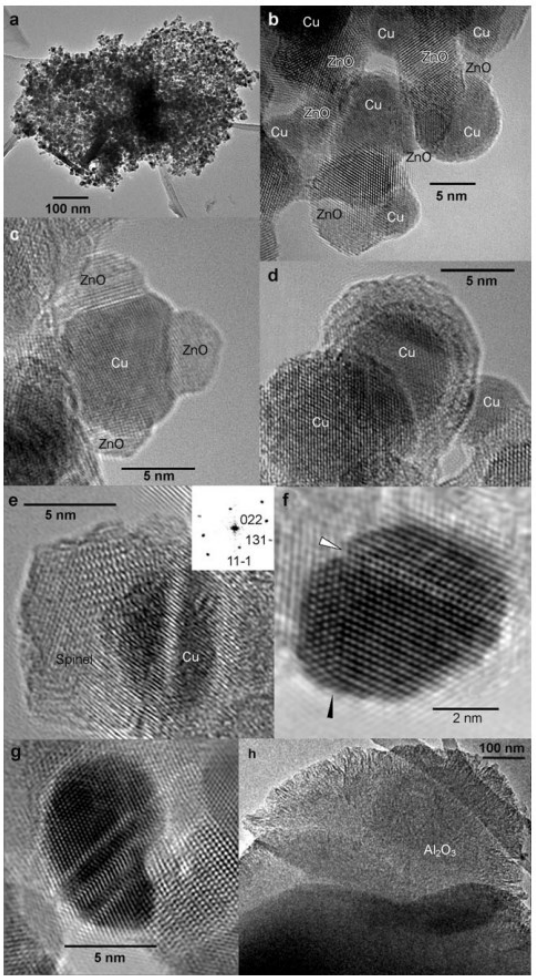

Figure 15- Microstructural features revealed by TEM. a)100nm sized clusters, b)porous framework formed of Cu and ZnO, c) Partial coverage of copper surface by ZnO, d) Complete coverage of copper surface by ZnO, e) crystallized and spinal like cubic structures of $ZnAl_2O_4$, f) Coherent(black arrow) and partially coherent(white arrow) twin boundaries, g)Twin boundaries and stacking faults, h) Agglomerated Alumina with traces of Cu and Zn. Reprinted with permission from ref [67].

The second requirement is the presence of $Zn^{\delta+}$ at the defective (stepped) Cu surface which results from a dynamic metal support interaction (SMSI) effect leading to partial coverage of the metal particles with ZnO_x [59]. Nakamura et al explains that the oxidation state of the active site (Cu-Zn or Cu-O-Zn) depends on the reaction atmosphere and the amount of Zn, with the amount of Zn being the most important factor in creating the Cu-O-Zn site [61]. Excess Zn over the limit for a stable Cu-Zn surface alloy is readily oxidized to ZnO_x, while the stable Cu-Zn surface alloy remains in a metallic form [61], [70].

The ZnO oxidation state under reducing conditions is crucial for the catalyst performance in methanol synthesis. ZnO can be partially reduced however not enough to favor bulk alloying [59]. Increasing the ZnO content in the Cu/ZnO catalyst to a certain extent promotes the formation of Cu-Zn alloy in the Cu particles [62] and increases methanol synthesis. As shown in Figure 16, the Cu surface area measured by XRD reached a maximum when the ZnO content increased to 40-50 % promoting Cu dispersion and consequently an increased methanol yield, Figure 17. However, for a Zn content above 50% the Cu

surface area starts to decrease and that is attributed to the decrease in Cu content, where the particle size of Cu remains constant above a ZnO content of 40% shown in Figure 18. It is worth noting that the difference in the Cu surface area values in Figure 16 and Figure 18 is attributed to the fact that the former was measured using XRD while the latter was measured using reactive frontal chromatography (RFC).

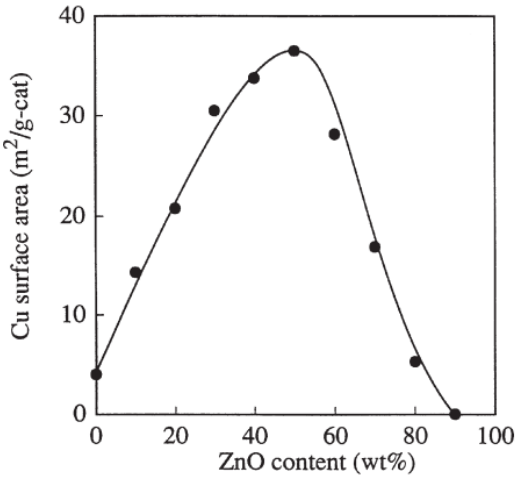

Figure 16-Yeild of methanol as a function of Cu surface area. Reprinted with permission from ref [62].

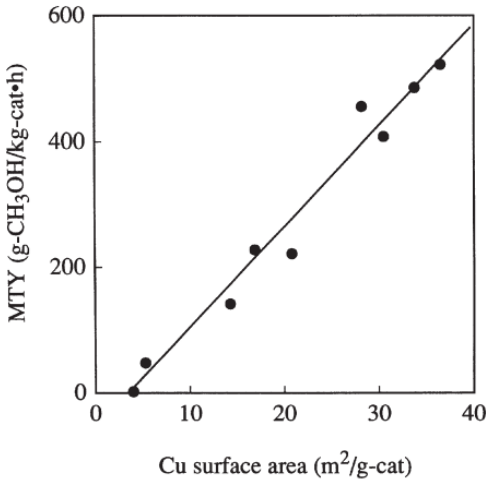

Figure 17-Cu surface area as a function of ZnO content. Reprinted with permission from ref [62].

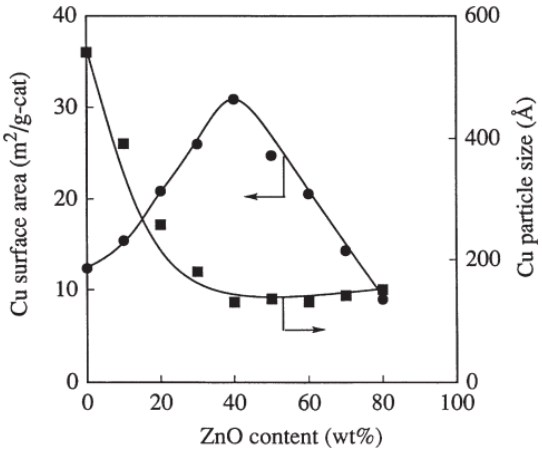

Figure 18-Cu surface area and particle size as a function of ZnO content in the Cu/ZnO catalysts content. Reprinted with permission from ref [62].

Similar trends are observed for the inverse ZnO/Cu(111) system where the maximum methanol production rate was reached when the fraction of Cu(111) covered by ZnO increased to 0.2 monolayer but then decreased with further ZnO coverage, Figure 19 [60], [61]. A comparison between Zn/Cu(111) and ZnO/Cu(111) systems, shown in Figure 20-b, revealed that the activity of Zn/Cu(111) increased with time until it exhibited the same performance as ZnO/Cu(111) . Further XPS measurements revealed that the increase in catalytic activity was associated with a shift in the corresponding Zn $2p_{3/2}$ peaks positions measured with respect to time, evolving from a binding energy of 1021.1 ev (Zn) to 1021.64 eV (ZnO). Thus the transformation from Zn to ZnO lead to an increase in the catalytic activity for methanol production where the optimal composition for CO_2 hydrogenation to methanol is considered to be ZnO/Cu(111).

Burch et al suggested that the Cu/ZnO synergy may be explained by hydrogen atoms produced on Cu during the co-adsorption of CO and H_2, which spill over onto ZnO and act as a reservoir of H atoms [72]. Spillover hydrogen from Cu may react rapidly with Zn methanoate to produce a methoxy species on ZnO or methanol directly. The two-way transfer of hydrogen between Cu and ZnO is believed to be crucial in the mechanism of methanol synthesis, with even a small amount of ZnO accelerating the RDS on Cu. It is postulated that ZnO acts as a reservoir for spillover hydrogen, and the reverse spillover process may account for the increased rate of methanol synthesis observed on Cu when ZnO is present in the catalyst. Even though a lot of authors have noticed the hydrogen spillover effect, it was suggested that it's not the major role of ZnO compared to the role of creating active sites.

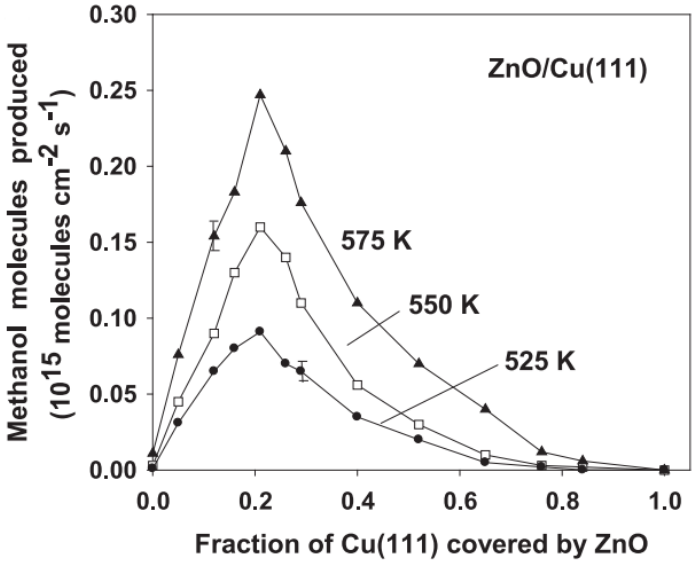

Figure 19-Rate for the conversion of CO2 to methanol on Cu(111) as a function of the fraction of the metal surface covered by zinc oxide. Reprinted with permission from ref [60].

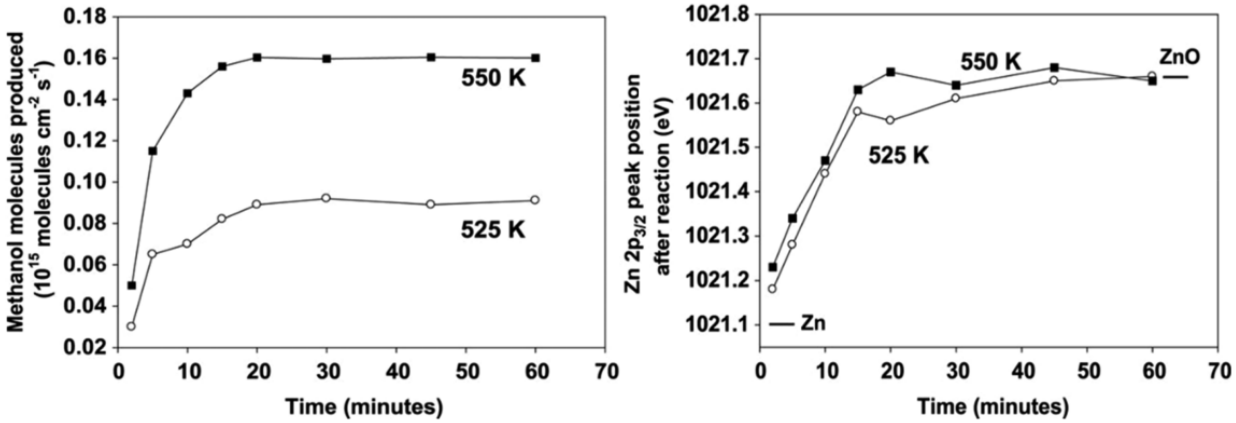

Figure 20-a) Rate of conversion of CO2 to methanol on ZnCu(111) as function of reaciton time (left). b) Zn 2p3/2 XPS binding energies measured after performing the hydrogenation of CO_2 on the Zn/Cu(111) catalyst (right). Reprinted with permission from ref [60].

The combination of Cu and Zn is excellent due to the property of stable surface alloy formation, which further strengthens the binding of the intermediates, increases the Cu dispersion and consequently increases the activity of the catalyst [59], [61], [62]. The data presented indicates that the existence of surface steps and their nearness to zinc oxide (ZnO) on copper (Cu) particles results in the formation of the necessary combination for making methanol catalysis highly effective. Specifically, a copper step in close proximity to Zn functions as an adsorption site for oxygen-bound intermediates due to the greater affinity of Zn for oxygen [59], [60].

2.3.2.2.4 CO hydrogenation:

The yield of methanol by CO_2 hydrogenation increased with increasing reduction temperature, indicating that the Cu-Zn site operates as the active site for methanol synthesis in CO_2 hydrogenation. However, no such increase was observed for the yield of methanol by CO hydrogenation upon reduction treatment, suggesting that the Cu-Zn site does not operate as the active site for methanol synthesis by CO hydrogenation [61].

Opposed to other authors , Nakamura et al claim that the active sites for CO_2 and CO hydrogenations are different, indicating that different mechanisms are involved and highlighting the role of ZnO in Cu/ZnO-based methanol synthesis catalysts [61], [73].

The effect of the oxidation treatment on the catalyst methanol synthesis ability from CO hydrogenation was tested on a physical mixture of Cu/SiO_2 + ZnO/SiO_2 and $(Zn)Cu/SiO_2$. The catalysts underwent reduction followed by oxidation and re-reduction where the methanol yield from a H_2/CO stream at pressure of $P(H_2)/P(CO)$ = 33.3 atm/16.7 atm was monitored. CO hydrogenation was very little when the physical mixture catalyst was reduced, however a significant increase of the methanol synthesis activity by CO hydrogenation was achieved after oxidation as can be seen in Figures 21 - 22. This increase was followed by a decrease in methanol yield after re-reduction indicating that the oxidation state of the catalyst plays a crucial role in the formation of active sites for CO hydrogenation. It was concluded that the promotion of methanol synthesis activity due to the oxidation of Zn species migrated onto the Cu particles suggesting that the active site for the CO hydrogenation is a Cu–O–Zn site on Cu particles [61].

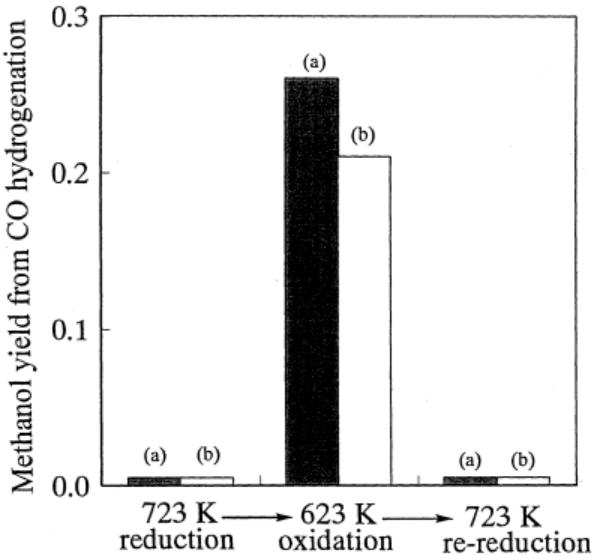

Figure 21-Effeect of reduction-oxidation treatment on the methanol yields by Co hydrogenation over a physical mixure of (a) Cu/SiO_2 + ZnO/SiO_2) and (b) $(Zn)Cu/SiO_2$ catlysts at 523 K. P(H2)/P(CO) = 33.3 atm/1. Reprinted with permission from ref [61].

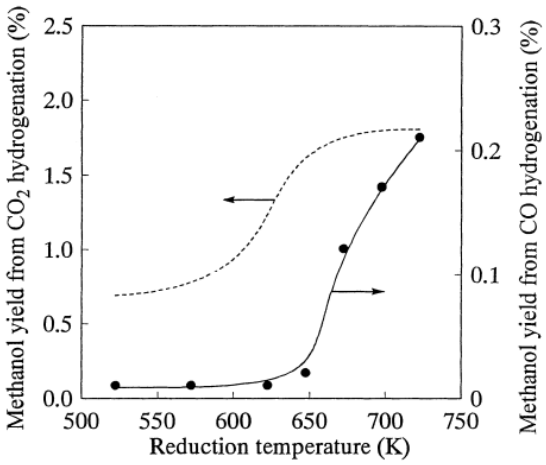

Figure 22-Methanol yield over a (Zn)Cu/SiO2 catalyst as a function of reduction temperature. After the reduction of Cu=SiO2 þ ZnO/SiO2; the Cu/SiO2 was separated from the physical mixture and was oxidized at 623 K. Then CO hydrogenation was carried out at P(H2)/P(CO) = 33:3 atm/16.7 atm and 523 K. The dashed line shows previous results of CO_2 hydrogenation over (Zn)Cu/SiO_2. Reprinted with permission from ref [61].

2.3.2.2.5 Mechanism:

Two primary routes for CO_2 conversion to methanol over the catalyst surface exist. The first involves the Reverse Water-Gas Shift (RWGS) reaction, which produces a CO intermediate followed by its conversion to methanol through hydrogenation (RWGS + CO hydro pathway). The second route includes the initial hydrogenation of CO_2 to form a HCOO intermediate, followed by its hydrogenation and dissociation into methanol (formate pathway), Figure 23. In line with prior computational analyses and by employing Density Functional Theory (DFT), the results indicate that the formate pathway, involving **HCOOH*, **H_2COOH*, and **CH_3O* intermediates, is the preferred route for methanol synthesis where CO_2 hydrogenation predominantly follows the formate pathway on both CuZn and ZnO/Cu systems [59], [60].

On pure Cu catalysts, **HCOO* species are found to play a passive role in methanol synthesis. In contrast, for both ZnCu and ZnO/Cu systems, the introduction of Zn or ZnO plays a vital role in stabilizing **HCOOH* intermediates through direct Zn-O interactions and activates **HCOO* through hydrogenation, which is regarded as the rate-determining step. The enhancement of methanol production on ZnCu catalysts can be attributed to the effective dispersion of Zn sites, including ZnO, on the top layer of the copper surface under the reaction conditions. This results in an increased number of active ZnO-Cu sites, ultimately leading to higher methanol yields.

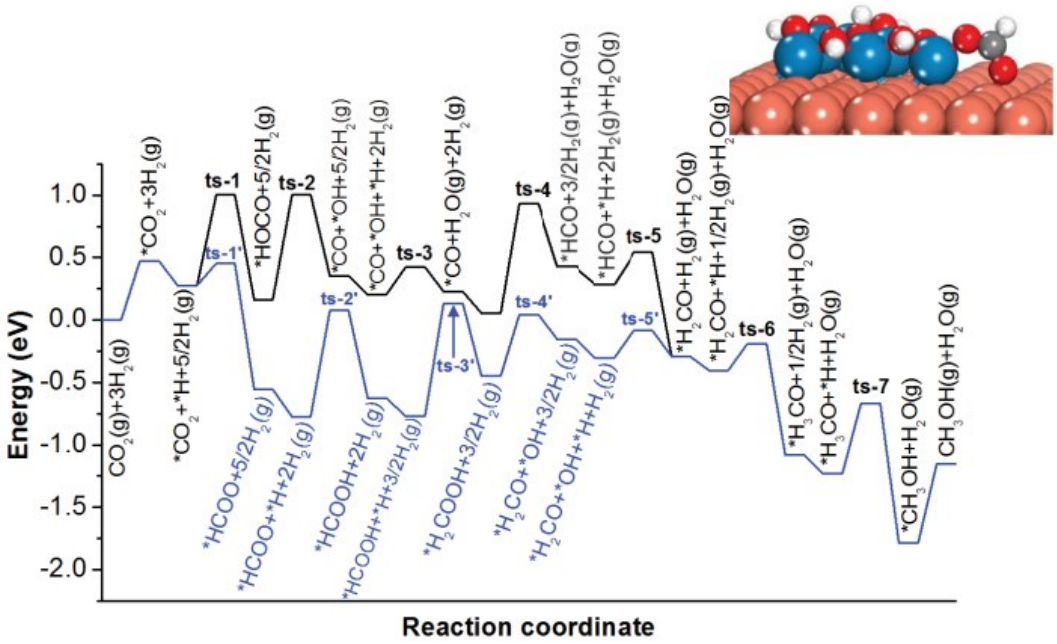

Figure 23-Potentail energy diagram for the hydrogenation of CO_2(g) to CH3OH(g) on ZnO/Cu(111) via the RWGS + CO-hydrogenation and formate pathways. Cu: brown, Zn: blue, O: red, H: white, C: gray. Reprinted with permission from ref [60].

2.3.2.2.6 Kinetic modeling

Several authors have investigated the kinetics of the conversion of CO_2 to methanol using the commercial $Cu/ZnO/Al_2O_3$ catalyst. Different kinetic models for the CO_2 and CO hydrogenation over the commercial catalyst have been proposed, with two main models mostly discussed. One being the dual site model advocated by Graaf et al [74] and the other being the single site model proposed by Bussche and Froment [75] which is currently in use for the methanol synthesis description in the industry. Such kinetic models are employed for the design of reactors and chemical processes and will be discussed in more detail in section 2.4.

2.4 Kinetic Models and Rate Laws for Methanol Synthesis

Kinetic models are used for describing a reaction system, how a reaction proceeds, what is the driving force, and what is the adsorption term. All the studies that have been made so far and all the improvements that have been made in kinetic modeling are on the commercial catalyst, $Cu/ZnO/Al_2O_3$, which helped improve the understanding of the catalysts performance. Later on, those kinetics were further modified and used in software such as “Aspen Plus” which helped in upscaling the methanol synthesis process.

In order to come up with the kinetics that describe the reaction system completely, there should be a common approval of the mechanism with which a reaction proceeds or a product is formed. A lot of authors formulated their hypothesis on how the methanol synthesis takes place and there have been a lot of conflicting and contradicting ideas among the authors.

In their paper, Graaf et al.[74] did a literature review on the work done in the field of kinetics by other authors, and were inspired to improve the accuracy of the kinetic model describing the methanol synthesis. Instead of being biased to any of the previous theories proposed, Graaf et al.[74] considered all three reactions mentioned earlier while formulating their kinetic model. Both the CO and CO_2 hydrogenation routes were considered along with the RWGS in order to account for all the possibilities. The main reason that the RWGS was considered is because it is said to be catalyzed as well on the Cu-Zn-Al surface [74], [75].

A dual site Langmuir-Hinshelwood-Hougen-Watson(LHHW) mechanism was proposed by Graaf et al. [74], where CO and CO_2 adsorb competitively on a site (σ_1) while H_2 and H_2O adsorbs competitively on another site (σ_2). H_2 is considered to adsorb in a dissociative matter. This model is considered as one of the most important models describing the methanol synthesis, and it acted as a base for other models that followed later on [56].

The Adsorption equilibria is as follows:

$$CO + \sigma_1 = CO\cdot\ \sigma_1$$

$$CO_2 + \sigma_1 = CO_2\cdot\ \sigma_1$$

$$H_2 + 2\sigma_2 = 2H\cdot\ \sigma_2$$

$$H_2O + \sigma_2 = H_2O\cdot\ \sigma_2$$

The Assumption of a fixed total number of sites 1 and 2 per catalyst weight allowed [74] to express the total concentration of adsorption sites as follows:

$$C\sigma_{1,tot} = C\sigma_1 + C_{CO}\sigma_1 + C_{CO_2}\sigma_1$$

$$C\sigma_{2,tot} = C\sigma_2 + C_H\sigma_2 + C_{H_2O}\sigma_2$$

The elementary reactions involved in the methanol synthesis overall reaction are tabulated below, Table 2, where the reaction A_3, B_2, and C_3 were chosen to be the rate determining steps (RDS) as they showed an agreement between the experimental results and model calculation for the methanol and water production.

Table 2-The elementary reaction and corresponding driving force for the methanol synthesis process. Adapted from ref [74].

RDS	Corresponding driving force
A_1: $CO\sigma_1 + H\sigma_2 = HCO\sigma_1 + \sigma_2$	$P_{CO}P_{H2}^{0.5} - P_{CH3OH}/P_{H2}^{1.5}\ K_3^{eq}$
A_2: $HCO\sigma_1 + H\sigma_2 = H_2CO\sigma_1 + \sigma_2$	$P_{CO}P_{H2} - P_{CH3OH}/P_{H2}\ K_3^{eq}$
A_3: $H_2CO\sigma_1 + H\sigma_2 = H_3CO\sigma_1 + \sigma_2$	$P_{CO}P_{H2}^{1.5} - P_{CH3OH}/P_{H2}^{0.5}\ K_3^{eq}$
A_4: $H_3CO\sigma_1 + H\sigma_2 = CH_3OH + \sigma_1 + \sigma_2$	$P_{CO}P_{H2}^{2} - P_{CH3OH}/K_3^{eq}$
B_1: $CO_2\sigma_1 + H\sigma_2 = HCO_2\sigma_1 + \sigma_2$	$P_{CO2}P_{H2}^{0.5} - P_{CO}P_{H2O}/P_{H2}^{0.5}\ K_2^{eq}$
B_2: $HCO_2\sigma_1 + H\sigma_2 = CO\sigma_1 + H_2O\sigma_2$	$P_{CO2}P_{H2} - P_{CO}P_{H2O}/\ K_3^{eq}$
C_1: $CO_2\sigma_1 + H\sigma_2 = HCO_2\sigma_1 + \sigma_2$	$P_{CO2}P_{H2}^{0.5} - P_{CH3OH}P_{H2O}/P_{H2}^{2.5}\ K_1^{eq}$
C_2: $HCO_2\sigma_1 + H\sigma_2 = H_2CO_2\sigma_1 + \sigma_2$	$P_{CO2}P_{H2} - P_{CH3OH}P_{H2O}/P_{H2}^{2}\ K_1^{eq}$
C_3: $H_2CO_2\sigma_1 + H\sigma_2 = H_3CO_2\sigma_1 + \sigma_2$	$P_{CO2}P_{H2}^{1.5} - P_{CH3OH}P_{H2O}/P_{H2}^{1.5}\ K_1^{eq}$
C_4: $H_3CO_2\sigma_1 + H\sigma_2 = H_2CO\sigma_1 + H_2O\sigma_2$	$P_{CO2}P_{H2}^{2} - P_{CH3OH}P_{H2O}/P_{H2}K_1^{eq}$
C_5: $H_2CO\sigma_1 + H\sigma_2 = H_3CO\sigma_1 + \sigma_2$	$P_{CO2}P_{H2}^{2.5}/P_{H2O} - P_{CH3OH}/P_{H2}^{0.5}K_1^{eq}$
C_6: $H_3CO\sigma_1 + H\sigma_2 = CH_3OH + \sigma_1 + \sigma_2$	$P_{CO2}P_{H2}^{3}/P_{H2O} - P_{CH3OH}/K_1^{eq}$

Based on the rate determining steps the following rate expressions for the three reactions involved were deduced.

$$r_{C_3)_{CO_2 Hydrogenation}} = \frac{k_{C_3}.b_{CO2}[P_{CO2}P_{H2}^{1.5} - \frac{P_{CH3OH}P_{H2O}}{P_{H2}^{1.5}Keq1}]}{(1+b_{CO}P_{CO}+b_{CO2}P_{CO2})[P_{H2}^{0.5}+\left(\frac{b_{H2O}}{b_{H2}^{0.5}}\right)P_{H2O}]}$$

$$r_{B_2)_{RWGS}} = \frac{k_{B_2}.b_{CO2}[P_{CO2}P_{H2} - \frac{P_{H2O}P_{CO}}{Keq2}]}{(1+b_{CO}P_{CO}+b_{CO2}P_{CO2})[P_{H2}^{0.5}+\left(\frac{b_{H2O}}{b_{H2}^{0.5}}\right)P_{H2O}]}$$

$$r_{A_3)_{CO\ Hydrogenation}} = \frac{k_{A_3}.b_{CO}[P_{CO}P_{H2}^{1.5} - \frac{P_{CH3OH}}{P_{H2}^{0.5}Keq3}]}{(1+b_{CO}P_{CO}+b_{CO2}P_{CO2})[P_{H2}^{0.5}+\left(\frac{b_{H2O}}{b_{H2}^{0.5}}\right)P_{H2O}]}$$

Where, bi is the adsorption equilibrium constant, e.g.b_{CO_2}, k_j is the specific reaction rate constant, and K_{eq_j} is pressure based equilibrium constant.

Poto et al. [56] agreed on the mechanism proposed by Graaf et al., [74] , stating that methanol can be synthesized directly from CO_2 through the direct rout or indirectly from the CO produced via the reverse

water gas shift reaction. The H_2 molecule adsorbs dissociatively on the metallic copper while the oxygen of the CO_2 molecule adsorbs onto the oxygen vacancy created by the CeZr oxide solution. Once the adsorbed hydrogen interacts with carbon, the formate path is created. Where it can be seen in Figure 24 below that both routes overlap once the H_2CO intermediate forms sharing the last to two steps leading to the methanol formation.

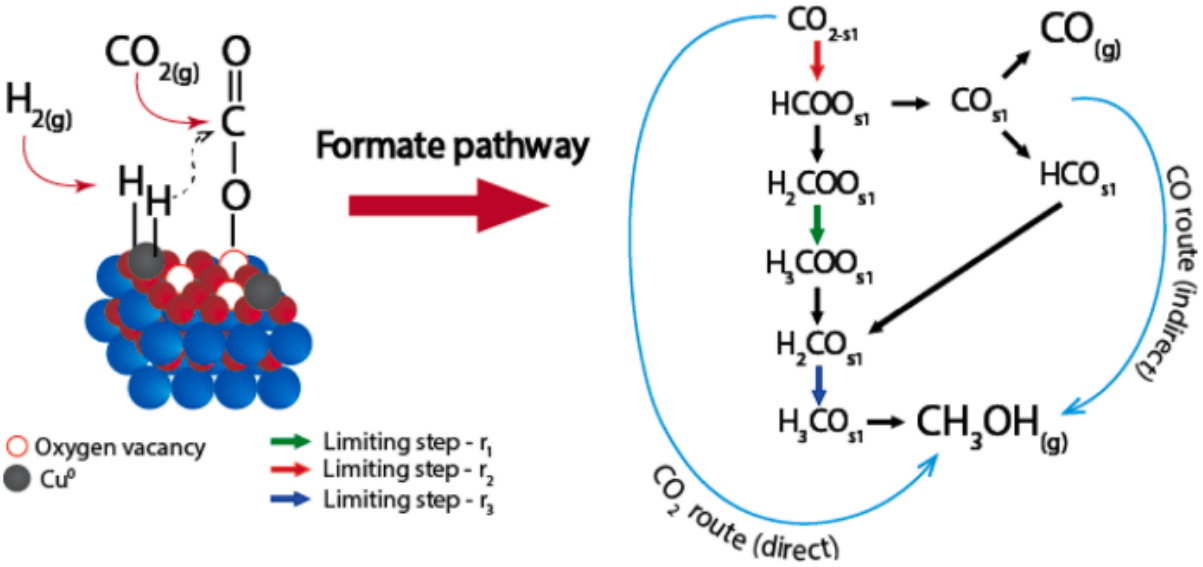

Figure 24-Schematic representation of the reaction mechanism. Reprinted with permission from ref [56]

However, there happens to be an equilibrium between the adsorbed and the desorbed CO at the point where the COs_1 (CO adsorbed) intermediates appear, explaining a certain selectivity towards CO. The contribution of CO_2 and CO to the methanol synthesis relies on various elements like temperature, H_2 concentration, and the arrangement of Cu^0 active sites with respect to oxygen vacancies. However, when the catalyst composition is unchanged, only the reaction conditions can influence the amount of methanol produced through direct and indirect routes [56].

In their work Poto et al. [56] investigate the kinetics of methanol synthesis over a $Cu/CeO_2/ZrO_2$ catalyst through CO_2 hydrogenation. They were able to come up with their unique kinetic model through analyzing single, dual, and three adsorption sites kinetic models retrieved from literature and optimizing those models using an algorithm based on the minimization of the root mean square error while utilizing physicochemical constrains and statistical indicators for model discrimination, Table 3.

The model proposed by Graaf et al.[74] describing a dual site adsorption mechanism on a CuZnAL catalyst was chosen to be the most representative of the current system($Cu/CeO_2/ZrO_2$) . The adsorption term for both catalysts is the same along with the rate determining step for the CO and CO_2 hydrogenation, while the difference falls on the RDS for the RWGS reaction (A3B1C3 instead of

A3B2C3) and the kinetic parameters as well(activation energy, pre-exponential factor, adsorption term) which are represented in Table 4.

Table 3-Physicochemical constraints of the kinetic parameters. Adapted from ref [56].

Parameter	Physicochemical Constraint
Pre-exponential factor, $k_{j,0}$	$k_{j,0} > 0$
Activation energy, $E_{a,j}$	$E_{a,j} > 0$
Enthalpy of adsorption, $\Delta H^0_{ads,i}$	$\Delta H^0_{ads,i} < 0$
Entropy of adsorption, $\Delta S^0_{ads,i}$	$0 < -\Delta S^0_{ads,i} < S^0_{g,i}$

Table 4-Kinetic parameters of Cu/CeO2/ZrO2 catalyst based on the Graaf model(A3B1C3). Adapted from ref [56].

Kinetic Parameters	Value	Units
$k_{1,0}$	$(7.103 \pm 0.351)\cdot 10^{-1}$	$mol.kg_{cat}^{-1}\cdot s^{-1}\cdot bar^{-2.5}$
$k_{2,0}$	$(2.765 \pm 0.118)\cdot 10^{11}$	$mol.kg_{cat}^{-1}\cdot s^{-1}\cdot bar^{-1.5}$
$k_{3,0}$	$(1.416 \pm 0.097)\cdot 10^{9}$	$mol.kg_{cat}^{-1}\cdot s^{-1}\cdot bar^{-2.5}$
E_{a1}	$(3.378 \pm 0.224)\cdot 10^{4}$	$J.mol^{-1}$
E_{a2}	$(1.342 \pm 0.089)\cdot 10^{5}$	$J.mol^{-1}$
E_{a3}	$(1.204 \pm 0.094)\cdot 10^{5}$	$J.mol^{-1}$
$b_{CO2,0}$	$(6.173 \pm 0.327)\cdot 10^{-7}$	bar^{-1}
$\Delta H^0_{ads,CO2}$	$-(5.668 \pm 0.451)\cdot 10^{4}$	$J.mol^{-1}$
$b_{CO,0}$	$(3.561 \pm 0.296)\cdot 10^{-3}$	bar^{-1}
$\Delta H^0_{ads,CO}$	$-(8.438 \pm 0.364)\cdot 10^{3}$	$J.mol^{-1}$
$b_{H2O,H2\ 0}$ *	$(3.521 \pm 0.511)\cdot 10^{-12}$	$bar^{-0.5}$
$\Delta H^0_{ads,H2O,H2}$*	$-(1.242 \pm 0.105)\cdot 10^{5}$	$J.mol^{-1}$

* Parameters to determine the combined adsorption constant of H_2O and H_2 ($b_{H2O} / \sqrt{b_{H2}}$).

Referring to the table above, the pre-exponential factor k_j and the adsorption term for each component(i) ,b_i are calculated as follows:

$k_j = k_{j,0}\exp(-E_{a,j}/RT)$

$b_i = \exp(\Delta S^0_{ads,i}/R).\exp(-\Delta H^0_{ads,i}/RT)$

And,

$\exp(\Delta S^{0}_{ads,i}/R) = b_{i,0}$

Table 5 compares the values of the adsorption constants obtained by Poto et al. [56] and Graaf et al. [74] at 200 and 260℃ . By observing these results and going back to Table 4, it can be deduced that Poto et al. [56] used the average value for the adsorption constants in their calculations without considering the higher and lower limits. With no further comparison made regarding the pre-exponential factors and the activation energy, the average for those values is assumed as well in this study, Table 6.

Table 5-Comparison between the values of the adsorption constants obtained by Poto et al. [56]and Graaf et al. [74] at 200 and 260℃

Adsorption Constant	[56](200-260 ^{0}C)	[76](200-260^{0}C)
b_{CO2} , bar^{-1}	1.117-0.2207	4.517 – 0.7823
b_{CO} , bar^{-1}	$(3.042 – 2.389)\cdot10^{-2}$	3.171 – 0.8313
$b_{H2O} / \sqrt{b_{H2}}$, $bar^{-0.5}$	181.4 – 5.19	$(5.389 – 4.238)\cdot10^{-8}$

Table 6-The calculated kinetic parameters of $Cu/CeO_2/ZrO_2$ catalyst as used by Poto et al. to simulate their model [56].

Kinetic Parameters	Values	Units
k_1	$(7.103\cdot10^{-1})\exp(-\frac{3.378\cdot10^{4}}{RT})$	$mol.kg_{cat}^{-1}\cdot s^{-1}\cdot bar^{-1}$
k_2	$(2.765\cdot10^{11})\exp(-\frac{1.342\cdot10^{5}}{RT})$	$mol.kg_{cat}^{-1}\cdot s^{-1}$
k_3	$(1.416\cdot10^{9})\exp(-\frac{1.204\cdot10^{5}}{RT})$	$mol.kg_{cat}^{-1}\cdot s^{-1}\cdot bar^{-1}$
b_{CO2}	$(6.173\cdot10^{-7})\exp(\frac{5.668\cdot10^{4}}{RT})$	bar^{-1}
b_{CO}	$(3.561\cdot10^{-3})\exp(\frac{8.438\cdot10^{3}}{RT})$	bar^{-1}
$b_{H2O} / \sqrt{b_{H2}}$	$(3.521\cdot10^{-12})\exp(\frac{1.242\cdot10^{5}}{RT})$	$bar^{-0.5}$

The reaction rates (r_j) are function of the partial pressure of the components, and parameters such as kinetic (k_j), adsorption (bi) and equilibrium constants (K_j^{eq}).

Table 7-Equilibrium constant of all the reactions as a function of temperature. Adapted from ref [77].

Equilibrium Constant	Expression	Units
K_1^{eq}	$\log_{10}K_1 = \frac{3066}{T} - 10.592$	bar^{-2} with T in K
K_2^{eq}	$\log_{10}K_2 = \frac{-2073}{T} + 2.029$	Dimensionless with T in K
K_3^{eq}	$\log_{10}K_3 = \frac{5139}{T} - 12.6291$	bar^{-2} with T in K

Bussche & Froment.,[75] argued that the approach taken by Graaf et al. [74] in terms of considering the CO and CO_2 to adsorb and desorb competitively on one site (σ_1) and hydrogen to adsorb and desorb on another site (σ_2) is not a proper approach since some intermediates will feature in two different overall reactions. Implying that the model simultaneously predicts two different concentrations for the same intermediates such as methoxy species and formyl.

Furthermore, they assumed that the main source of carbon for methanol synthesis was CO_2 based on the research done by Rozovskii. [78], in which they used labelled $^{14}CO_2$ and ^{14}CO interchangeably in a mixture of H_2, CO and CO_2 to determine which of these compounds is its carbon-containing precursor by measuring the specific radioactivity of the methanol obtained. The results of the experiments concluded methanol was formed exclusively from CO_2, since the specific radio-activities of methanol and CO_2 in the integral sample were almost identical and greatly exceeded the specific radioactivity of CO. Together with the tracer atom methods and kinetic analysis, the authors reached the conclusion that methanol is synthesized in two microscopic stage, one being the conversion of CO to CO_2 by the water gas shift reaction, and two being the hydrogenation of CO_2 to methanol. The scheme of the methanol synthesis adopted by Bussche & Froment [75] is represented in the table below.

Table 8-Reaction scheme showing the elementary steps for the synthesis of methanol and reverse water gas shift reaction and the rate determining step. Adapted from ref [75]

Elementary Steps	
$H_2(g) + 2s = 2\ H.s$	(b_{H_2})
$CO_2(g) + s = O.s + CO(g)$	RDS,k_1
$CO_2(g) + O.s + s = CO_3.2s$	
$CO_3.2s + H.s = HCO_3.2s + s$	
$HCO_3.2s + s = HCO_2.2s + O.s$	
$HCO_2.2s + H.s = H_2CO_2.2s + s$	RDS, k_2
$H_2CO_2.2s = H_2CO.s + O.s$	
$H_2CO.s + H.s = H_3CO.s + s$	
$H_3CO.s + H.s = CH_3OH(g) + 2s$	
$O.s + H.s = OH.s + s$	(b_X)
$OH.s + H.s = H_2O.s + s$	(b_Y)
$H_2O.s = H_2O(g) + s$	(b_{H_2O})

The assumption of a pseudo-steady-state of the intermediates concentration was made for the derivation of the corresponding kinetics equations. The balance equation for the total concentration (c_t) is used for the calculation of the concentration of the free active sites(c_σ).$c_{Co3.2\sigma}$

$$1 = \frac{c_\sigma}{c_t} + \frac{c_{o.\sigma}}{c_t} + \frac{c_{H_2O\cdot\sigma}}{c_t} + \frac{c_{HCO_2\cdot 2\sigma}}{c_t} + \frac{c_{CO_3\cdot 2\sigma}}{c_t} + \frac{c_{H\cdot\sigma}}{c_t}$$

It can be noticed that the concentrations of adsorbed bicarbonate, formaldehyde, methoxy, methanol, and hydroxyl species were not considered in the total site balance, as their concentration was considered negligible under reaction conditions as reported elsewhere in the literature. Upon elimination of the surface species concentration and introduction of the rate determining steps the following expressions are obtained for the rate of methanol synthesis and the reverse water gas shift reaction are obtained:

$$r_{MeOH} = \frac{k_1 b_{H2} P_{CO2} P_{H2}\left(1 - \frac{1}{K_{eq1}}\frac{p_{H2O} p_{CH3OH}}{p_{H2}^3 p_{CO2}}\right)}{\left(1 + \left(\frac{b_{H2O}}{b_X b_Y b_{H2}}\right)\left(\frac{p_{H2O}}{p_{H2}}\right) + \sqrt{b_{H2} P_{H2}} + b_{H2O} P_{H2O}\right)^3}$$

$$r_{RWGS} = \frac{k_2 P_{CO2}\left(1 - K_{eq2}\frac{p_{H2O} p_{CO}}{p_{CO2} p_{H2}}\right)}{\left(1 + \left(\frac{b_{H2O}}{b_X b_Y b_{H2}}\right)\left(\frac{p_{H2O}}{p_{H2}}\right) + \sqrt{b_{H2} P_{H2}} + b_{H2O} P_{H2O}\right)}$$

b_X and b_Y represent the adsorption equilibrium constants of the elementary steps involved in the formation and dissociation of H_2O on site σ . The equilibrium constants K_{eq1} and K_{eq2} are thermodynamically determined and their values are documented in Table 7 [77]. The kinetic parameters were then calculated from experimental results obtained at a temperature range of 180-280℃ , a pressure range of 15-51 bar and p_{CO} / p_{CO2} ratio of 0-4.1. The results are tabulated below:

Table 9-Kinetic Parameter for the CuO/ZnO/AL_2O_3 .Adapted from ref [75].

Kinetic Parameters	Values	Units
$\sqrt{b_{H2}}$	$(0.499)\exp(-\frac{17197}{RT})$	$mol.kg_{cat}^{-1}\cdot s^{-1}\cdot bar^{-1}$
b_{H2O}	$(6.62\cdot 10^{-11})\exp(\frac{124119}{RT})$	$mol.kg_{cat}^{-1}\cdot s^{-1}$
$\frac{b_{H2O}}{b_X b_Y b_{H2}}$	3453.38	$mol.kg_{cat}^{-1}\cdot s^{-1}\cdot bar^{-1}$
k_1	$(4.297171)\exp(\frac{71090}{RT})$	$mol.kg_{cat}^{-1}\cdot s^{-1}\cdot bar^{-1}$
k_2	$(1.22\cdot 10^{10})\exp(\frac{-94765}{RT})$	$mol.kg_{cat}^{-1}\cdot s^{-1}\cdot bar^{-1}$

The Bussche and Froment [75] model was considered to be the most descriptive model of the methanol synthesis process over the CuO/ZnO/AL_2O_3 and was adopted in Aspen Plus for the simulation of this process on an industrial scale.

2.5 Conclusion

In essence, this literature review underscores the importance of mitigating CO_2 emissions, with a particular emphasis on the transformative potential of converting CO_2 to methanol. The exploration of Cu-based catalysts and their intricate properties provides a solid foundation for future research, promising greener solutions for our energy challenges. Two catalysts were reviewed in depth: Cu/ZnO/Al_2O_3 and Cu/CeO_2/ZrO2. The activity of these catalysts in the hydrogenation process serves as a testament to their efficiency. The intricate relationship between the catalyst's morphology, its chemical and structural surface properties, and the formation of active sites for CO_2 hydrogenation is evident. The literature suggests that these properties aren't just incidental but rather imperative for the mechanism underlying the CO_2 and CO hydrogenation reaction leading to methanol production. As we look ahead, a continued investigation into this domain holds the key to harnessing CO_2 not as a problematic waste but as a valuable resource.

CHAPTER 3: MODEL DEVELOPMENT

3.1 Thermodynamic Modeling

The thermodynamic properties of each element in the reactions as function of temperature and pressure , such as Specific heat (C_p), Entropy (S), Enthalpy (H), and Gibbs free energy (G), were pulled using Fact Sage [79], one of the largest fully integrated database computing systems in chemical thermodynamic, and inserted into Microsoft (MS) Excel. The effect of thermodynamics properties on the equilibrium conversion of CO_2 and CO and consequently the methanol, CH_3OH, yield was then modeled in MS Excel using the Fit to Equilibrium constant method, described below, at a different range of temperatures, 423-573 K, and pressures 2-6 MPa. The equilibrium constants for each reaction (1-3) were calculated at specific conditions using Gibbs free energy.

3.1.2 Fit to Equilibrium Constant Method

The concept behind this method is to use the excel solver to predict the number of mols of each element at equilibrium, based on which the partial pressure will be calculated. User defined logarithmic initial guesses of the number of moles are entered into the Excell cells which will be manipulated by the Excel solver to satisfy several conditions.

1- The calculated ln K values consistent with the partial pressures are equal to those calculated from the Gibbs free energy.

2- The number of C, H and O atoms at equilibrium equals the number of atoms that we started from (material balance).

As a rule of thumb the maximum number of reactions involved in our system and that will be enough to evolve the compounds in all proportions allowed by the stoichiometry without having redundancies, is calculated by subtracting the number of elements from the number of compounds in the system. In our case we have 5 compounds (CO_2, CO, CH_3OH, H_2, H_2O) and 3 elements (C, H, O) and thus the max number of reactions would be 2. The CO_2 HYD and RWGS reactions are considered for the calculation of CO_2 equilibrium conversion and the product (CO and CH_3OH) selectivity and yield. Whereas the CO HYD and RWGS reactions are considered for CO equilibrium conversion results at P: 40 bars.

The initial number of moles for the CO_2 HYD system was set to 1 mol CO_2 and 3 mol H_2. Consequently, the atomic balance was represented as follows:

$$n_{CO} + n_{CO_2} + n_{CH_3OH} = 1 \quad \text{C balance}$$

$$n_{CO} + 2n_{CO_2} + n_{CH_3OH} + n_{H_2O} = 2 \quad \text{O balance}$$

$$2n_{H_2} + 4n_{CH_3OH} + 2n_{H_2O} = 6 \quad \text{H balance}$$

The initial number of moles for the CO HYD system was set to 1 mol CO and 2 mol H_2. Consequently, the atomic balance was represented as follows:

$$n_{CO} + n_{CO_2} + n_{CH_3OH} = 1 \quad \text{C balance}$$

$$n_{CO} + 2n_{CO_2} + n_{CH_3OH} + n_{H_2O} = 1 \quad \text{O balance}$$

$$2n_{H_2} + 4n_{CH_3OH} + 2n_{H_2O} = 4 \quad \text{H balance}$$

The actual number of moles, being the exponential of the initial guesses, are calculated automatically. There are two reasons for using ln values for the manipulated variable, one being that the solver is sensitive for estimations if they are orders of magnitude apart where it won't converge. Two, to ensure that there are no negative or zero values which can cause an error in the calculations of ln K. The use of ln K instead of K is of similar reasons to that of the initial guesses of the number of moles [80].

The thermodynamic properties determined that lower reaction temperatures and higher pressures are more favorable for a high CO_2 conversion and methanol yield as shown in Figures 25 (a,b). CO_2 hydrogenation to methanol and the RWGS reaction exhibit competitive behavior. Due to the exothermic nature of methanol synthesis, the selectivity towards methanol decreases with increasing temperature. On the other hand, the RWGS reaction, characterized by its endothermic nature, becomes more prominent at higher temperatures which in turn increases the selectivity toward CO as can be seen in Figure 25 (c). The results presented here are in line with what has been documented in the literature [41].

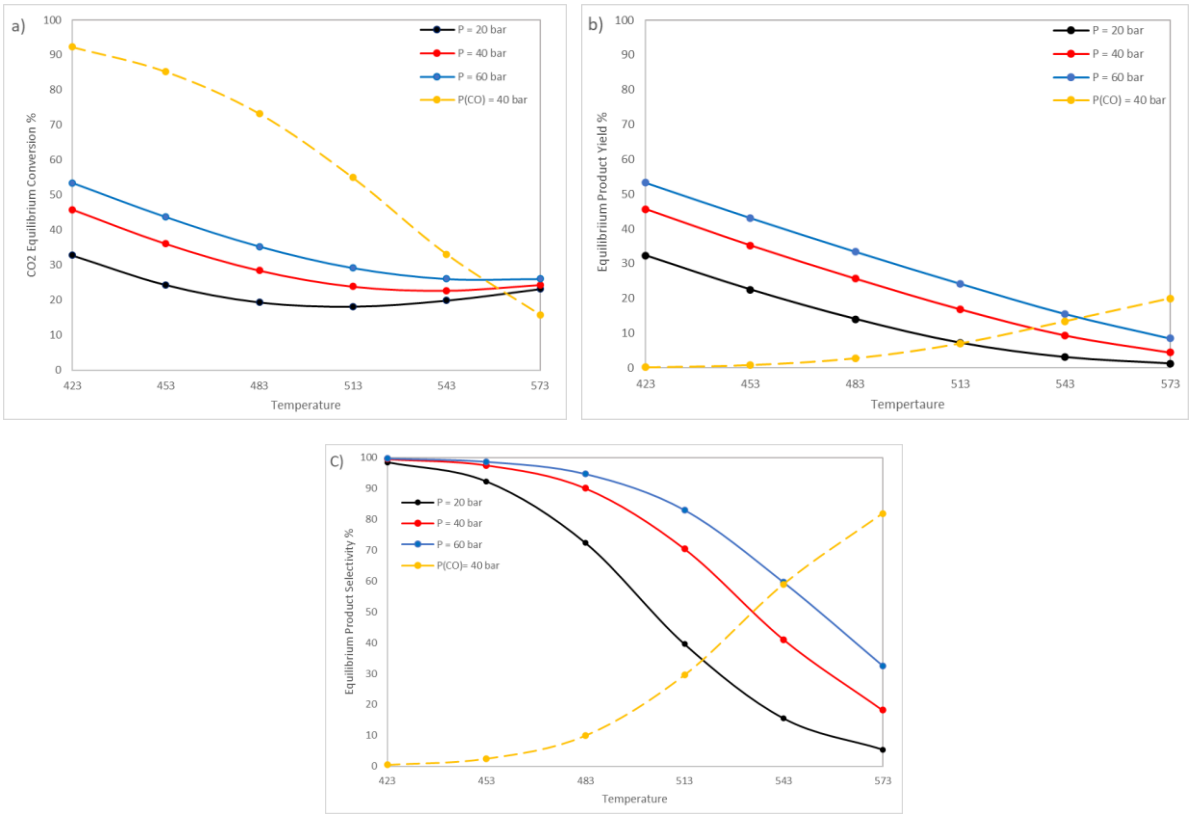

Figure 25-(a) Equilibrium CO_2/CO conversion and (b,c) product, CH_3OH, yield and selectivity as a function of temperature and pressure. The CO_2:H_2 and CO:H_2 mole ratio used is 3:1 and 2:1 respectively.

3.2 Rate Laws

An irreversible reaction is a reaction that proceeds and continues in one possible direction where the reactants are totally consumed to form products. However, there is no reaction completely irreversible, where in a lot of cases the equilibrium lies sharply to the products side that those reactions appear as irreversible [81].

Since we're dealing with reversible reactions then our focus will be the study of those reactions.

All rate laws for reversible reactions must reduce to the thermodynamics relationship relating the reacting species concentration at equilibrium. For instance, the concentrations at equilibrium are related to the equilibrium constant K_c.

$$K_{C1}=\frac{[CH_3OH][H_2O]}{[CO_2][H_2]^3}\ (mol/dm^3)^{1+1-1-3}$$

$$K_{C2}=\frac{[CH_3OH]}{[CO][H_2]^2}\ (mol/dm^3)^{1-1-2}$$

$$K_{C3}=\frac{[CO][H_2O]}{[CO_2][H_2]}\ (mol/dm^3)^{1+1-1-1}$$

Where $[CH_3OH]$ refers to the concentration of methanol and so on for the rest of the elements involved in the reaction. As a rule of thumb, all the concentration involved in the equilibrium constant expression are raised to the power of their coefficient in the reaction.

The rate of disappearance of CO_2:

$$-r_{CO_2} = k_{CO_2}\ [CO_2][H_2]^3 - k_{-CO_2}\ [CH_3OH][H_2O]$$

$$= k_{CO2}([CO_2][H_2]^3 - \frac{k_{-CO_2}}{k_{CO_2}}[CH_3OH][H_2O])$$

$$= k_{CO_2}\ ([CO_2][H_2]^3 - \frac{[CH_3OH][H_2O]}{Kc})$$

At equilibrium $-r_{CO2} = 0$ and thus,

$$k_{CO2}([CO_2][H_2]^3 - \frac{[CH_3OH][H_2O]}{Kc})=0$$

$$\rightarrow K_C = \frac{[CH_3OH][H_2O]}{[CO_2][H_2]^3}$$

The rate for the other elements involved in the reaction can be calculated from the relation:

$$\frac{r_{CO_2}}{-1}=\frac{r_{H_2}}{-3}=\frac{r_{H_2O}}{1}=\frac{r_{CH_3OH}}{1}$$

The concentration equilibrium constant can be also calculated from the enthalpy of formation of a reaction whenever there is no change in the total number of moles and the heat capacity term such as $\Delta C_p=0$.

$$K_C(T)=K_C(T_1)\exp\left(\frac{\Delta H}{R}\left(\frac{1}{T_1}-\frac{1}{T}\right)\right)$$

3.3 Catalysis

A catalyst is a material that enhances the rate at which a forward or a reverse reaction proceeds, without being consumed or generated by the reaction itself. The presence of a catalyst does not influence the underlying thermodynamics of a reaction, such as the equilibrium composition or the heat of reaction [81], [82]. However, it does impact the temperature sensitivity of the reaction rate by reducing the activation energy or the energy barrier along the reaction pathway, facilitating the conversion of reactants into products. When compared to the corresponding uncatalyzed reaction, the catalyzed one occurs faster at a given temperature. Alternatively, catalyzed reactions can even occur at lower temperatures than their non-catalyzed counterparts. In complex reaction networks, a catalyst is frequently utilized to speed up desired reactions and/or to slow down undesired reactions, thereby enhancing the overall selectivity of the process [82]. Based on catalysis, reactions can be further classified into

1. Noncatalytic reactions, e.g., free-radical gas-phase reactions such as combustion of hydrocarbons.
2. Homogeneous catalytic reactions where the catalyst is uniformly distributed throughout the system with the catalyst being dissolved in the same phase as the reactants and products in a homogeneous reaction medium.
3. Heterogeneous catalytic reactions, where a solid catalyst is in contact with reactants and products in a gas-solid, liquid-solid, or gas-liquid-solid, reaction system. The catalyst in this case is not uniformly distributed, and the adsorption of reactants and desorption of products from the catalyst solid surface should take place for a reaction to occur. For instance, CO_2 conversion to methanol.

Steps in a Catalytic Reaction [81]:

1. Diffusion of the reactant from the bulk fluid to the external surface of the catalyst pellet.
2. Diffusion of the reactants from the pore mouth to the vicinity of the internal catalytic surface through the catalyst pores.
3. Adsorption of the reactant onto the catalyst surface
4. Reaction on the surface of the catalyst
5. Desorption of the products from the surface
6. Diffusion of the product from the interior of the pellet to the pore mouth at the external surface

The Langmuir and Hinshelwood kinetic model which is referred to for the representation of the kinetics on the heterogeneous catalyst, suggests that steps 3,4 and 5 take place in series where one particular step is found to be the rate controlling. Since we are dealing with a system of heterogeneous catalytic reaction we will expand on the kinetic representation of these steps leading to the formation of the rate law describing our system.

3.4 Intrinsic Kinetics for Fluid-Solid Catalytic Reaction

More than one type of active site can be present. The reactants in the gas phase adsorb, bond, to the active sites on the catalyst surface in the form molecules or dissociated atoms. The rate of adsorption is proportional to the partial pressure of reactants and to the fraction of vacant sites.

3.4.1 Adsorption Equilibrium

Let's consider the following reaction:

$$A + \sigma \overset{k_A}{\Longrightarrow} A\,\sigma \qquad A + \sigma \underset{k_{-A}}{\Longleftarrow} A\,\sigma$$

The rate of adsorption of A on an active site is directly proportional to the number of collisions a vacant site, ϑ_V, undergoes by a "A" molecule, where with each collision a portion of A is adsorbed, and the collision rate is proportional to the partial pressure of A. Thus, we can conclude the following expression:

$$\text{Rate of adsorption } r_A = k_A \cdot P_A \cdot \vartheta_V$$

On the other hand, the reaction can proceed in the backward direction leading to the desorption of A from the active site, where the rate desorption is proportional to the fraction of occupied sites by A molecules, ϑ_A.

$$\text{Rate of desorption } r_{-A} = k_{-A} \cdot \vartheta_A$$

Thus, the net rate of adsorption equals to the difference between the rate of adsorption and the rate of desorption that is:

$$r_{AD} = k_A P_A \cdot \vartheta_V - k_{-A} \cdot \vartheta_A$$

This can be rearranged in the following form:

$$r_{AD} = k_A\left(P_A \vartheta_V - \vartheta_A \frac{\vartheta_A}{K_A}\right)$$

where K_A is the adsorption equilibrium constant.

At equilibrium the net rate of adsorption equals to zero and the equation can be modified in terms of ϑA :

$$\vartheta_A = K_A P_A \cdot \vartheta_V$$

A material balance on all sites leads to:

$$\vartheta_V + \vartheta_A = 1$$

By replacing the expression of ϑ_A the material balance, the fraction of the vacant site can be expressed as follows:

$$\vartheta_V = \frac{1}{1 + K_A \cdot P_A}$$

Consequently, if there another gas, B, adsorbing on the same type of active site along with A in such a way that:

$$B + \sigma \overset{k_B}{\Longrightarrow} B\,\sigma \qquad B + \sigma \underset{k_{-B}}{\Longleftarrow} B\,\sigma$$

$$\vartheta_B = K_B \cdot P_B \cdot \vartheta_V$$

And the material balance becomes:

$$\vartheta_V + \vartheta_A + \vartheta_B = 1$$

$$\vartheta_V = \frac{1}{1 + K_A \cdot P_A + K_B \cdot P_B}$$

3.4.2 Adsorption on Different Sites

Let's consider that 2 gases A, and B adsorb on two different sites σ_1 and σ_2, and react together in the following manner:

A σ_1 + B σ_2 → Unadsorbed products

Then the rate of adsorption can be expressed as follows

$$r_{Ads,A} = k_A\left(P_A\vartheta_{V1} - \frac{\vartheta_A}{KA}\right)$$

$$r_{Ads,B} = k_B\left(P_B\vartheta_{V2} - \frac{\vartheta_B}{K_B}\right)$$

$$r_{Rxn} = k_1\vartheta_B\vartheta_A = \frac{k_1K_AK_B\,P_A\,P_B}{(1+K_A\cdot P_A)(1+K_B\cdot P_B)} = \frac{k\,P_A\,P_B}{(1+K_A\cdot P_A)(1+K_B\cdot P_B)}$$

3.4.3 Dissociative Adsorption

When adsorption of a polyatomic molecule is accompanied by dissociation the reaction may be written

$$A_2 + 2\,\sigma \rightarrow 2A\sigma$$

$$r_{Ads,A} = k_A\left(P_A\vartheta_v^2 - \frac{\vartheta_A^2}{K_A}\right) = 0 \text{ at equilibrium}$$

$$\vartheta_A = \sqrt{K_AP_A}\cdot\vartheta_V$$

$$\vartheta_V = \frac{1}{1+\sqrt{K_AP_A}}$$

3.4.4 Difference in the Number of Moles, Dual Site Mechanism

For a reaction where:

$$A \leftrightarrow C + D$$

When the number of moles of the product is greater than that of the reactants, it is assumed that the molecule on the reactant side, A, interacts with an adjacent unoccupied site to form an intermediate compound. This compound later dissociates into the molecules in the product side, C&D, leaving each molecule adsorbed on a different active site[83].

$$A\sigma + \sigma \leftrightarrow C\sigma + D\sigma$$

$$A\sigma_2 \leftrightarrow C\sigma + D\sigma$$

The rate of formation of the intermediate compound $A\sigma_2$ is proportional to the fraction of vacant sites, ϑ_V, and to the surface occupied by A, ϑ_A. Consequently, the net rate of reaction is expressed as:

$$r_{Rxn} = k_r\left(\vartheta_A\vartheta_V - \frac{\vartheta_C\vartheta_D}{K_r}\right) = k\left(P_A - \frac{P_CP_D}{K}\right)\vartheta_v^2 = \frac{k\left(P_A - \frac{P_CP_D}{K}\right)}{(1+K_AP_A+K_CP_C+K_DP_D)^2}$$

Where, $k = k_rK_A$ *and* $K = K_AK_r / K_CK_D$

3.4.5 Eley-Rideal Mechanism

This mechanism takes place when a reaction between an adsorbed molecule and a molecule in the gas phase occurs.

$$A\sigma + B(g) \leftrightarrow C\sigma$$

$$r = k_r\left(\vartheta_A P_B - \frac{\vartheta_C}{K_r}\right) = k_r\left(K_A P_A P_B \vartheta_v - \frac{K_C\, p_C\, \vartheta_v}{K_r}\right) = \frac{k\left(P_A P_B - \frac{p_C}{K}\right)}{1 + K_A P_A + K_C P_C}$$

Where, $k = k_r K_A$ *and* $K = K_A K_r / K_C$

3.4.6 Chemical Equilibrium in Gas Phase

In a system where the reacting molecule, A, is not in adsorptive equilibrium but rather in chemical equilibrium in the gas phase according to the following reaction:

$$A + B \leftrightarrow C + D$$

$$P_A = \frac{P_C P_D}{K_e \cdot P_B}$$

Where K_e is the equilibrium reaction constant.

The expression for P_A is substituted wherever it appears in the rate equation. If the rate-determining step is the surface reaction between adsorbed species, then

$$r = kP_A P_B \vartheta^2 = \frac{k\, P_C P_D / Ke}{1 + K_A \cdot \left(\frac{p_C \cdot p_D}{KePB}\right) + K_B P_B + Kc \cdot Pc + K_D P_D}$$

Where $k = k_r \cdot K_A$

Table 10 summarizes some examples of reactions where all substances are in adsorptive equilibrium and the surface reaction controls the rate. In Table 11, substance A is not in adsorptive equilibrium, and its adsorption rate is controlling.

Table 10-Rate law expressions for surface-reaction controlled system in an adsorptive Equilibrium.

Reaction	Special Condition	Basic rate equation	Driving Force	Adsorption Term
A→ C + D	General Case	$r=k\vartheta_A$	P_A	$1+K_A{\cdot}P_A+K_C{\cdot}P_{C+}K_D{\cdot}P_D$
A→ C + D	Sparsely covered surface	$r=k\vartheta_A$	P_A	1
A→ C + D	Fully Covered Surface	$r=k\vartheta_A$	1	1
A↔C		$r=k_r\vartheta_A-k_{-r}\vartheta_C$	$P_A-\frac{P_C}{K}$	$1+K_A{\cdot}P_A+K_C{\cdot}P_C$
A↔C+D	Adsorbed A reacts with vacant site	$r=k_r\vartheta_A\vartheta_V-k_{-r}\vartheta_C\vartheta_D$	$P_A-\frac{P_CP_D}{K}$	$(1+K_A{\cdot}P_A+K_C{\cdot}P_{C+}K_D{\cdot}P_D)^2$
A_2↔C	Dissociation of A_2 upon adsorption	$r=k_r\vartheta_A^2-k_{-r}\vartheta_C\vartheta_v$	$P_A-\frac{P_C}{K}$	$(1+\sqrt{K_A\cdot P_A}+K_C{\cdot}P_C)^2$
A + B → C + D A + B(g) → C + D	Adsorbed A reacts with B in gas but not with adsorbed B	$r=k\vartheta_A\vartheta_B$ $r=k\vartheta_AP_B$	$P_A{\cdot}P_B$ $P_A{\cdot}P_B$	$(1+K_A{\cdot}P_A+K_B{\cdot}P_{B+}K_C{\cdot}P_C+K_D{\cdot}P_D)^2$ $1+K_A{\cdot}P_A+K_C{\cdot}P_C+K_D{\cdot}P_D$
A + B ↔ C		$r=k_r\vartheta_A\vartheta_B-k_{-r}\vartheta_C\vartheta_v$	$P_A{\cdot}P_B-\frac{P_C}{K}$	$(1+K_A{\cdot}P_A+K_B{\cdot}P_{B+}K_C{\cdot}P_C)^2$
A + B ↔ C+D		$r=k_r\vartheta_A\vartheta_B-k_{-r}\vartheta_C\vartheta_D$	$P_A{\cdot}P_B-\frac{P_CP_D}{K}$	$(1+K_A{\cdot}P_A+K_B{\cdot}P_{B+}K_C{\cdot}P_C+K_D{\cdot}P_D)^2$
A_2 + B ↔ C+D	Dissociation of A_2 upon adsorption	$r=k_r\vartheta_A\vartheta_B-k_{-r}\vartheta_C\vartheta_D\vartheta_v$	$P_A{\cdot}P_B-\frac{P_CP_D}{K}$	$(1+\sqrt{K_AP_A}+K_B{\cdot}P_B+K_C{\cdot}P_C+K_D{\cdot}P_D)^3$

Table 11-Rate law expressions for Adsorption rate controlled system (Rapid Surface Reaction).

Reaction	Special Condition	Basic rate equation	Driving Force	Adsorption Term
A→ C + D		$r = kP_A\vartheta_v$	P_A	$1 + \frac{K_A P_C P_D}{K} + K_C{\cdot}P_C + K_D{\cdot}P_D$
A↔C		$r = k(P_A\vartheta_v - \frac{\vartheta_A}{K_A})$	$P_A - \frac{P_C}{K}$	$1 + \frac{K_A P_C}{K} + K_C{\cdot}P_C$
A↔C+D	Adsorbed A reacts with vacant site	$r = k(P_A\vartheta_v - \frac{\vartheta_A}{K_A})$	$P_A - \frac{P_C P_D}{K}$	$1 + \frac{K_A P_C P_D}{K} + K_C{\cdot}P_C + K_D{\cdot}P_D$
A_2↔C	Dissociation of A_2 upon adsorption	$r = k(P_A\vartheta_v^2 - \frac{\vartheta_v^2}{K_A})$	$P_A - \frac{P_C}{K}$	$(1+\sqrt{\frac{K_A P_A}{K}} + K_C{\cdot}P_C)^2$
A + B → C + D	Unadsorbed B reacts with A	$r = k\vartheta_A P_B$	P_A	$1 + \frac{K_A P_C P_D}{K P_B} + K_C{\cdot}P_C + K_D{\cdot}p_D$
A + B ↔ C		$r = r = k(P_A\vartheta_v - \frac{\vartheta_A}{K_A})$	$P_A - \frac{P_C}{K P_B}$	$1 + \frac{K_A P_C}{K P_B} + K_B{\cdot}P_B + K_C{\cdot}P_C$
A + B ↔ C+D		$r = k(P_A\vartheta_v - \frac{\vartheta_A}{K_A})$	$P_A - \frac{P_C P_D}{K P_B}$	$1 + \frac{K_A P_C P_D}{K P_B} + K_B{\cdot}P_B + K_C{\cdot}P_C + K_D{\cdot}P_D$
A_2 + B ↔ C+D	Dissociation of A_2 upon adsorption	$r = k_r\vartheta_A\vartheta_B - k_r\vartheta_C\vartheta_D\vartheta_v$	$P_A P_B - \frac{P_C P_D}{K}$	$(1+\sqrt{\frac{K_A P_C P_D}{K P_B}} + K_B{\cdot}P_B + K_C{\cdot}P_C + K_D{\cdot}P_D)^2$

3.5 Kinetic Model Implementation in Aspen Plus

The kinetic model implemented in this research resulted from multiple approaches utilizing the data fit model, sensitivity analysis and the design specification tools provided in Aspen Plus. The methodology used is a trial-and-error methodology where different combinations of kinetic variations are implemented to understand the system and come up with the best kinetic model that describes it.

The Design specification and sensitivity tools have diverse applications, including aiding in making decisions about the selection of operating conditions for unit operations (such as pump pressures, heat exchanger duties, etc.) as well as determining flow rates and chemical properties (such as composition, temperature, pressure).These tools can also be utilized to propose improved flowsheet designs under various scenarios, predict potential flowsheet inputs and outputs, identify errors like violations of thermodynamic laws within a given flowsheet, recognize certain limitations, and explore other relevant concepts [84].

Sensitivity analysis is a valuable technique used to understand how a process responds to changes in key operating and design factors. By adjusting one or more variables in a process and observing their impact on other variables, it allows for conducting "what if" studies. However, it's important to note that the variables altered must be inputs to the process and not ones that are derived through the simulation. Also,

it should be noted that even though sensitivity blocks provide additional information to base-case results, they have no effect on the base-case simulation. The simulation runs independently of the sensitivity study. If more than one variable is to be varied independently, a separate sensitivity block for each varied variable should be used [85].

When a design specification is used, a desired value for a flowsheet variable or some function of flowsheet variables is specified, sampled variable, along with the variable to be adjusted to satisfy this design specification, manipulated variable. Aspen Plus then manipulates the value of the input variable to achieve the desired value of the flowsheet variable [85].

Data fit or data regression, is an Aspen Plus tool that have the same concept as the design spec, however instead of being limited to one sample variable, the data fit tool permits varying the manipulated variable to obtain several sample variables at once. This tool is considered very valuable in kinetic calculations, where it makes use of experimental results to come up with the corresponding kinetics.

Two approaches were considered for the kinetic model calculation. The first approach is a form of manual data regression that was done through the design specification tool. The literature experimental result for one or two temperatures, precisely 240 and 250, were set as a target by varying the pre-exponential factor and the activation energy of the three reactions involved to obtain the desired the CO_2 conversion and methanol yield. Through trial-and-error experiments, the data obtained at 240 and 250 where the most descriptive of the whole system and thus those two temperatures were considered the base for our calculations.

A sensitivity analysis was conducted to check the effect of the different reaction kinetics, (E&K), of the three reactions occurring on the desired values in terms of CO_2 conversion and methanol and CO yield. The results of the sensitivity analysis display that the reaction kinetics for the RWGS reaction have the strongest effect on the CO yield, while the kinetics for the CO_2 hydrogenation reaction have the strongest effect on the methanol yield. Together they lead to the desired CO_2 conversion values. The kinetics for the CO hydrogenation reaction, however, didn't have a predominant effect on one particular yield and its kinetics were varied as a support to reach the desired results.

The second approach included using the data fit option provided by Aspen Plus and thus a more automatic approach. By using the data fit, a larger set of experimental results can be used, where instead of limiting the kinetic model simulation to experimental results at one or two temperatures, the whole temperature range with the corresponding methanol and CO yield along with the CO_2 values is included and the kinetic data for the three reactions involved are varied simultaneously to try to achieve the best fit. The data fit model offers a range of flexibility where it can be used to achieve a certain accuracy for a specific set of data by using the standard deviation, decreasing it, which gives Aspen Plus a limit on the variation or deviation from the input reference results.

Since the feed used for the calculation of the kinetic model in study didn't include CO, a special case where the CO hydrogenation reaction doesn't take place is considered and a new kinetic model tailored towards the CO_2 hydrogenation and RWGS reactions is calculated where the reaction rate expression is modified accordingly.

Another special case included dividing the temperature range into 3 sets 200-220℃, 220-240℃, and 240-260 ℃ and calculating the reaction kinetics accordingly in an attempt to better describe system at those specific temperature ranges.

The kinetics are first arranged in excel to comply with the Aspen Plus environment, since Aspen Plus adapts a built-in Langmuir–Hinshelwood– Hougen–Watson (LHHW) expression for calculating the rate of reaction when it comes to rate controlled reactions [86].

The general LHHW expressions are expressed below and applied to our system consisting of the CO_2 hydrogenation, reverse water gas shift, and CO hydrogenation reactions.

CO_2 HYD	$CO_2 + 3H_2 = CH_3OH + H_2O$	$\Delta H_{298\,K} = -49.4$ kJ mol^{-1}
RWGS	$CO_2 + H_2 = CO + H_2O$	$\Delta H_{298\,K} = +41.0$ kJ mol^{-1}
CO HYD	$CO + 2H_2 = CH_3OH$	$\Delta H_{298\,K} = -90.4$ kJ mol^{-1}

3.5.1 The General Form for Specifying LHHW Type Reaction In Aspen Plus

$$r = \frac{(Kinetic\ factor)(driving\ force\ expression)}{(adsorpption\ term)}$$

Considering the reaction:

$$W + X \leftrightarrow Y + Z$$

$$\text{Rate} = \frac{k * e^{\left(-\frac{E}{R}\right)\left(\frac{1}{T}\right)}\{kf[W][X] - kb[Y][Z]\}}{Adsorption\ Expression}$$

The rates of the reactions taking place over the CuO/CeO2/ZrO_2 catalyst are expressed as follows:

$$r_1)_{CO_2\ \text{Hydrogenation}} = \frac{k_1 b_{CO_2}\left(P_{CO_2}P_{H_2}^{1.5} - \frac{P_{CH_3OH}P_{H_2O}}{P_{H_2}^{1.5}.K_{eq1}}\right)}{(1 + b_{CO}P_{CO} + b_{CO_2}P_{CO_2})\left(P_{H_2}^{0.5} + \left(\frac{b_{H_2O}}{b_{H_2}^{0.5}}\right)P_{H_2O}\right)}$$

$$r_2)_{RWGS} = \frac{k_2 b_{CO_2}\left(P_{CO_2}P_{H_2}^{0.5} - \frac{P_{CO}P_{H_2O}}{P_{H_2}^{0.5}.K_{eq2}}\right)}{(1 + b_{CO}P_{CO} + b_{CO_2}P_{CO_2})\left(P_{H_2}^{0.5} + \left(\frac{b_{H_2O}}{b_{H_2}^{0.5}}\right)P_{H_2O}\right)}$$

$$r_3)_{CO\ \text{Hydrogenation}} = \frac{k_3 b_{CO}\left(P_{CO}P_{H_2}^{1.5} - \frac{P_{CH_3OH}}{P_{H_2}^{0.5}.K_{eq3}}\right)}{(1 + b_{CO}P_{CO} + b_{CO_2}P_{CO_2})\left(P_{H_2}^{0.5} + \left(\frac{b_{H_2O}}{b_{H_2}^{0.5}}\right)P_{H_2O}\right)}$$

Considering the possibility that only the CO_2 hydrogenation and the reverse water gas shift reaction take place on the surface of the catalyst, the CO adsorption term is eliminated from the denominator and the reaction rate expression becomes:

$$r_1)_{CO_2\ \text{Hydrogenation}} = \frac{k_1 b_{CO_2}\left(P_{CO_2}P_{H_2}^{1.5} - \frac{P_{CH_3OH}P_{H_2O}}{P_{H_2}^{1.5}.K_{eq1}}\right)}{(1 + b_{CO_2}P_{CO_2})\left(P_{H_2}^{0.5} + \left(\frac{b_{H_2O}}{b_{H_2}^{0.5}}\right)P_{H_2O}\right)}$$

$$r_2)_{RWGS} = \frac{k_2 b_{CO_2}\left(P_{CO_2} P_{H_2}^{0.5} - \frac{P_{CO} P_{H_2O}}{P_{H_2}^{0.5} \cdot K_{eq2}}\right)}{(1+b_{CO_2} P_{CO_2})\left(P_{H_2}^{0.5} + \left(\frac{b_{H_2O}}{b_{H_2}^{0.5}}\right) P_{H_2O}\right)}$$

By comparison with the LHHW expression it can be concluded that the kinetic factor is represented as follows:

$$k^* \, e^{\left(\frac{-E}{R}\right)\left(\frac{1}{T}\right)} = k_j * b_i$$

Figures 54 – 56 in the appendix, display the Aspen Plus representation of the kinetic force expression, showcasing the pre-exponential factor "k" and the activation energy for all three reactions using the unmodified kinetics provided in the literature. The Activation energy unit is set to kcal/mol and thus "E" should be multiplied by 0.000239006 to convert it from J/mol. Furthermore, the reaction rate constant unit is set to kmol/kg-s and thus "k" should be multiplied by 10^{-3} to convert it from mol/kg-s and the catalyst weight should be selected as our rate basis for the kinetic expression.

3.5.2 The Driving force for a Reversible Reaction

$$\{k_f [W]^L [X]^M - k_b [Y]^N [Z]^O\}$$

"f" here refers to "forward" while "b" refers to "backwards".

[W], [X], [Y], and [Z] represent the concentration of the reactants and products.

L, M, N, and O represent the concentration exponent for each component.

$$\ln(k_f) = A + \frac{B}{T} + C\ln(T) + DT$$

Alternatively,

$$k_f = \exp(A) * \exp\left(\frac{B}{T}\right) * T^C * \exp(DT)$$

Similarly:

$$\ln(k_b) = A + \frac{B}{T} + C\ln(T) + DT$$

and

$$k_b = \exp(A) * \exp\left(\frac{B}{T}\right) * T^C * \exp(DT$$

A, B, C, and D represent the coefficient for the driving force constant.

Applying this concept when referring to our system will result in:

$$k_f = 1$$

$$k_b = \frac{1}{K_j^{eq}}$$

Thus, the equilibrium constant expression must be modified to match the driving force expression of the LHHW type reaction. Table 12 below displays the modified equilibrium constant expression.

Table 12-Inverse equilibrium constant of all the reactions as a function of temperature

Inverse Equilibrium Constant	Expression	Unit
$1/K_1^{eq}$	$3.9084\times10^{10}.\exp(\frac{-7059.726}{T})$	bar ^{2} with T in K
$1/K_2^{eq}$	$0.009354.\exp(\frac{4773.259)}{T}$	Dimensionless with T in K
$1/K_3^{eq}$	$4.178304\times10^{12}.\exp(\frac{-11832.98479}{T})$	bar ^{2} with T in K

As can be seen in the reaction rate equations, the partial pressure is the basis for the rate of reaction, and thus the reacting phase considered is vapor. Figures 57 – 60 in Appendix.B display the Aspen Plus representation of the driving force expression, showcasing the concentration constants and coefficients for the driving force constant for all three reactions in the forward and backward direction.

3.5.3 The Adsorption Expression

The "Adsorption Expression" in LHHW reactions depends on the assumed adsorption mechanism and usually takes on the following form:

$$\text{Adsorption} = \{1 + K_A[A] + K_B[B] + K_C[C] + K_D[D]\ldots\ldots\}^n$$

By changing the form of the adsorption expression to match that of the LHHW we get:

$$\text{Adsorption} = \{P_{H2}^{0.5} + \frac{bH2O}{bH2^{0.5}} P_{H2O} + b_{CO}P_{CO}P_{H2}^{0.5} + b_{CO} \frac{bH2O}{bH2^{0.5}} P_{CO}P_{H2O} + b_{CO2}P_{CO2}P_{H2}^{0.5} + b_{CO2}\frac{bH2O}{bH2^{0.5}} P_{CO2}P_{H2O}\}^1$$

A representation of the adsorption expression is shown in Figure 61 Appendix B.

3.6 Kinetic Variation and Modification:

The first approach included using the unmodified kinetics in our simulation environment and modifying the activation energy and pre-exponential factor within the range provided, as documented in table 6, while keeping the adsorption constants intact until we reached conversion and product yields similar to those reported in the literature.

After being successful, and in an effort to come up with a more accurate kinetic model, the adsorption constants b_{CO2}, b_{CO}, and $\frac{bH2O}{bH2^{0.5}}$ were varied along the lower and upper limit provided in the literature. The combined adsorption of H_2 and H_2O, $\frac{bH2O}{bH2^{0.5}}$, contributes only to the adsorption term in the denominator and thus it's easy to predict their effect on the reaction rate for each reaction.

However, since the adsorption constants of CO and CO_2, b_{CO} and b_{CO2}, contribute to the kinetic factor in addition to the adsorption term, the prediction of their effect on the reaction is not straightforward. Therefore, upon choosing a value for the adsorption constants, b_i, within the range provided and after

updating the kinetic factor and adsorption term in the simulation with this new value, a sensitivity analysis is conducted varying the kinetic factor within the range of the kinetic constants, k_j to monitor the effect on CH_3OH /CO yield and CO_2 conversion. This approach is repeated in a trial-and-error manner until the range in which the system is described accurately is reached. The adsorption constants and kinetic factors used can be seen in the table below.

Let's Assume that

$$b_i = A \cdot \exp(B/T)$$

$$k_j = C \cdot \exp(D/T)$$

Table 13-: The calculated adsorption constants at the lower, average, and upper limit of the range given in the literature.

b_i bar^{-1}	A	B
$b_{H2O}/\sqrt{b_{H2}}$ Lower Limit	3.01×10^{-12}	13675.728
$b_{H2O}/\sqrt{b_{H2}}$ Average	3.521×10^{-12}	14938.658
$b_{H2O}/\sqrt{b_{H2}}$ Upper Limit	4.032×10^{-12}	16201.588
b_{CO} Lower Limit	3.265×10^{-3}	971.13303
b_{CO} Average	3.561×10^{-3}	1014.9146
b_{CO} Upper Limit	3.857×10^{-3}	1058.6962
b_{CO2} Lower Limit	5.846×10^{-7}	6274.9579
b_{CO2} Average	6.173×10^{-7}	6817.42
b_{CO2} Upper Limit	6.50×10^{-7}	7359.8749

Table 14-The calculated kinetic constants at the lower, average, and upper limit of the range given in the literature.

$k_j\ mol/kg \cdot s$	C	D
k_1 Lower Limit	6.75×10^{-1}	-4332.451287
k_1 Average	7.10×10^{-1}	-4063.02622
k_1 Upper Limit	7.45×10^{-1}	-3793.601155
k_2 Lower Limit	2.65×10^{11}	-17211.93168
k_2 Average	2.77×10^{11}	-16141.4482
k_2 Upper Limit	2.88×10^{11}	-15070.96464
k_3 Lower Limit	1.32×10^{9}	-15612.22035
k_3 Average	1.42×10^{9}	-14481.5973
k_3 Upper Limit	1.51×10^{9}	-13350.97426

The adsorption and kinetic constants are both used to calculate the range in which the pre-exponential factor, K_j, and the activation energy E_i, fall into. As can be seen in Table 15, the adsorption constants are fixed where one adsorption constant is picked at a time while the kinetic constant is being varied. Figures 34 and 35 display the Aspen Plus input environment for the sensitivity analysis.

Table 15-The calculated kinetic factor elements used for the sensitivity analysis in Aspen Plus.

	K (kmol/kg· s) Range	E(kcal/mol) Range
$b_{CO2})_{Min} * k_1)_{min\text{-}max}$	$(3.95 – 4.36)\times 10^{-10}$	(3.857362899) – (4.927392979)
$b_{CO2})_{Avg} * k_1)_{min\text{-}max}$	$(4.17 – 4.60)\times 10^{-10}$	(4.934565497) – (6.004595576)
$b_{CO2})_{Max} * k_1)_{min\text{-}max}$	$(4.39 – 4.85)\times 10^{-10}$	(6.01175382) – (7.0817839)
$b_{CO2})_{Min} * k_2)_{min\text{-}max}$	$(1.55 – 1.69)\times10^{2}$	(-21.71826678) – (-17.46680798)
$b_{CO2})_{\mathbf{Avg}} * k_2)_{min\text{-}max}$	$(1.63 – 1.78)\times10^{2}$	(-20.64106418) – (-16.38960539)
$b_{CO2})_{Max} * k_2)_{min\text{-}max}$	$(1.72 – 1.87)\times10^{2}$	(-19.56387586) – (-15.31241706)
$b_{CO})_{Min} * k_3)_{min\text{-}max}$	$(4.31 – 4.94)\times10^{3}$	(-29.07376819) – (-24.5834634)
$b_{CO})_{Avg} * k_3)_{min\text{-}max}$	$(4.70 – 5.39)\times10^{3}$	(-28.98682825) – (-24.49652346)
$b_{CO})_{Max} * k_3)_{min\text{-}max}$	$(5.09 – 5.84)\times10^{3}$	(-28.89988831) – (-24.40958351)

3.7 Setup and Experimental results:

The catalyst in study, $CuOCeO_2ZrO_2$ was synthesized via the gel-oxalate coprecipitation method with a 50wt% CuO loading and a CeO_2:ZrO_2 mass fraction of 1. The authors in the literature purposely chose the same catalyst wt% as the commercial catalyst in order for both catalysts to be comparable [56].

Figure 26 below shows the experimental setup that Poto et al.[56] used in their research for the catalytic tests. The mass flow controllers, FC, are used to regulate the gas feed going to the reactor placed in a box oven where it's temperature is regulated through thermocouples and controllers, TI and TC, and the pressure is controlled by a back pressure system. The reactor's inner diameter is 10 mm and the catalyst loading used throughout the experiment is 0.25 g.

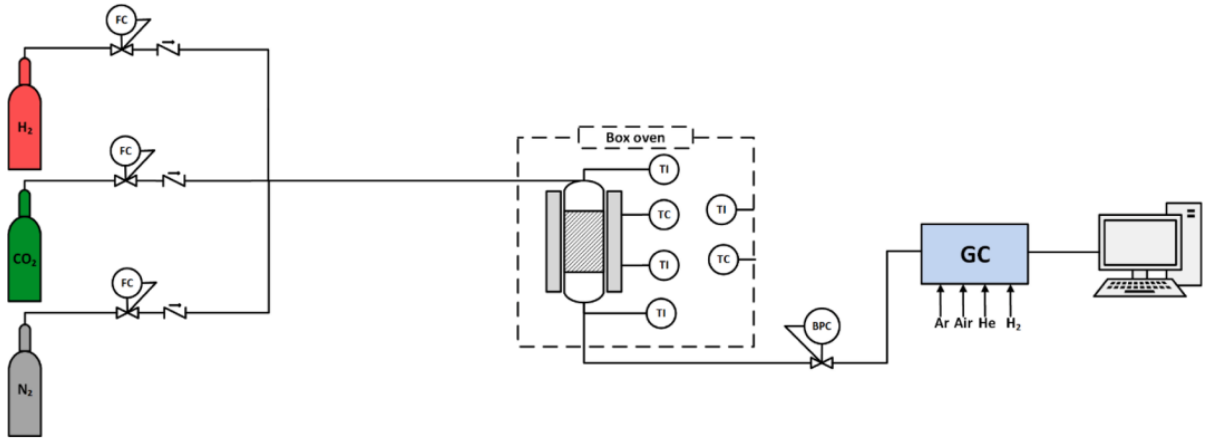

Figure 26-Experimental setup [56]

The reaction tests were performed in temperature and pressure range of 200-260℃ and 10-40 bar respectively while providing a 7500 to 24000 $NL.kg^{-1}_{cat}.h$ GHSV range feed of $H_2/CO_2/N_2$ mixture in different fractions. The catalyst stability was tested on a GHSV of 9600 $NL.Kg^{-1}_{car}.h^{-1}$ with a H_2:CO_2 molar ratio of 3 and a temperature and pressure of 250℃ and 30 bar , respectively, for 100h . The experimental tests used for the kinetic fitting were mostly conducted at a GHSV of 9562 $NL.Kg^{-1}_{car}.h^{-1}$ and thus we will consider this feed when performing kinetic model validation in Aspen Plus. The physical properties of the $CuO/CeO_2/ZrO_2$ catalyst and the Aspen Plus flowsheet for simulating the kinetic model are displayed in Table 16 and Figure 27 respectively.

Table 16-Physical properties of CuO/CeO2/ZrO2 catalyst.

Property	Value
BET surface area, $S_{BET}(m^2.g^{-1})$	79
Pore volume, P.V.$(cm^3.g^{-1})$	0.26
Pore diameter, P.D.(nm)	9.5
Average Cu diameter, d_{cu}(nm)	10.4

Surface-to-volume Cu diameter, d_{Cu}^{sv}(nm)	11.6
Cu dispersion, D_{Cu}(%)	8.56
Cu specific surface area, S_{Cu} ($m_{Cu}^2.g^{-1}$)	58
Catalyst solid density, ρ_{cat}(g.cm^{-3})	7.53
Catalyst porosity, $\varepsilon_{cat}(m_{pore}^3.m_{cat}^{-3})$	0.66
Catalyst apparent density, $\rho_{b,cat}$(g.cm^{-3})	2.56

In order to validate the kinetics and the experimental results, a simulation was conducted under the same conditions and reactor dimensions as the ones mentioned in the literature. A plug flow reactor is used to describe the packed bed reactor where the temperature and pressure are adjusted to match the experimental conditions. The type of the reactor used is a reactor with specified temperature.

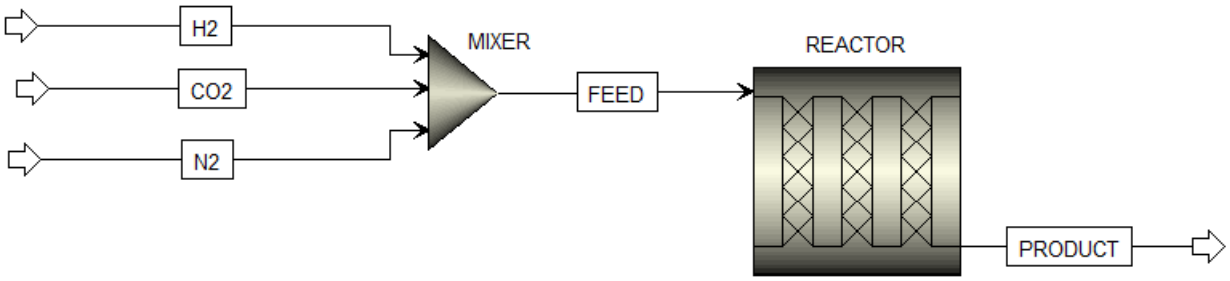

Figure 27-Flowsheet of the process for the validation of results.

Table 17 summarizes the reactor dimensions and the conditions at which the experiments take place. Although the reactor length is not provided in the literature, it was calculated from the apparent density and the catalyst weight according to the following relation:

$$W = V \times \rho_{apparent}$$

$$V = A \times h$$

$$\rightarrow h = \frac{W}{A \times \rho}$$

where "W" is the catalyst weight, "V" is the reactor volume, "ρ" is the apparent density, "A" is the reactor Area, and "h" represents the reactor length.

The apparent density is chosen here since the kinetic rate expressions are based on the weight of the catalyst[76] , and because it counts for the void space present in the reactor and thus it provides an accurate measurement of the space occupied by the catalyst.

Since Aspen Plus does not provide a flow option for GHSV, the mole flow should be calculated and entered into our simulation. To do that, we have to calculate the volumetric flow rate to determine the equivalent mole flow rate.

Volumetric Flow Rate = GHSV × W_{Cat} = 9562 × 0.00025 = 2.3905 $L.h^{-1}$ at T=20℃ and P= 1.01325 bar. This value is then entered into a plug flow reactor at normal condition and results in a mole flow rate of 0.0987991427 $mol.h^{-1}$. The mole flow obtained is used throughout the kinetic testing and validation.

Table 17-Experimental conditions and reactor dimensions.

Pressure range, bar	20-40
Temperature range, ℃	200 -260
Length, mm	1.24
Diameter, mm	10
Catalyst mass, g	0.25
Molar Flow, mol/h	0.0987991427
H_2/CO_2 ratio	3
XCO_2	0.225
XH_2	0.675
XN_2	0.1

CHAPTER 4: APPROACHES AND RESULTS

4.1 Kinetic Model Validation

The kinetic model testing takes place by providing the same feed conditions as the experimental results, by fixing the pressure and varying the temperature. Since the catalyst stability test was done under a pressure of 30 bar, this pressure is going to be considered the base for the kinetic model testing, and the pressures of 20 and 40 bars are used for further validation. The same experimental conditions and reactor dimensions present in table 17 were used in the validation process.

The first approach was inserting the unmodified kinetics as proposed by Poto et al [56] (Table 18) into our simulation and comparing the results to that of the experimental. The CO_2 conversion (X_{CO2}), product yield (Y_i), and product selectivity (S_i) are the main tools for the comparison which wear calculated in excel based on equations 4.1-4.3.

$$X_{CO2} = \frac{F_{CO2}^{in} - F_{CO2}^{out}}{F_{CO2}^{in}} \quad 4.1$$

$$Y_i = \frac{F_i^{out}}{F_{CO2}^{in}} \quad 4.2$$

$$S_i = Y_i . X_{CO2} \quad 4.3$$

The simulation results along with the experimental data are displayed in the following tables and figures:

Table 18-Unmodified Reaction Kinetics

Kinetic Parameters	Values	Units
K_1	4.38E-10	(kmol/kg· s)
K_2	171	(kmol/kg· s)
K_3	5040	(kmol/kg· s)
E_1	-5.469580536	kcal/mol
E_2	18.51533478	kcal/mol
E_3	26.74167586	kcal/mol

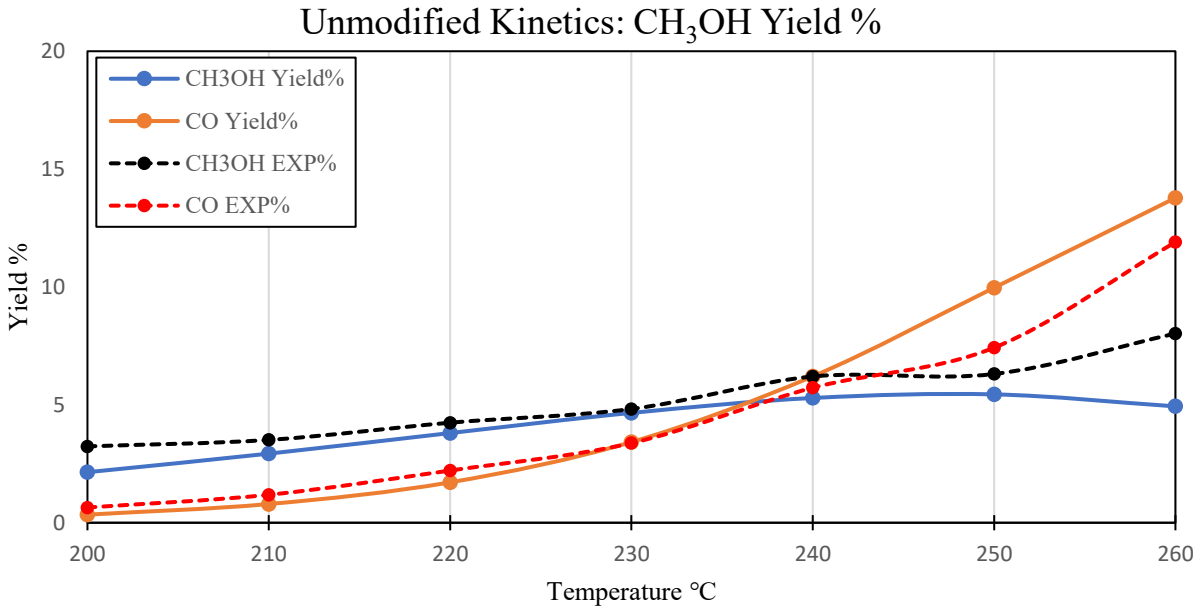

Figure 28-Comparison of the obtained CH_3OH and CO yield with the experimental data reported in the literature.

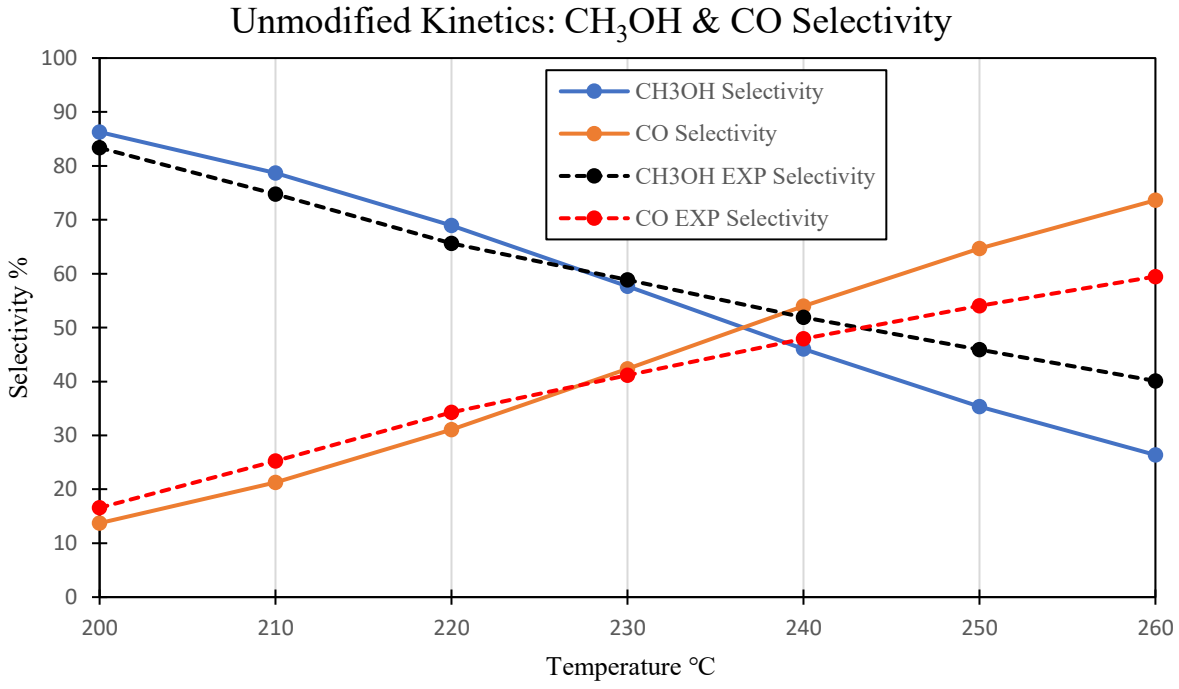

Figure 29-Comparison of the obtained CH_3OH and CO selectivity with the experimental data reported in the literature.

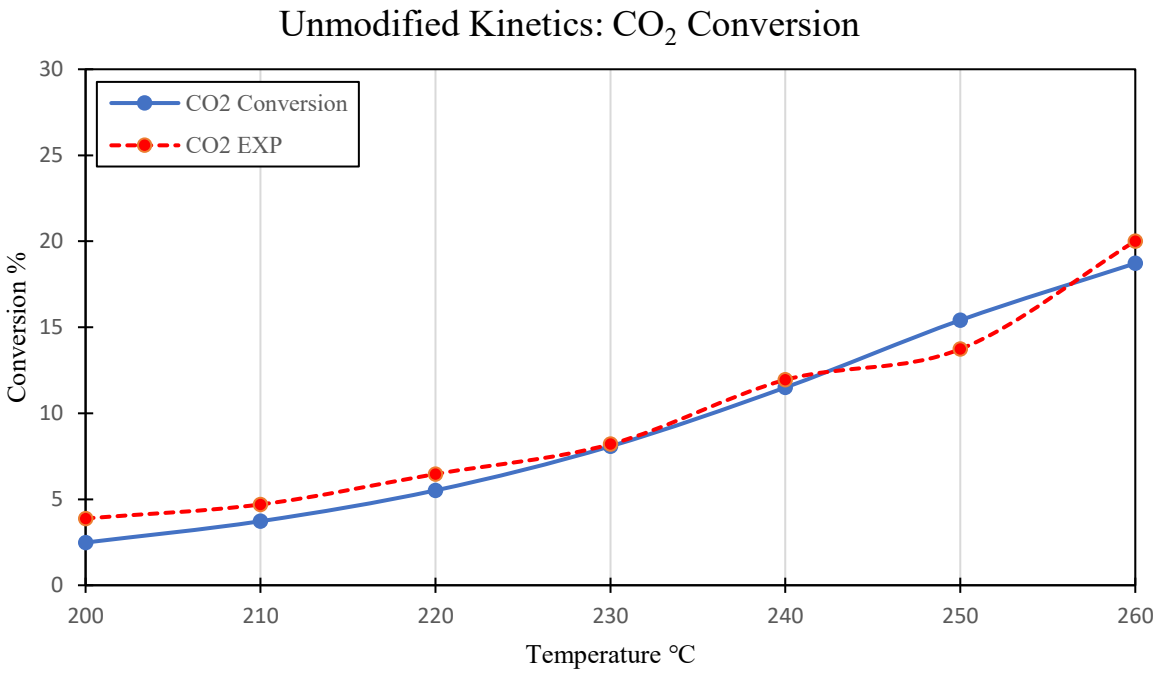

Figure 30-Comparison between the obtained CO_2 conversion results with the experimental data reported in the literature.

Table 19-Error and error percentage of the CO_2 results obtained from the unmodified kinetics model.

CO_2 mol/h	**Experimental**	**Model**	**Error**	**Error%**
200℃	0.021366179	0.0216776729	-0.000311494	-1.46
210℃	0.021185228	0.0214020613	-0.000216833	-1.02
220℃	0.020792205	0.0210035153	-0.000211310	-1.02
230℃	0.020406518	0.0204335527	-0.000027034	-0.13
240℃	0.019574679	0.0196735408	-0.000098862	-0.51
250℃	0.019176765	0.0188039603	0.000372805	1.94
260℃	0.0177814	0.0180694986	-0.000288098	-1.62
SSE			0.000000421	

Table 20-Error and error percentage of the CO results obtained from the unmodified kinetics model.

CO mol/h	Experimental	Model	Error	Error%
200℃	0.000143160	0.000075797	0.000067363	47.05
210℃	0.000263646	0.000176269	0.000087377	33.14
220℃	0.000492390	0.000380840	0.000111550	22.65
230℃	0.000750701	0.000760735	-0.000010034	-1.34
240℃	0.001272879	0.001379954	-0.000107075	-8.41
250℃	0.001650563	0.002215784	-0.000565221	-34.24
260℃	0.002645569	0.003062978	-0.000417408	-15.78
SSE			0.000000530	

Table 21-Error and error percentage of the MeOH results obtained from the unmodified kinetics model.

MEOH mol/h	Experimental	Model	Error	Error%
200℃	0.000719801	0.000476337	0.000243464	33.82
210℃	0.000780933	0.000651477	0.000129456	16.58
220℃	0.000943211	0.000845452	0.000097759	10.36
230℃	0.001072588	0.001035519	0.000037069	3.46
240℃	0.001378915	0.001176312	0.000202603	14.69
250℃	0.001402479	0.001210063	0.000192416	13.72
260℃	0.001783720	0.001097331	0.000686389	38.48
SSE			0.000000636	

The results obtained from the Aspen Plus simulation seem to deviate from what have been reported in the literature in terms of methanol and CO yield over the whole temperature range which is evident in tables 20 and 21 above. Furthermore, it can be noticed in Figures 28 and 29 that the crossover temperature occurs earlier than expected and that the model starts to lose its accuracy after 240℃.

In an attempt to achieve more accurate results and a crossover temperature close to that reported in the literature, the kinetics were modified within the range given, and then ran in the simulation software. The adsorption term and pre-exponential factors for the 3 reactions were modified using the design specs and data fit tool and documented in Table 22-23.

Table 22-Modified kinetic parameters of Cu/CeO2/ZrO2 catalyst as used by Poto et al.,[56] to produce the kinetic model.

Kinetic Parameters	Values	Units
k_1	$(7.103\cdot10^{-1})\exp(-\frac{3.378\cdot10^{4}}{RT})$	$mol.kg_{cat}^{-1}\cdot s^{-1}\cdot bar^{-1}$
k_2	$(2.75\cdot10^{11})\exp(-\frac{1.35404\cdot10^{5}}{RT})$	$mol.kg_{cat}^{-1}\cdot s^{-1}$
k_3	$(1.416\cdot10^{9})\exp(-\frac{1.11\cdot10^{5}}{RT})$	$mol.kg_{cat}^{-1}\cdot s^{-1}\cdot bar^{-1}$
b_{CO2}	$(6.50\cdot10^{-7})\exp(\frac{6.1190\cdot10^{4}}{RT})$	bar^{-1}
b_{CO}	$(3.857\cdot10^{-3})\exp(\frac{8.802\cdot10^{3}}{RT})$	bar^{-1}
b_{H2O} / $\sqrt{b_{H2}}$	$(3.521\cdot10^{-12})\exp(\frac{1.242\cdot10^{5}}{RT})$	$bar^{-0.5}$

Table 23-The modified pre-exponential factor and activation energy of Cu/CeO2/ZrO2 catalyst using design specs and data fit.

Kinetic Parameters	Values	Units
K_1	4.62e-10	(kmol/kg· s)
K_2	179.063416	(kmol/kg· s)
K_3	5460	(kmol/kg· s)
E_1	-6.54676886	kcal/mol
E_2	17.725679	kcal/mol
E_3	24.40958351	kcal/mol

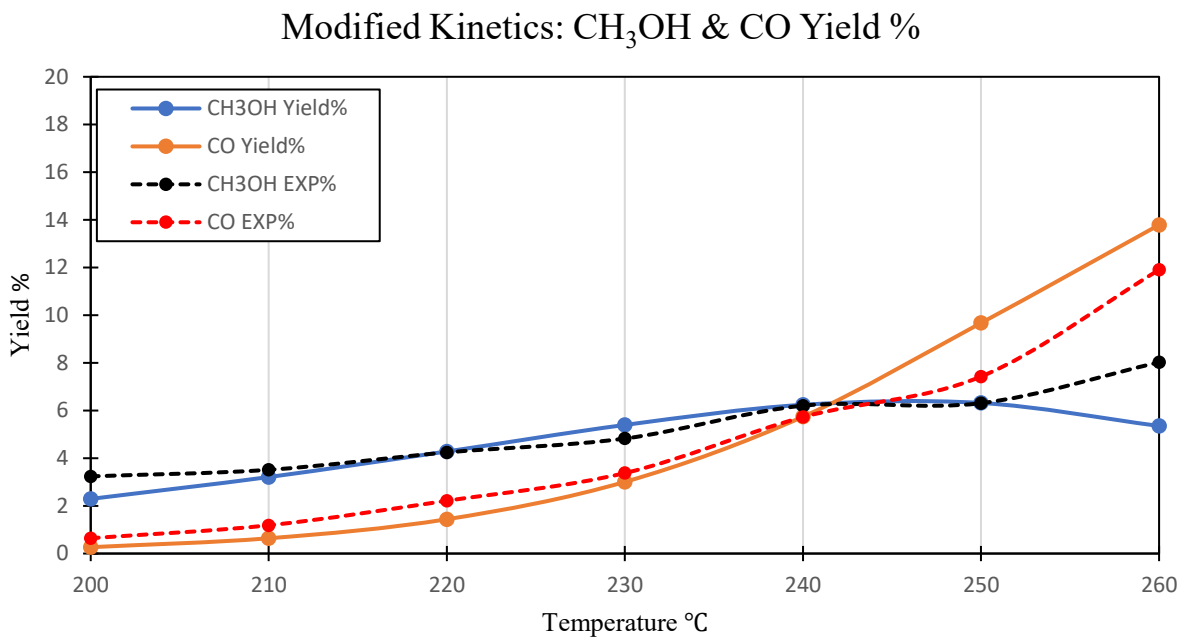

Figure 31- Comparison of the obtained CH_3OH and CO yield from the simulation with modified kinetics with the experimental data reported in the literature at P=30 bars.

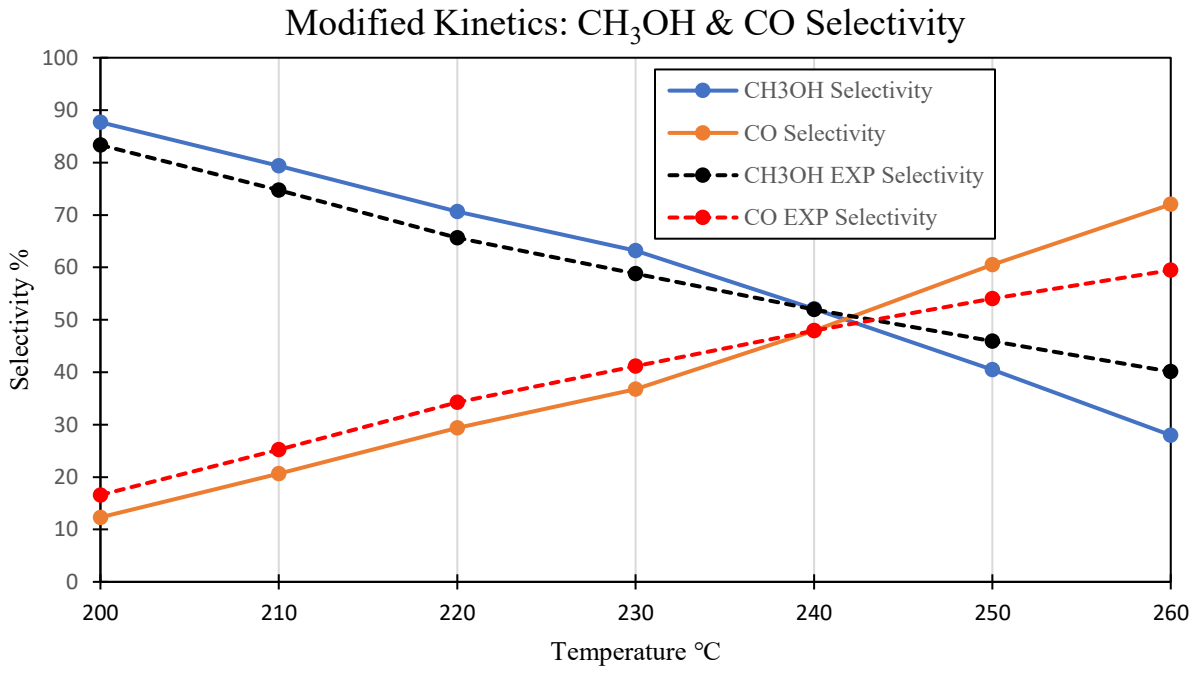

Figure 32-Comparison between the obtained CH_3OH and CO selectivity from the simulation with modified kinetics with the experimental data reported in the literature at P=30 bars.

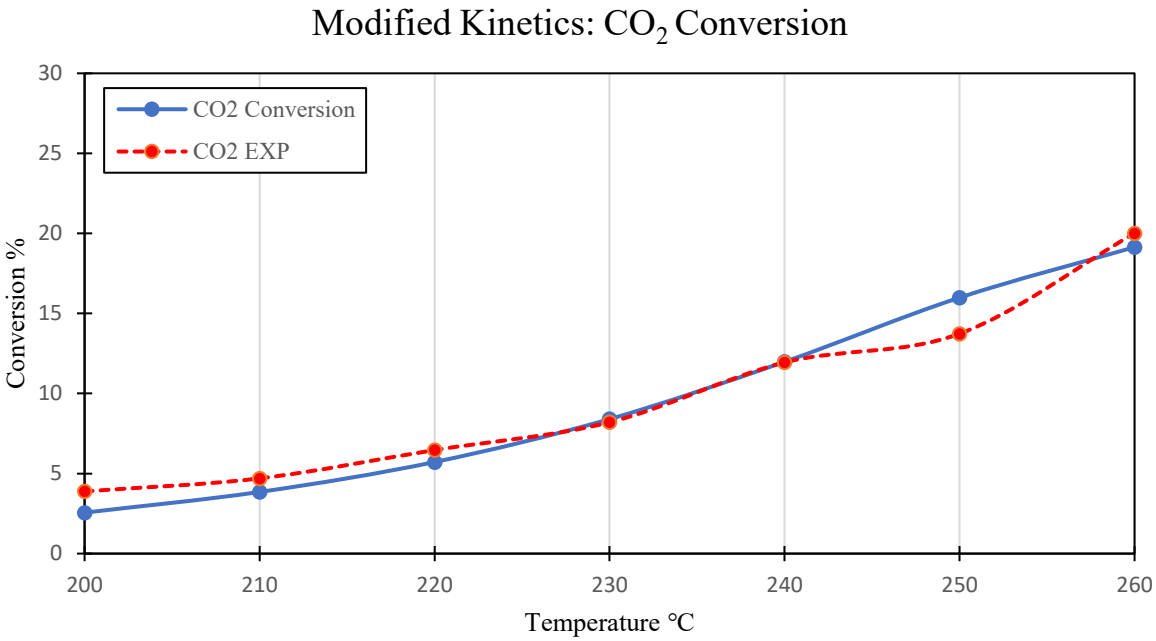

Figure 33-Comparison between the obtained CO_2 conversion from the simulation with modified kinetics with the experimental data reported in the literature at P=30 bars.

Table 24-Error and error percentage of CO_2 results obtained from the modified model.

CO_2 mol/h	**Experimental**	**Model**	**Error**	**Error%**
200	0.021366179	0.0215690547	-0.000202876	-0.95
210	0.021185228	0.0212713010	-0.000086072	-0.41
220	0.020792205	0.0208398922	-0.000047687	-0.23
230	0.020406518	0.0203150042	0.000091514	0.45
240	0.019574679	0.0195528301	0.000021849	0.11
250	0.019176765	0.0188256085	0.000351157	1.83
260	0.0177814	0.0180350652	-0.000253665	-1.43
SSE			0.000000247	

Table 25-Error and error percentage of the CO results obtained from the modified kinetics model.

CO mol/h	Experimental	Model	Error	%Error
200	0.000143160	0.000089418	0.000053742	37.54
210	0.000263646	0.000198773	0.000064873	24.61
220	0.000492390	0.000397618	0.000094772	19.25
230	0.000750701	0.000714755	0.000035946	4.79
240	0.001272879	0.001298073	-0.000025194	-1.98
250	0.001650563	0.002017272	-0.000366709	-22.22
260	0.002645569	0.002980216	-0.000334647	-12.65
SSE			0.000000264	

Table 26-Error and error percentage of the MeOH results obtained from the modified kinetics model.

MeOH mol/h	Experimental	Model	Error	%Error
200	0.000719801	0.000571334	0.000148467	20.63
210	0.000780933	0.000759733	0.000021200	2.71
220	0.000943211	0.000992297	-0.000049086	-5.20
230	0.001072588	0.001200048	-0.000127460	-11.88
240	0.001378915	0.001378904	0.000000011	0.00
250	0.001402479	0.001386926	0.000015553	1.11
260	0.001783720	0.001214526	0.000569194	31.91
SSE			0.000000365	

It can be observed that the simulation with modified kinetics describes the system in a more precise way, where the error for the methanol yield is much less than that for the unmodified kinetics. Even though the error in the CO yield is still relatively high at some temperatures, it is significantly less than that of the unmodified kinetics. Furthermore, it can be observed from the figures that the crossover temperature aligns with what is reported in the literature and the CO_2 conversion and CH_3OH yield results are more accurate as the curves can be seen overlapping at several points. At 250 and 260℃ the kinetic model seems to deviate from the experimental results in terms of CH_3OH and CO yields and this can be related to thermodynamic restrictions implemented in Aspen Plus, since the CO_2 is the only source of carbon being fed and thus the reversible reaction will shift towards producing more CO to satisfy the equilibrium. The kinetic model was further validated by changing the operating pressure between 20 and 40 bars while comparing the simulation result with that of the experimental. The results can be shown below:

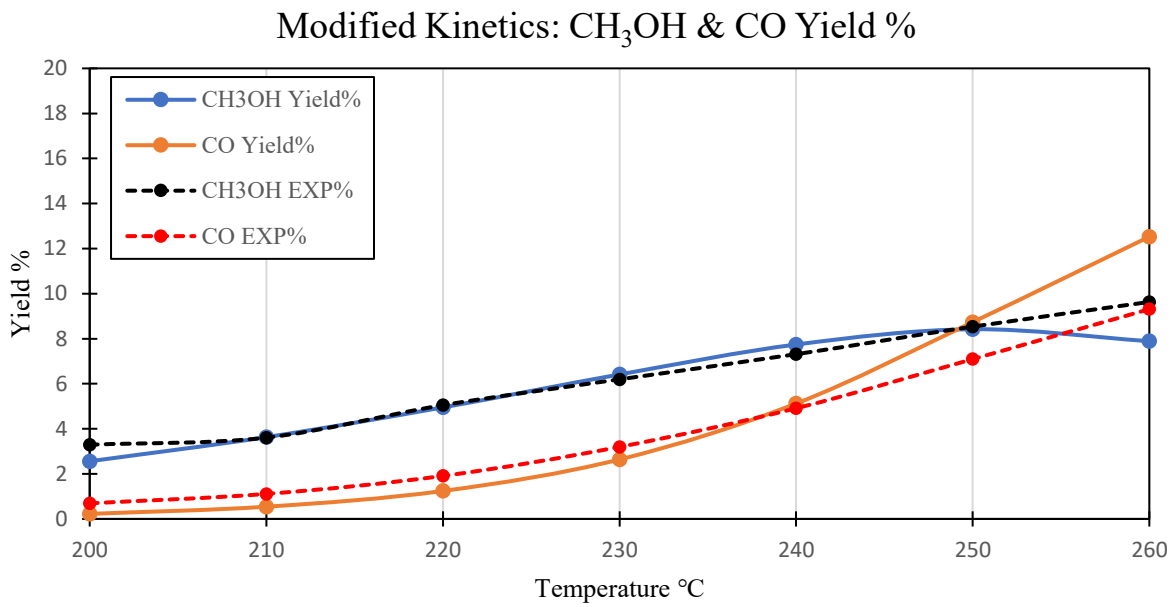

Figure 34-Comparison of the obtained CH_3OH and CO yield from the simulation with modified kinetics with the experimental data reported in the literature at P=40 bars

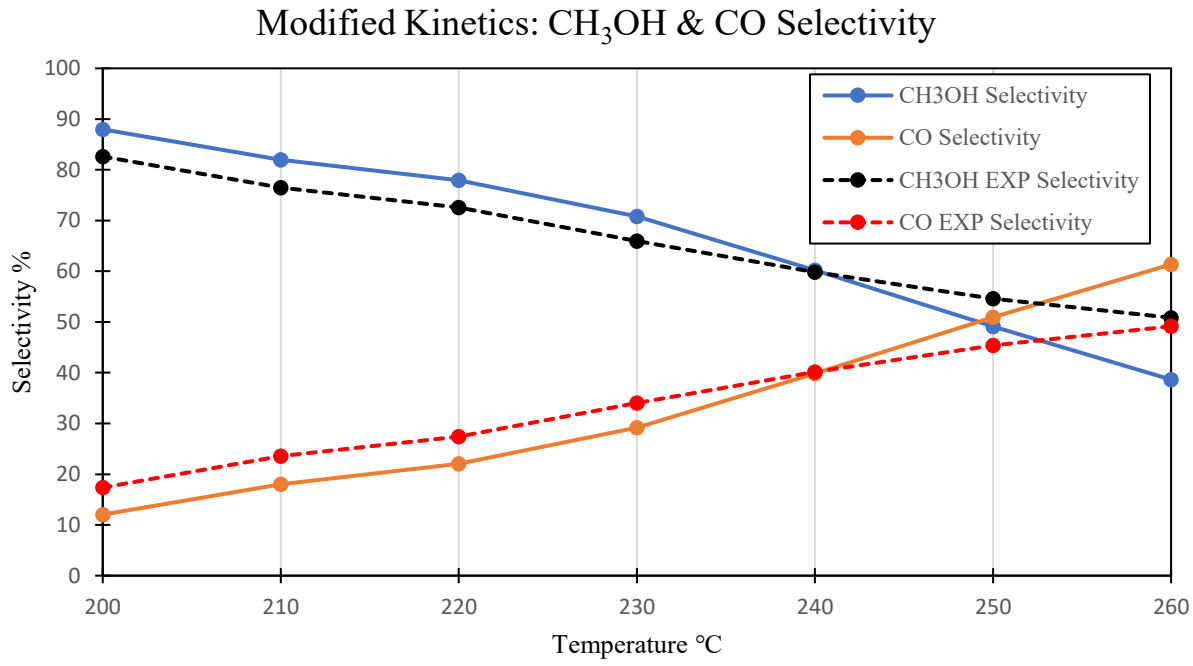

Figure 35-Comparison between the obtained CH_3OH and CO selectivity from the simulation with modified kinetics with the experimental data reported in the literature at P=40 bars.

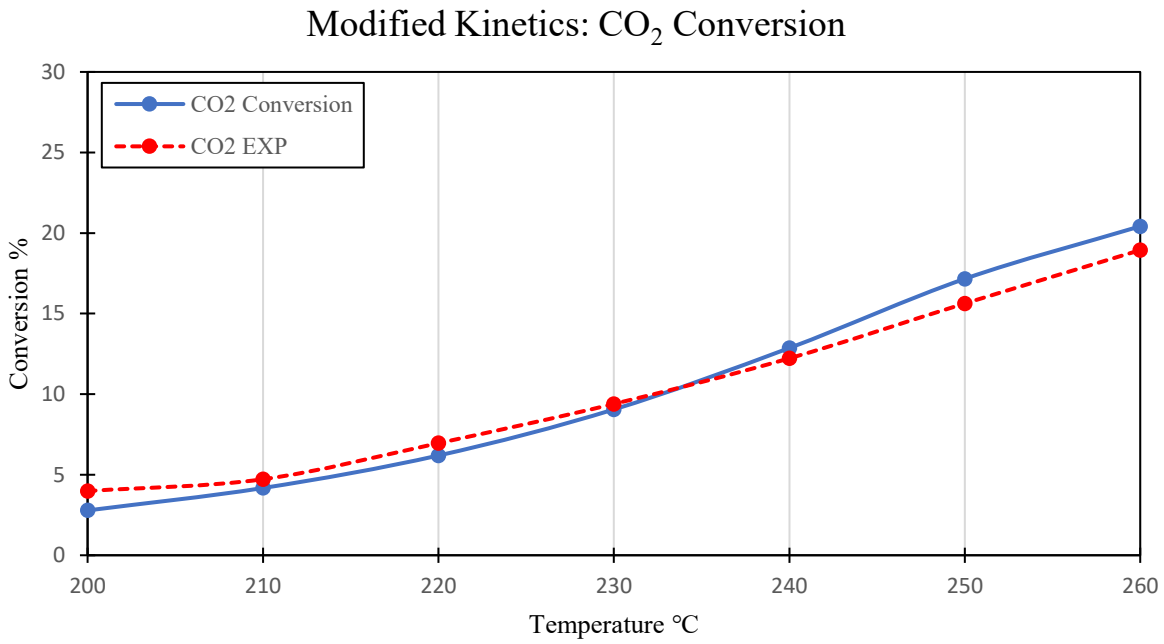

Figure 36-Comparison between the obtained CO_2 conversion from the simulation with modified kinetics with the experimental data reported in the literature at P=40 bars.

The model validation at 40 bars further confirms the accuracy of the kinetic model in describing the system where the CH_3OH and CO yield results are very close to what's reported in the literature, the only inaccuracy lies in the crossover temperature that appears to be earlier than what's reported which could be related to what was mentioned earlier with regards to the thermodynamic limitations. The CO_2 conversion curve is of proximity as well to what have been reported.

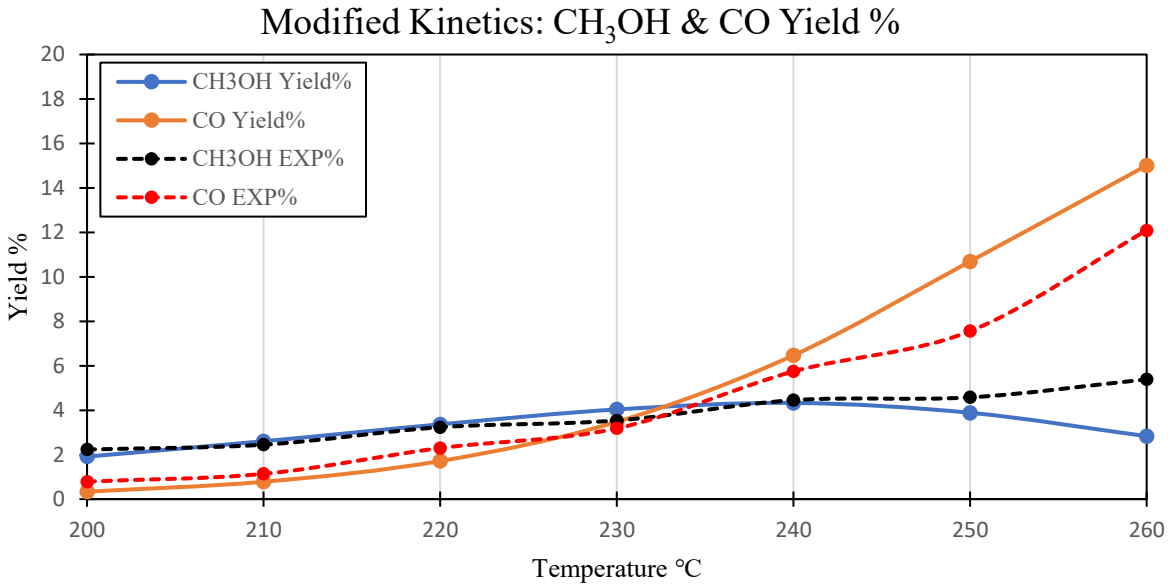

Figure 37-Comparison of the obtained CH_3OH and CO yield from the simulation with modified kinetics with the experimental data reported in the literature at P=20 bars

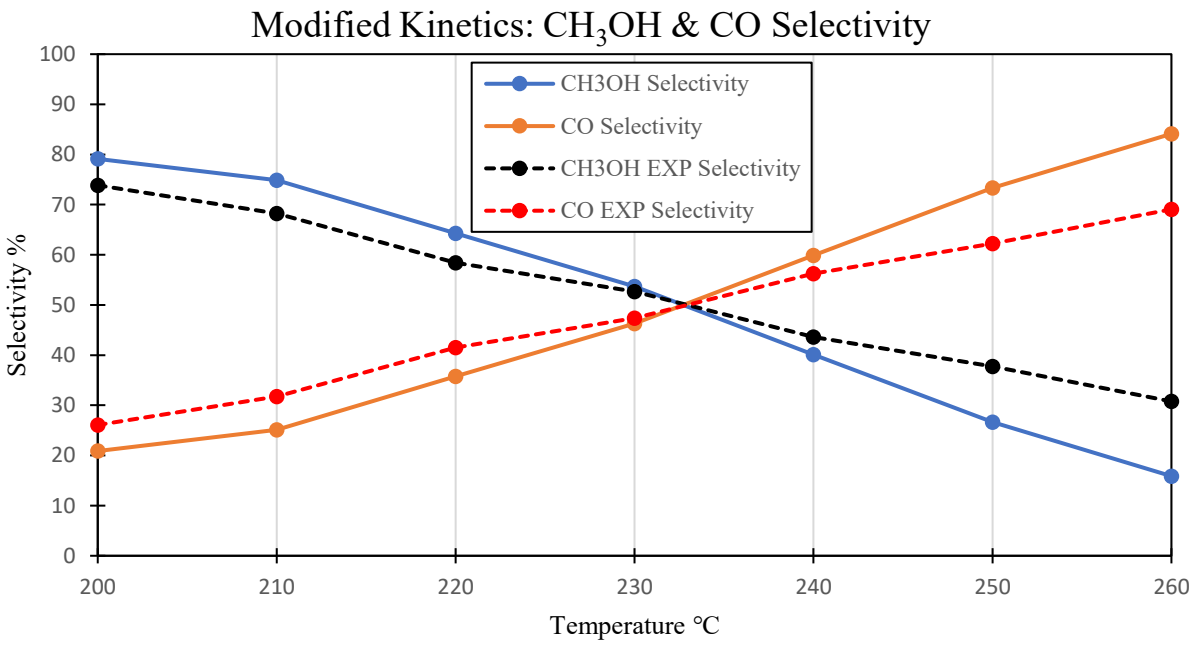

Figure 38-Comparison between the obtained CH_3OH and CO selectivity from the simulation with modified kinetics with the experimental data reported in the literature at P=20 bars

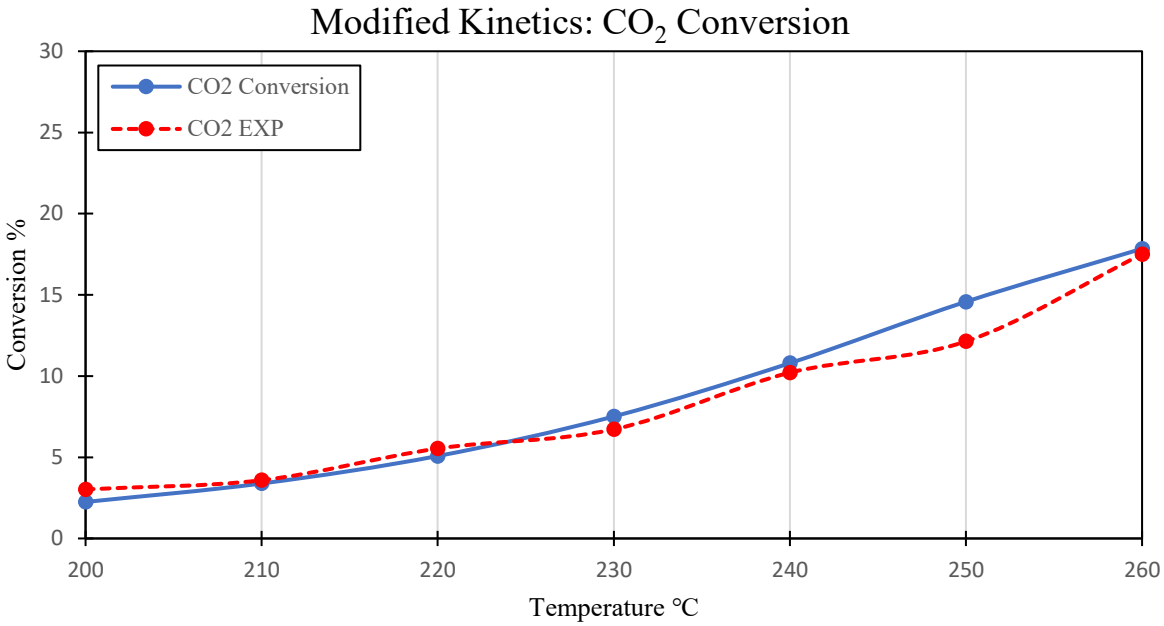

Figure 39-Comparison between the obtained CO_2 conversion from the simulation with modified kinetics with the experimental data reported in the literature at P=20 bars

Finally, the kinetic model results at 20 bars conclude our model validation where the CH_3OH and CO yield results along with the CO_2 conversion results are very close to that reported in the literature and the cross over temperature is represented accurately as well. Since the model validation was a success, the calculated kinetics are going to be adopted for the $CuO/CeO_2/ZrO_2$ performance testing.

When it comes to the selectivity curves for all three pressures that the kinetic model have been tested at, the CH_3OH and CO curves tend to have the same trend in terms of increase or decrease even though the curves don't overlap the literature results.

In an attempt to further enhanced the accuracy of the kinetic model specially when it comes to the CO and MeOH yields, the temperature range was divided into three sections, 200-220℃, 220-240℃, and 240-260℃ and the kinetic model was calculated accordingly as can be seen in the following section.

4.1.1 Kinetic Model for Different Sets of Temperature Range

For the following sections the kinetic models are calculated based on the following adsorption terms in the form of $b_i = A \cdot \exp(B/T)$

Table 27-Adsorption terms considered for the kinetic modeling.

b_i bar^{-1}	A	B
b_{CO2}	6.173×10^{-7}	6817.42
$b_{H2O}/\sqrt{b_{H2}}$	3.521×10^{-12}	14938.658
b_{CO}	3.561×10^{-3}	1014.9146

4.1.1.1 Kinetic Model Over 200-220℃

Table 28- Calculated pre-exponential factor and activation energy over the 200-220 temperature range

Kinetic Parameters	Values	Units
K_1	4.62e-10	(kmol/kg· *s*)
K_2	163	(kmol/kg· *s*)
K_3	5390	(kmol/kg· *s*)
E_1	-5.7789779	kcal/mol
E_2	18.004453	kcal/mol
E_3	24.5834634	kcal/mol

Table 29-Error and error percentage of the CO2 results obtained from the modified kinetics model over 200-220℃...

CO_2 mol/h	**Experimental**	**Model**	**Error**	**Error%**
200	0.021366179	0.0215234651	-0.000157286	-0.74
210	0.021185228	0.0211973027	-0.000012074	-0.06
220	0.020792205	0.0207095082	0.000082697	0.40
SSE			0.000000032	

Table 30-Error and error percentage of the CO results obtained from the modified kinetics model over 200-220℃..

CO mol/h	**Experimental**	**Model**	**Error**	**%Error**
200	0.000143160	0.000114249	0.000028911	20.19
210	0.000263646	0.000240050	0.000023595	8.95
220	0.000492390	0.000510525	-0.000018134	-3.68
SSE			0.000000002	

Table 31-Error and error percentage of the MeOH results obtained from the modified kinetics model over 200-220℃..

MEOH mol/h	Experimental	Model	Error	%Error
200	0.000719801	0.000592093	0.000127709	17.74
210	0.000780933	0.000792454	-0.000011521	-1.48
220	0.000943211	0.001009774	-0.000066564	-7.06
SSE			0.000000021	

4.1.1.2 Kinetic Model Over 220-240℃

Table 32-Calculated pre-exponential factor and activation energy over the 220-240 temperature range

Kinetic Parameters	Values	Units
K_1	4.62e-10	(kmol/kg· *s*)
K_2	163	(kmol/kg· *s*)
K_3	5040	(kmol/kg· *s*)
E_1	-5.62122037	kcal/mol
E_2	18.4906144	kcal/mol
E_3	26.74167586	kcal/mol

Table 33-Error and error percentage of CO_2 results obtained from the modified kinetics model over 220-240℃.

CO_2 mol/h	Experimental	Model	Error	Error%
220	0.020792205	0.0208647891	-0.000072584	-0.35
230	0.020406518	0.0203493364	0.000057182	0.28
240	0.019574679	0.0195588277	0.000015851	0.08
SSE			0.000000009	

Table 34-Error and error percentage of CO results obtained from the modified kinetics model over 220-240℃.

CO mol/h	Experimental	Model	Error	%Error
220	0.000492390	0.000401594	0.000090796	18.44
230	0.000750701	0.000711331	0.000039369	5.24
240	0.001272879	0.001308017	-0.000035138	-2.76
SSE			0.000000011	

Table 35-Error and error percentage of MeOH results obtained from the modified kinetics model over 220-240℃.

MEOH mol/h	Experimental	Model	Error	%Error
220	0.000943211	0.000963424	-0.000020213	-2.14
230	0.001072588	0.001169139	-0.000096551	-9.00
240	0.001378915	0.001362962	0.000015953	1.16
SSE			0.000000010	

4.1.1.3 Kinetic Model Over 240-260℃

Table 36-Calculated pre-exponential factor and activation energy over the 240-260 temperature range

Kinetic Parameters	Values	Units
K_1	4.62e-10	(kmol/kg· s)
K_2	163	(kmol/kg· s)
K_3	5040	(kmol/kg· s)
E_1	-5.62122037	kcal/mol
E_2	18.4906144	kcal/mol
E_3	26.74167586	kcal/mol

Table 37-Error and error percentage of CO_2 results obtained from the modified kinetics model over 200-220℃.

CO2	Experimental	Model	Error	Error%
240	0.019574679	0.0196727354	-0.000098056	-0.50
250	0.019176765	0.0190083847	0.000168381	0.88
260	0.0177814	0.0182294006	-0.000448000	-2.52
SSE			0.000000239	

Table 38-Error and error percentage of CO results obtained from the modified kinetics model over 240-260℃.

CO	Experimental	Model	Error	%Error
240	0.001272879	0.001173043	0.000099836	7.84
250	0.001650563	0.001804630	-0.000154067	-9.33
260	0.002645569	0.002715497	-0.000069928	-2.64
SSE			0.000000039	

Table 39-Error and error percentage of MeOH results obtained from the modified kinetics model over 220-260℃.

MEOH	Experimental	Model	Error	%Error
240	0.001378915	0.001384028	-0.000005113	-0.37
250	0.001402479	0.001416792	-0.000014313	-1.02
260	0.001783720	0.001284909	0.000498811	27.96
SSE			0.000000249	

Dividing the temperature among three sets allowed us to improve the accuracy of the kinetic model significantly, especially for the CO yield results where the percentage error now is within a more reasonable range. The improvement in accuracy also reflected an enhancement of the methanol yield and CO_2 conversion values.

Next, as discussed in the methodology section, the kinetic model for the system described by the CO_2 and RWGS reactions is calculated, and the results are displayed below.

4.1.2 Kinetic Model for the System Excluding the CO HYD Reaction

Table 40-Calculated pre-exponential factor and activation energy over a temperature range of 200-260℃

Kinetic Parameters	Values	Units
K_1	4.62e-10	(kmol/kg· s)
K_2	163	(kmol/kg· s)
E_1	-5.64797927	kcal/mol
E_2	18.49502	kcal/mol

Table 41-Error and error percentage of CO_2 results obtained from the modified kinetics model over 200-260℃.

CO_2 mol/h	Experimental	Model	Error	Error%
200	0.021366179	0.0215511320	-0.000184953	-0.87
210	0.021185228	0.0212714571	-0.000086229	-0.41
220	0.020792205	0.0208401548	-0.000047949	-0.23
230	0.020406518	0.0203052769	0.000101241	0.50
240	0.019574679	0.0195525823	0.000022097	0.11
250	0.019176765	0.0188338964	0.000342869	1.79
260	0.0177814	0.0182076034	-0.000426203	-2.40
SSE			0.000000354	

Table 42-Error and error percentage of CO results obtained from the modified kinetics model over 200-260℃.

CO mol/h	Experimental	Model	Error	%Error
200	0.000143160	0.000087341	0.000055819	38.99
210	0.000263646	0.000198617	0.000065029	24.67
220	0.000492390	0.000397355	0.000095035	19.30
230	0.000750701	0.000704482	0.000046219	6.16
240	0.001272879	0.001298321	-0.000025442	-2.00
250	0.001650563	0.002008984	-0.000358421	-21.72
260	0.002645569	0.002817678	-0.000172108	-6.51
SSE			0.000000177	

Table 43-Error and error percentage of MeOH results obtained from the modified kinetics model over 200-260℃.

MEOH mol/h	Experimental	Model	Error	%Error
200	0.000719801	0.000591334	0.000128467	17.85
210	0.000780933	0.000759733	0.000021200	2.71
220	0.000943211	0.000992297	-0.000049086	-5.20
230	0.001072588	0.001220048	-0.000147460	-13.75
240	0.001378915	0.001378904	0.000000011	0.00
250	0.001402479	0.001386926	0.000015553	1.11
260	0.001783720	0.001204526	0.000579194	32.47
SSE			0.000000377	

As can be seen from the mole flow values reported and the relative error percentage, the results are very similar to that reported for the system of three reaction which have been already validated and thus the results are reliable, and the kinetic model calculated can be used to describe the CO_2 conversion to methanol properly.

4.2 $CuO/CeO_2/ZrO_2$ and $CuO/ZnO/Al_2O_3$ Performance Comparison

The comparison between the two catalysts is done in ASPEN PLUS V12 software. The simulation environment adopted for our comparison is taken from pre-existing models provided by Aspen Plus, two of these models are the lurgi two-stage methanol synthesis process model and ICI synetix methanol process model [85].

4.2.1 Lurgi Two-Stage Methanol Synthesis Process

The Lurgi two-stage methanol synthesis process is regarded as a large-scale process which transforms syngas into crude methanol through a two-stage reactor system. It is a reliable technology known for its minimal production expenses at maximum capacity due to its efficient energy integration and minimal

recycling requirements during the synthesis process. This process is represented in the flow diagram shown below:

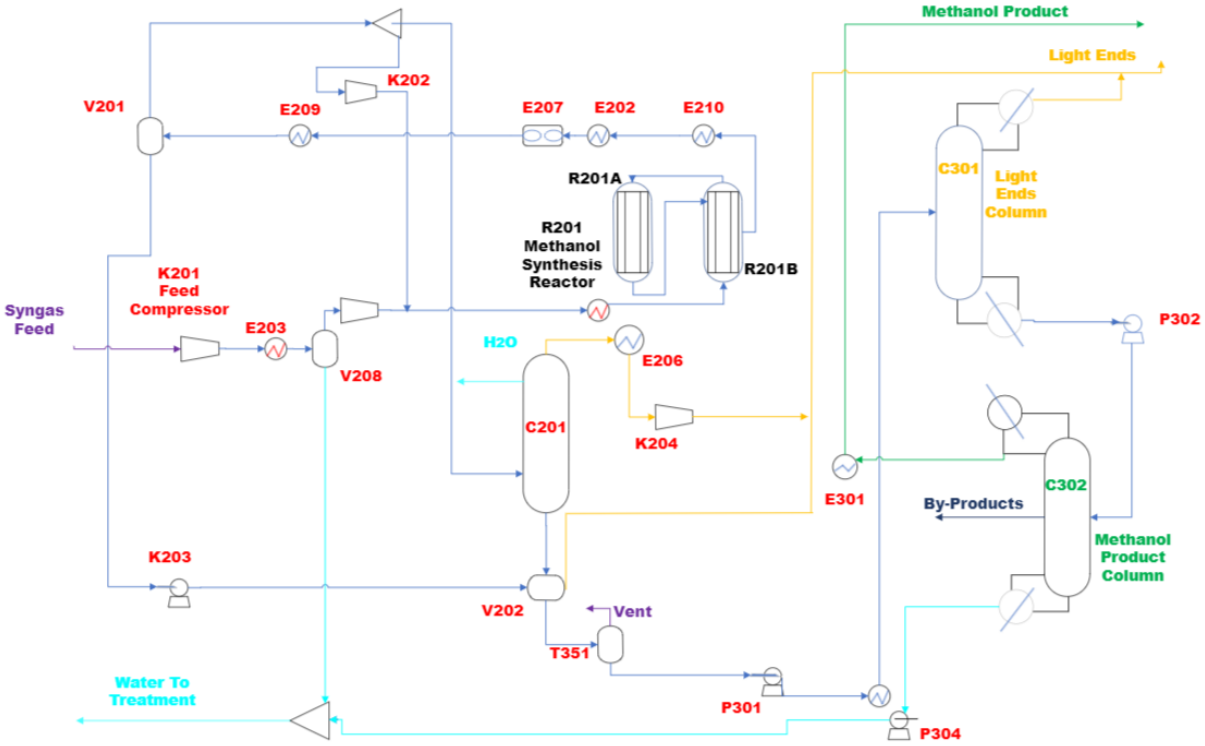

Figure 40-Lurgi Two-Stage Methanol Synthesis Process

The sulfur free syngas having a molar composition of 7% CO_2, 23% CO, and 68% H_2 is fed to the process where it undergoes a series of compression and heating stages. A condensate stream is taken off downstream by the compressor knockout drum (V208), and the gas is mixed with the cooler recycled syngas. The streams is heated again before going into the methanol synthesis reactor (R201) where the CO_2 undergoes conversion. The reacted gas is then cooled, and liquids are separated by condensation. A fraction of the gas is recycled back into the feed stream,0.029, while the rest of the product stream is further purified by passing through the purge gas scrubber (C201), light ends column (C301) and methanol product column (C302).

The methanol synthesis reactor is formed of two stages. The fresh feed is introduced into the second stage (R201B) and heated to a temperature between 250°C and 270°C. This heated feed then enters the first stage (R201A) on the tube side. The first stage is known as the isothermal stage because it operates at nearly constant temperatures since it utilizes boiling water on the shell side to control its temperature. The steam pressure on the shell side is responsible for maintaining the temperature in this stage. The effluent from the first stage (R201 A) is directed back to the catalyst-packed shell side of the second stage (R201 B), where it flows countercurrent to the syngas flowing through the tube side. This arrangement cools the product stream, leading to increased conversion rates.

R201 A is modeled as an ideal, multi-tube plug-flow reactor with constant heat transfer temperature. The heat transfer coefficient has been set to a high value typical for systems with rapid boiling. Additionally, the tube-side heat transfer is expected to be very high due to the turbulent flow across the packing. The pressure drop across the tubes is determined using Ergun's equation, which is commonly used for flow calculations in packed beds.

As for R201 B, it is represented as a single-tube reactor with counter-current cooling. The RPLUG model takes into consideration the counter-current coolant flow and calculates the temperature of the coolant feed based on a specified outlet temperature. To ensure the actual inlet temperature of the coolant feed matches the temperature calculated by the reactor model, an external design specification is employed to adjust the specified coolant outlet temperature. Figure 41 below shows the R201 methanol synthesis reactor in the Aspen Plus environment. To-R201 is the feed stream going in the methanol synthesis reactor, where To-R201 and To-R101A streams have the same mass flow rate, 1737 tonne/hr, and pressure 91.66 bars, but different temperature. The product of the first stage (R201-A) is fed to the second stage (R201-B) that yields the final product stream X-R201B.

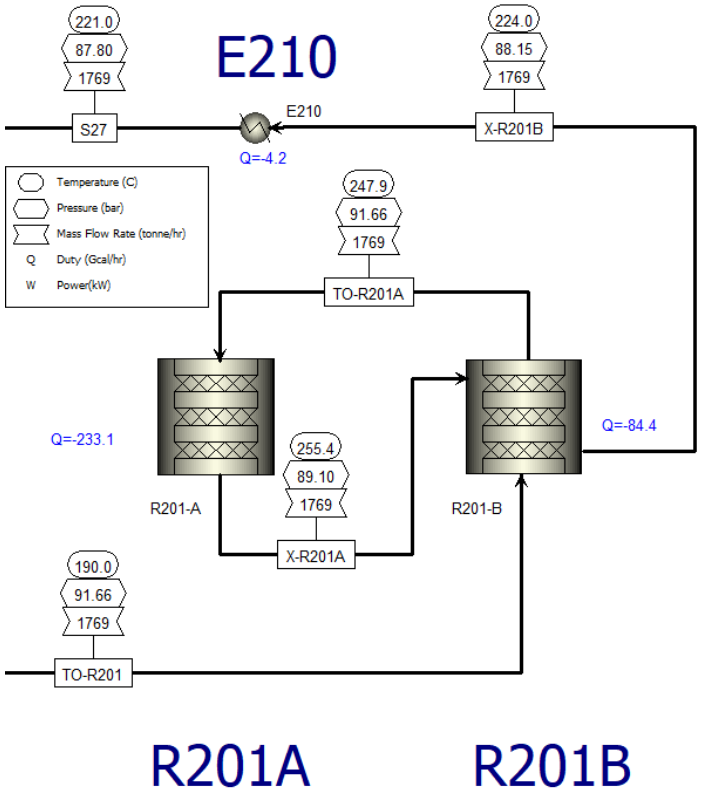

Figure 41-Lurgi Two- Stage Methanol Synthesis Reactor

The kinetic model for the $CuO/CeO_2/ZrO_2$ calculated in Chapter 4, Table 23, was implemented in the Aspen Plus simulation model to test its performance compared to the commercial catalyst. The results obtained from the simulation are documented below.

Table 44-Syngas feed composition

Component	Mole Flow kmol/hr
H_2	30755.79
N_2	142.79
CO	10424.7
CO_2	3112.94
CH_3OH	0
CH_4	997.33
H_2O	111.02

Table 45-Comparison of the performance of the commercial catalyst and $CuO/CeO_2/ZrO_2$

$CuO/CeO_2/ZrO_2$				$CuO/ZnO/Al_2O_3$			
Mole Flows kmol/hr	To-R201 Feed	X-R201A	X-R201B	Mole Flows kmol/hr	To-R201 Feed	X-R201A	X-R201B
H_2	114787	90252	86582.2	H_2	120834	96527.7	92813.2
N_2	4798.61	4798.61	4798.61	N_2	4798.61	4798.61	4798.61
CO	13987	5021.08	3672.03	CO	13620.4	5244.4	3293.83
CO_2	10638.4	8437.12	8113.19	CO_2	11785	9266.9	9329.13
CH_3OH	596	11763.2	13436.2	CH_3OH	626.477	11520.6	13408.9

The difference in the mole flows in the feed stream, To-R201, for the two catalysts is a result of the recycled gas stream as explained earlier, and thus it depends on the reactor performance and in our case the catalyst performance.

From the results present, it can be observed that $CuO/CeO_2/ZrO_2$ have a better performance in terms of CO_2 conversion and methanol yield when compared to the commercial catalyst. The $CuO/CeO_2/ZrO_2$ achieved a 23.74% CO_2 conversion rate compared to 20.84% conversion rate of $CuO/ZnO/Al_2O_3$. Furthermore, it can be seen in Table 45 that the CO_2 value increased in the final product stream, X-R201 B, over the commercial catalyst which is attributed to RWGS being favored at high temperatures over the commercial catalyst whereas $CuO/CeO_2/ZrO_2$ showed consistency in CO_2 conversion due to its CO hydrogenation ability and better methanol selectivity.

4.2.1.1 Simulation Model Modification

In an attempt to increase the methanol yield and selectivity, several sensitivity analysis were performed on both systems containing the commercial $CuO/ZnO/Al_2O_3$ and $CuO/CeO_2/ZrO_2$ catalyst. One particular sensitivity analysis was done on the first stage reactor R201-A, whose thermal fluid temperature was 265 ℃ , by varying it between 250 and 265℃ . A notable increase in CO_2 conversion and methanol yield in the R201- A reactor was noticed at T = 255℃ which can be attributed to the fact that methanol selectivity and CO_2 conversion are higher at lower temperatures as shown in section 3.1.2 in chapter-3. The graphs representing the sensitivity analysis for the two catalysts are shown below.

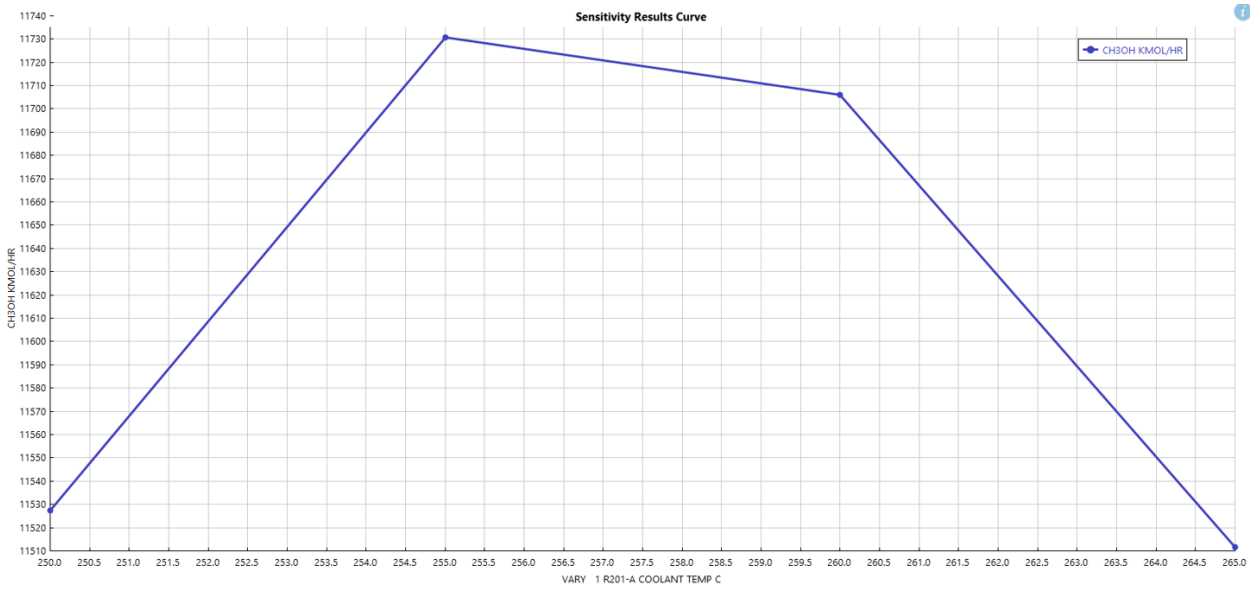

Figure 42-Sensitivity Analysis of methanol yield with respect to the first stage reacto thermal fluid temperature for $CuO/ZnO/Al_2O_3$

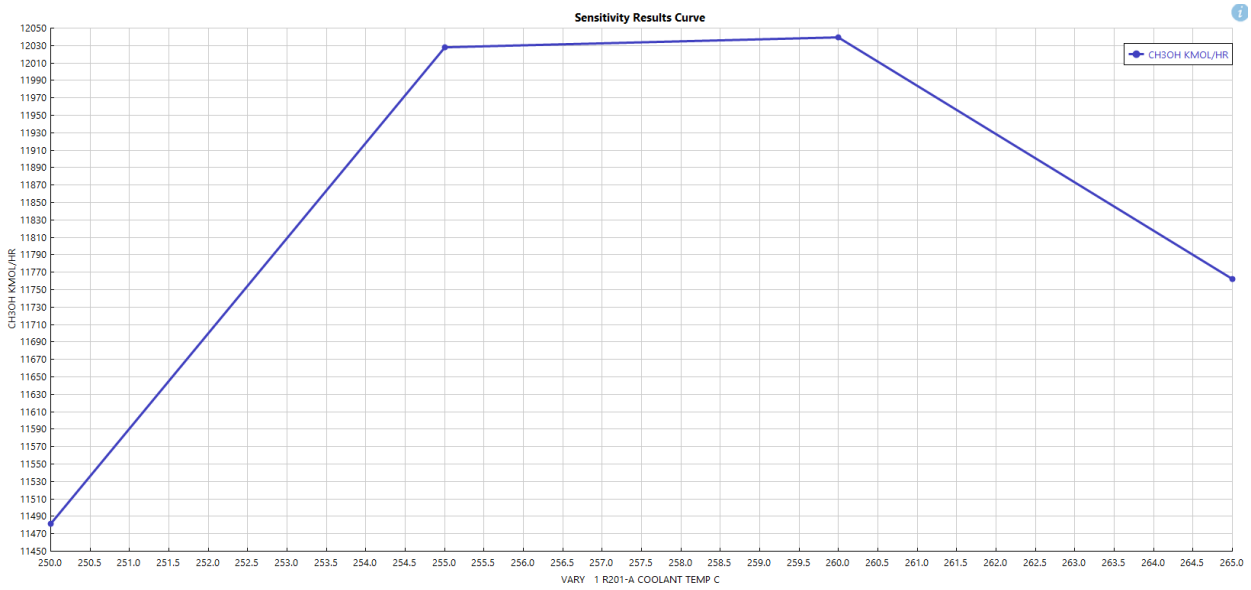

Figure 43-Sensitivity Analysis of methanol yield as a function of the first stage reactor thermal fluid temperature for CuO/CeO2/ZrO2

It can be seen from the Figure 43 that 260℃ was the optimal temperature at which the R201-A yielded the highest methanol yield. However, we decided to go with 255℃ since by doing so the temperature of the product stream, X-R201-B drops below 221 ℃ as can be seen in Figure 44 which permits the removal of the cooler E201, Figure 41, and thus reduces both capital and operational.

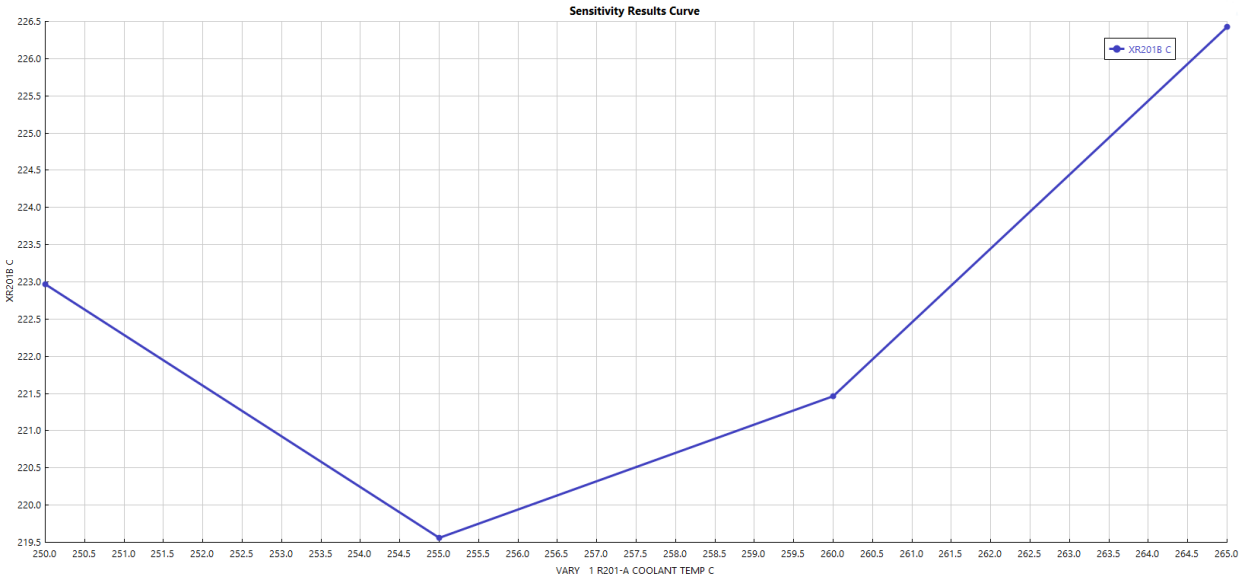

Figure 44-Sensitivity analysis of the product stream temperature as a function of reactor R201-A fluid temperature

4.2.1.2 Energy and Economic Study

Table 46 below demonstrates the energy consumption of the two-stage Lurgi methanol synthesis process operating with the commercial catalyst in comparison to the $Cu/CeO_2/ZrO_2$ in terms of hot and cold utilities. The difference in energy between the two systems is counted as energy savings if the $Cu/CeO_2/ZrO_2$ is considered as a replacement for the commercial catalyst. As can be seen, the process operating with the $Cu/CeO_2/ZrO_2$ catalyst seems to be more energy efficient except in the area of medium pressure (MP) steam. Whereas the low pressure (LP) and high pressure (HP) steams demonstrate better results than the commercial counterpart.

Table 46-Energy consumption comparison between the commercial $Cu/ZnO/Al_2O_3$ and $Cu/CeO_2/ZrO_2$

Energy: Gcal/hr	**$CuO/ZnO/Al_2O_3$**	**$CuO/CeO_2/ZrO_2$**	**Energy Savings**
MP Steam	286	287.4	-1.4
LP Steam	53.94	53.9	0.04
HP Steam	289.9	277.6	12.3
Total Hot Utilities	629.84	618.9	10.94
Air	637.5	632.7	4.8
MP Steam Generation	14.07	7.283	6.787
Cooling Water	95.45	92.52	2.93
Total Cold Utilities	747.02	732.503	14.517

Table 47 below sums up the utilities in four categories, electricity, cooling water, and steam at 100 and 400 PSI. The rate of those utilities exerted by the two-stage Lurgi methanol process is the sum of the rates of all the equipment involved in the process. As can be seen the methanol synthesis process operating with the $CuO/CeO_2/ZrO_2$ catalyst displays lower utility rates and consequently lower costs where savings up to $4,872,355per year have been calculated.

Table 47-Utilities Rates and Cost

Utilities	**$CuO/ZnO/Al_2O_3$**	**$CuO/CeO_2/ZrO_2$**	**Savings**	**Savings/ year**
Electricity	58661.8 kW	57192.2 kW	1469.6 kW 1.469 MW	12697.34 MW
Cooling water	17.7746 MGal/hr	17.4307 klb/hr	0.3439 MGal/hr	2971.296 MGal
Steam @100 PSI	1517.84 klb/hr	1523.89 klb/hr	-6.05 klb/hr	-52272 klb
Steam @400 PSI	992.173 klb/hr	953.056 klb/hr	39.117 klb/hr	337970.99 klb
Cost	**$CuO/ZnO/Al_2O_3$**	**$CuO/CeO_2/ZrO_2$**	**Savings**	**Savings/ year**
Electricity	$ 4546.29 /hr	$ 4432.39 /hr	$ 113.9 /hr	$ 984,096
Cooling water	$ 2132.95 /hr	$ 2091.68 /hr	$ 41.27 /hr	$ 356,572.8
Steam @100 PSI	$ 12355.2 /hr	$ 12404.44 /hr	$ -49.24 /hr	$ -425,433.6
Steam @400 PSI	$ 11618.3 /hr	$ 11160.3 /hr	$ 458 /hr	$ 3,957,120
Total			$ 563.93 /hr	$ 4,872,355.2

Though the using the $Cu/CeO_2/ZrO_2$ catalyst results in a much lower energy requirement, the energy requirement for the overall process is quite high. A heat integration network was investigated to further reduce the energy requirement for the overall process first considering the unmodified process, and is represented in Figure 45 below. Two streams are shown “hot streams” in red, and “cold streams” in blue, where a heat exchanging network exists between those streams. The cooling water stream (20-25℃), the

first blue line, represents the cold utility used whereas the fired heat (1000℃), last red line, represents the hot utility used. The heat exchange between the hot and cold streams is represented by grey dots where heat always transfers from the hot stream to the cold streams. A heat exchange between the hot utility and the cold streams is represented by red dots and a heat exchange between the cold utility and the hot streams is represented by a blue. Both the hot and cold utility streams were split to accommodate the energy demand of the system and make up for the insufficient heat transfer in between the streams. The temperature approach, which is the minimum temperature allowed to exist between hot and cold streams, was taken to be 10 ℃.

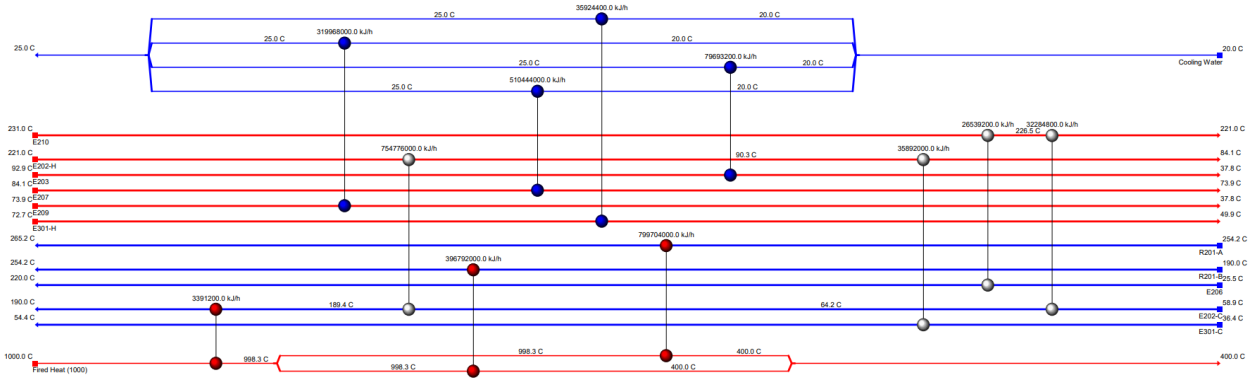

Figure 45-Heat Integration Design

Both hot streams E202-H and E210 provided the heat demand for cold stream E202-C. Furthermore, the remaining energy of E202-H and E210 was sufficient to satisfy the heat demand for cold streams E301-C and E206. Due to the high temperature requirement of the reactor R201-A and R201-B, a fired heat utility had to be used to satisfy their heating demand. Whereas for hot streams E203, E207, E209, and E301-H their cooling demand was provided by cooling water due to temperature approach limitations.

Table 48-Process Streams Inlet and Outlet Temperature

Equipment	Temperature in ℃	Temperature out ℃	Stream Type
E203	92.9	37.8	Hot Stream
E210	231	221	Hot Stream
E202-H	221	84.1	Hot Stream
E301-H	72.7	49.9	Hot Stream
E209	73.9	37.8	Hot Stream
E207	84.1	73.9	Hot Stream
E206	25.5	220	Cold Stream
E202-C	58.9	190	Cold Stream
E301-C	36.4	54.4	Cold Stream
R201-B	190	254.2	Cold Stream
R201-A	254.2	265.2	Cold Stream

Table 49-Utility Streams Inlet and Outlet Temperatures

Utility	Temperature in ℃	Temperature out ℃	Utility Type
Cooling Water	20	25	Cold Utility
Fired Heat (1000)	1000	400	Hot Utility

Tables 50 and 51below demonstrate the energy demand and the relative cost of the heat integration design.

Table 50-Heat Network Design Performance and Cost Index

Energy Gcal/hr	Heat Network Design	Cost Index
Heating	286.78	$5097/hr
Cooling	226.11	$200.98/hr
Number of Units	11	$5299.2/hr
Capital Cost		$33060000

As can be seen when compared to Tables 46 and 47 the heating and cooling energy demand and their relative price decrease significantly ($20808/hr in savings) upon performing the heat network design thus lowering the OPEX of the plant. Table 51 shows that an increase in CAPEX (+$33060000) should be accounted for when performing a heat integration design, price of the heat exchangers used, however the cost saving from the OPEX will eventually offset the extra cost in CAPEX regardless of the catalyst used.

Table 51 demonstrates the total equipment cost compromised of the equipment delivered cost and the installation cost for the two-stage Lurgi methanol synthesis process over the $CuO/CeO_2/ZrO_2$ catalyst. As mentioned before in section 4.3.1.1 the reduction in the first stage reactor thermal fluid temperature to 255℃ permits the removal of the cooling unit E-210 which in turn leads to the reduced equipment cost as can be seen in the table below.

Table 51-The effect of modifying the thermal fluid temperature of the R201 A reactor over the equipment cost.

Equipment Cost	T-R201 A = 265 ℃	T-R201 A = 255 ℃	Savings
Equipment Delivered Cost $	73,039,116	72,873,915	165,201
Installation Cost $	36,652,948	36,456,891	196,057
Total Equipment Cost $	109,692,064	109,330,805	361,258

4.2.1.3 $CuO/CeO_2/ZrO_2$ and $CuO/ZnO/Al_2O_3$ Performance Comparison on a pure CO_2 feed

For this system, only CO_2 hydrogenation and the RWGS reaction were assumed to take place on the surface of the $CuO/CeO_2/ZrO_2$ and thus the kinetic parameters calculated in Table-40 were used to describe the catalyst. The Lurgi-two stage reactor was used in this simulation with the same specifications as the previous sections except that the feed stream consisted mainly of CO_2. The feed compositions are shown below in Table 52, and the flow rates and compositions were taken from a CO_2 capture unit and a hydrogen stream being provided from a water electrolysis unit [87].

Table 52-Total feed composition for the CO_2 conversion unit

Component	Mole Flow kmol/hr
H_2	4401.96
N_2	8.97241
CO_2	1558.52
O_2	1.73152
H_2O	5.51601

Table 53-Comparison of the performance of the commercial catalyst and CuO/CeO2/ZrO2 over a pure CO_2 feed

$CuO/CeO_2/ZrO_2$				$CuO/ZnO/Al_2O_3$			
Mole Flows kmol/hr	To-R201 Feed	X-R201A	X-R201B	Mole Flows kmol/hr	To-R201 Feed	X-R201A	X-R201B
H_2	56473.62	52284	52775.5	H_2	38598.6	34886.3	34243.6
N_2	742.24	742.922	742.92	N_2	628.829	628.877	628.877
CO	421.467	296.634	432.325	CO	281.251	518.904	285.482
CO_2	2106.7	583.928	657.311	CO_2	2752.43	1357.27	1298.33
CH_3OH	39.878	1686.8	1476.56	CH_3OH	98.52	1254.58	1545.71
H_2O	26.1605	1544.07	1471.27	H_2O	20.7686	1416.72	1476.3

As can be seen from the table the CO_2 conversion on the surface of the $CuO/CeO_2/ZrO_2$ catalyst 68.79% is higher than that of the commercial catalyst 52.89% . Furthermore, it appears that the hydrogen consumption over the $CuO/CeO_2/ZrO_2$ is less than that of the commercial catalyst which proves to be economically viable since the H_2 feed is one of the highest expenses in the conversion unit.

4.2.2 ICI Synetix Methanol Synthesis Process Flow

The ICI Synetix low pressure methanol (LPM) process is the most common industrial methanol process worldwide, responsible for more than 30 million metric tons of methanol per year. The downstream methanol recovery processes are the same as the Lurgi-two stage methanol synthesis process and thus the flow diagram is not provided. Below is a graphical representation of the reactor used in the ICI Synetix Methanol Process where the kinetics for both catalysts were input for a clear comparison of their performance.

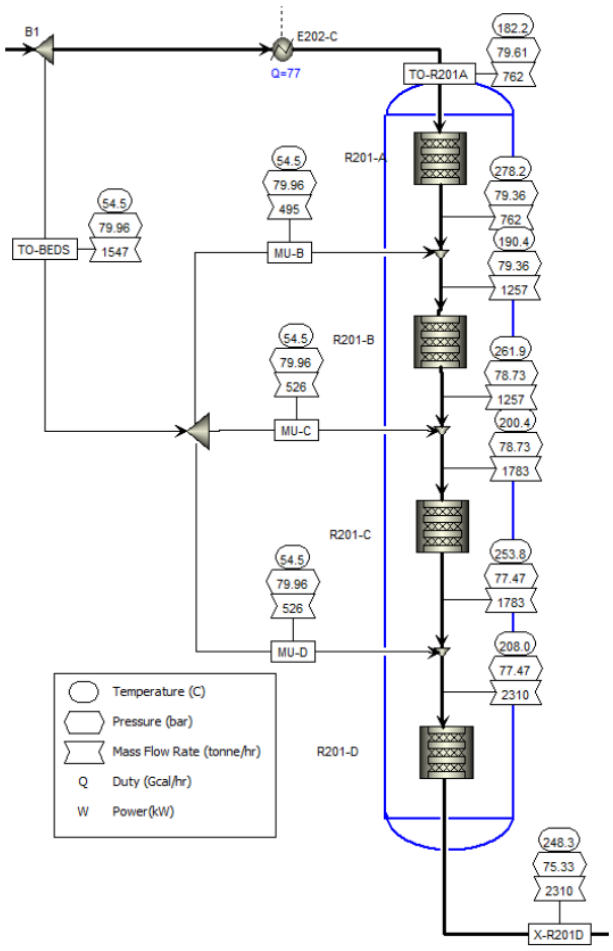

Figure 46-Methanol Synthesis Quench Reactor

In the ICI Synetix process, a four-stage "quench" reactor (R201) is employed for methanol production. The reactor is designed to mitigate the heat generated by the exothermic reactions occurring in the upstream catalyst bed by introducing fresh and cool syngas between the four catalyst beds. The catalyst beds are each represented as ideal, adiabatic, packed plug-flow reactors using the RPLUG rate-based reactor model. The temperature profile is calculated by the model based on the energy balance, accounting for the heat generated by the reactions. Pressure drop is calculated on each stage using Ergun's equations for packed beds. The auto-accelerating nature of the process makes the reactor highly sensitive to variations in the feed temperature, injection rates and the temperature of the quench gas introduced between the beds.

The initial feed introduced to the reactor is at low temperatures and contains very little methanol. The temperature rises to 278°C in the upper stage, and as a result the methanol concentration reaches close to the equilibrium limit. To control the reaction and prevent excessive temperatures, the effluent from the first stage is mixed with cold quench gas, resulting in a reduction of both temperature and the mole fraction of methanol. This process is repeated in each stage of the reactor. The quench rates are adjusted to enable equilibrium at successively lower temperatures in each stage which favors higher methanol concentrations, and thus maximizes the overall production rate and yield in the reactor even though the

reaction rates are faster at higher temperatures. The results showcased in the table below represent a comparison between the two catalysts in study at each “quench” reactor.

Table 54-Comparison of the performance of the commercial catalyst and $CuO/CeO_2/ZrO_2$ over reactor A

$CuO/CeO_2/ZrO_2$			$CuO/ZnO/Al_2O_3$		
Mole Flows kmol/hr	To-R201A	X-R201A	Mole Flows kmol/hr	To-R201A	X-R201A
CO_2	4129.67	3152.24	CO_2	4131.31	3153.97
CO	6602.43	4578.71	CO	6605.07	4581.29
CH_3OH	216.271	3217.42	CH_3OH	216.294	3217.41
H_2	57894.4	50914.7	H_2	57885.1	50905.5
H_2O	30.6485	1008.08	H_2O	30.649	1007.98

Table 55-Comparison of the performance of the commercial catalyst and $CuO/CeO_2/ZrO_2$ over reactor B

$CuO/CeO_2/ZrO_2$			$CuO/ZnO/Al_2O_3$		
Mole Flows kmol/hr	To-R201B	X-R201B	Mole Flows kmol/hr	To-R201B	X-R201B
CO_2	5835.27	5217.71	CO_2	5838.07	5220.72
CO	8868.29	6221.9	CO	8872.59	81368.6
CH_3OH	3357.94	6621.89	CH_3OH	3357.93	6621.59
H_2	88528.5	81383	H_2	88513.3	81368.6
H_2O	1027.99	1645.55	H_2O	1027.89	1645.24

Table 56-Comparison of the performance of the commercial catalyst and CuO/CeO2/ZrO_2 over reactor C

$CuO/CeO_2/ZrO_2$			$CuO/ZnO/Al_2O_3$		
Mole Flows kmol/hr	To-R201C	X-R201C	Mole Flows kmol/hr	To-R201C	X-R201C
CO_2	8068.43	7400.85	CO_2	8072.57	7405.24
CO	10779.6	7982.3	CO	10785.8	7988.46
CH_3OH	6771.18	10236	CH_3OH	6770.9	10235.6
H_2	121348	113750	H_2	121327	113730
H_2O	1666.71	2334.29	H_2O	1666.4	2333.73

Table 57-Comparison of the performance of the commercial catalyst and CuO/CeO2/ZrO2 over reactor D

$CuO/CeO_2/ZrO_2$			$CuO/ZnO/Al_2O_3$		
Mole Flows kmol/hr	To-R201D	X-R201D	Mole Flows kmol/hr	To-R201D	X-R201D
CO_2	10251.6	9595.79	CO_2	10257.1	9601.58
CO	12540	9764.17	CO	12548	9771.8
CH_3OH	10385.3	13816.9	CH_3OH	10384.9	13816.5
H_2	153715	146196	H_2	153688	146170
H_2O	2355.45	3011.22	H_2O	2354.89	3010.4

By analyzing the results obtained for all four reactors (A, B, C, D), it can be observed that the CO_2 and CO conversion along with the CH_3OH yield are very close in value, however the $CuO/CeO_2/ZrO_2$ have a slightly higher conversion rate than that of $CuO/ZnO/Al_2O_3$ and consequently a higher CH_3OH yield. It also should be noted that the H_2 consumption by $CuO/CeO_2/ZrO_2$ is shown to be less than that of the commercial catalyst.

CHAPTER 5: CONCLUSION AND RECOMMENDATIONS

In this study, we successfully developed and evaluated kinetic models for CO_2 and CO hydrogenation reactions using Aspen Plus. The initial model incorporated three key reactions occurring on the catalyst surface: CO2 hydrogenation, CO hydrogenation, and the reverse water-gas shift reaction. Through rigorous assessment using sum square error and error percentage metrics, this model demonstrated superior accuracy and validity compared to existing literature, particularly in representing system behavior. However, it initially exhibited some discrepancies in predicting CO yield. To address this, we refined the model by dividing the temperature range into three distinct segments, resulting in significantly enhanced precision for CO, CO2, and methanol yield predictions.

Further, we explored an alternative kinetic model that specifically excluded the CO hydrogenation reaction. By modifying the reaction rate expression to omit CO hydrogenation and adsorption processes, this model also showed promising results, suggesting its viability for certain applications.

Venturing beyond laboratory scales, the industrial applicability of the $CuO/CeO_2/ZrO_2$ catalyst was assessed against the benchmark commercial catalyst, $CuO/ZnO/Al_2O_3$, within the context of two industrial processes the ICI Synetix methanol synthesis process, and the two-stage Lurgi methanol synthesis process. Notably, the $CuO/CeO_2/ZrO_2$ catalyst surpassed its commercial counterpart, showcasing superior CO_2 conversion rates and methanol yields. Additionally, its methanol selectivity merits special attention. Unlike the commercial catalyst, which exhibited an uptick in CO_2 conversion at elevated temperatures, suggesting a preference for the reverse water gas shift in the two-stage Lurgi process, the $CuO/CeO_2/ZrO_2$ catalyst demonstrated consistent CO_2 conversion to methanol across the temperature spectrum. This highlights its potential to favor CO_2 hydrogenation even under diverse conditions. Furthermore, the two catalysts were tested for CO_2 hydrogenation using a pure CO_2 feed to exclude the effect of CO on the process and to analyze the catalyst performance and selectivity towards CO_2 conversion to methanol. The simulation performed proved once again that the $CuO/CeO_2/ZrO_2$ catalyst demonstrated higher CO_2 conversion than its commercial counterpart in addition to less hydrogen consumption which makes it more economically viable.

Another salient finding was the more energy-efficient nature of the methanol synthesis model employing the $CuO/CeO_2/ZrO_2$ catalyst, underscoring its potential economic and environmental advantages. The sensitivity analysis further amplified this catalyst's promise, indicating that a mere 10°C reduction in the reactor's thermal fluid temperature could lead to significant operational efficiencies — from the elimination of a cooling unit, translating to CAPEX and OPEX savings, to an appreciable boost in methanol yield and CO_2 conversion. The process was further optimized by performing a heat integration design which reduced the OPEX of the system significantly.

Recommendations for Future Works:

1. Scale-up Studies: Given the promising results of the $CuO/CeO_2/ZrO_2$ catalyst at the simulated industrial scale, it would be beneficial to carry out pilot-scale or even full-scale experimental studies to further ascertain its performance in real-world scenarios.

2. Catalyst Longevity: Future research should delve into the lifespan and stability of the CuO/CeO2/ZrO2 catalyst under continuous operation, giving insights into its practical viability for long-term industrial applications.

3. Catalyst Optimization: While the current version of the CuO/CeO2/ZrO_2 catalyst has displayed admirable performance, it would be worthwhile to investigate any potential modifications or improvements to further enhance its efficiency and selectivity.
4. Comprehensive Sensitivity Analysis: The current sensitivity analysis has provided valuable insights. Future works could encompass a broader range of parameters, exploring other operational or design modifications that might yield additional efficiencies or cost savings.
5. Economic Analysis: Given the potential savings observed in CAPEX and OPEX a comprehensive economic analysis, considering factors like return on investment (ROI) and payback period, would provide a clearer picture of the financial benefits of using the CuO/CeO_2/ZrO_2 catalyst on an industrial scale.
6. Environmental Impact Assessment: Alongside economic evaluations, understanding the environmental implications of switching to this catalyst in terms of greenhouse gas emissions, waste generation, and resource consumption would be invaluable for a holistic assessment.

In wrapping up, the results affirm the transformative potential of the CuO/CeO_2/ZrO_2 catalyst, setting the stage for more sustainable, efficient, and economically viable methanol synthesis on an industrial scale. Future endeavors in this field would benefit greatly from these insights, steering us closer to a greener future.

REFERENCES:

[1] H. Ritchie, M. Roser, and P. Rosado, "Energy," OurWorldInData.org, Online Resource, 2022. Accessed: Aug. 23, 2023. [Online]. Available: https://ourworldindata.org/energy

[2] "Statistical Review of World Energy 2022," 2022.

[3] G. A. Olah, A. Goeppert, and G. K. S. Prakash, "Chemical Recycling of Carbon Dioxide to Methanol and Dimethyl Ether: From Greenhouse Gas to Renewable, Environmentally Carbon Neutral Fuels and Synthetic Hydrocarbons," *J. Org. Chem.*, vol. 74, no. 2, pp. 487–498, Jan. 2009, doi: 10.1021/jo801260f.

[4] A. A. Lacis, G. A. Schmidt, D. Rind, and R. A. Ruedy, "Atmospheric CO_2: Principal Control Knob Governing Earth's Temperature," *Science*, vol. 330, no. 6002, pp. 356–359, Oct. 2010, doi: 10.1126/science.1190653.

[5] X. Jiang, X. Nie, X. Guo, C. Song, and J. G. Chen, "Recent Advances in Carbon Dioxide Hydrogenation to Methanol via Heterogeneous Catalysis," *Chem. Rev.*, vol. 120, no. 15, pp. 7984–8034, Aug. 2020, doi: 10.1021/acs.chemrev.9b00723.

[6] M. Höök and X. Tang, "Depletion of fossil fuels and anthropogenic climate change—A review," *Energy Policy*, vol. 52, pp. 797–809, Jan. 2013, doi: 10.1016/j.enpol.2012.10.046.

[7] K. Calvin *et al.*, "IPCC, 2023: Climate Change 2023: Synthesis Report. Contribution of Working Groups I, II and III to the Sixth Assessment Report of the Intergovernmental Panel on Climate Change [Core Writing Team, H. Lee and J. Romero (eds.)]. IPCC, Geneva, Switzerland.," Intergovernmental Panel on Climate Change (IPCC), Jul. 2023. doi: 10.59327/IPCC/AR6-9789291691647.

[8] W. Li *et al.*, "A short review of recent advances in CO_2 hydrogenation to hydrocarbons over heterogeneous catalysts," *RSC Adv.*, vol. 8, no. 14, pp. 7651–7669, 2018, doi: 10.1039/C7RA13546G.

[9] S. Chakravartula Srivatsa and S. Bhattacharya, "Amine-based CO2 capture sorbents: A potential CO2 hydrogenation catalyst," *Journal of CO2 Utilization*, vol. 26, pp. 397–407, Jul. 2018, doi: 10.1016/j.jcou.2018.05.028.

[10] T. A. Semelsberger, R. L. Borup, and H. L. Greene, "Dimethyl ether (DME) as an alternative fuel," *Journal of Power Sources*, vol. 156, no. 2, pp. 497–511, Jun. 2006, doi: 10.1016/j.jpowsour.2005.05.082.

[11] J. T. Farrell, J. Holladay, and R. Wagner, "Co-Optimization of Fuels & Engines: Fuel Blendstocks with the Potential to Optimize Future Gasoline Engine Performance; Identification of Five Chemical Families for Detailed Evaluation," NREL/TP--5400-69009, DOE/GO--102018-4970, 1434413, Apr. 2018. doi: 10.2172/1434413.

[12] Z. Jiang, T. Xiao, V. L. Kuznetsov, and P. P. Edwards, "Turning carbon dioxide into fuel," *Phil. Trans. R. Soc. A.*, vol. 368, no. 1923, pp. 3343–3364, Jul. 2010, doi: 10.1098/rsta.2010.0119.

[13] J. Yang, Y. Yu, T. Ma, C. Zhang, and Q. Wang, "Evolution of energy and metal demand driven by industrial revolutions and its trend analysis," *Chinese Journal of Population, Resources and Environment*, vol. 19, no. 3, pp. 256–264, Sep. 2021, doi: 10.1016/j.cjpre.2021.12.028.

[14] "United Nations Paris Agreement." 2015. [Online]. Available: https://unfccc.int/sites/default/files/english_paris_agreement.pdf

[15] "Statistical Review of World Energy," energy institute, 2023. Accessed: Aug. 23, 2023. [Online]. Available: https://www.energyinst.org/statistical-review/resources-and-data-downloads

[16] H. Ritchie, M. Roser, and P. Rosado, "CO2 and Greenhouse Emissions," Online Resource, 2020. Accessed: Aug. 23, 2023. [Online]. Available: https://ourworldindata.org/co2-and-greenhouse-gas-emissions

[17] G. A. Olah, "Beyond Oil and Gas: The Methanol Economy," *Angew. Chem. Int. Ed.*, vol. 44, no. 18, pp. 2636–2639, Apr. 2005, doi: 10.1002/anie.200462121.

[18] J. R. Fernández, S. Garcia, and E. S. Sanz-Pérez, "CO $_2$ Capture and Utilization Editorial," *Ind. Eng. Chem. Res.*, vol. 59, no. 15, pp. 6767–6772, Apr. 2020, doi: 10.1021/acs.iecr.0c01643.
[19] G. T. Rochelle, "Conventional amine scrubbing for CO2 capture," in *Absorption-Based Post-combustion Capture of Carbon Dioxide*, Elsevier, 2016, pp. 35–67. doi: 10.1016/B978-0-08-100514-9.00003-2.
[20] M. Bui *et al.*, "Carbon capture and storage (CCS): the way forward," *Energy Environ. Sci.*, vol. 11, no. 5, pp. 1062–1176, 2018, doi: 10.1039/C7EE02342A.
[21] D. Y. C. Leung, G. Caramanna, and M. M. Maroto-Valer, "An overview of current status of carbon dioxide capture and storage technologies," *Renewable and Sustainable Energy Reviews*, vol. 39, pp. 426–443, Nov. 2014, doi: 10.1016/j.rser.2014.07.093.
[22] J. M. Valverde, P. E. Sanchez-Jimenez, and L. A. Perez-Maqueda, "Ca-looping for postcombustion CO2 capture: A comparative analysis on the performances of dolomite and limestone," *Applied Energy*, vol. 138, pp. 202–215, Jan. 2015, doi: 10.1016/j.apenergy.2014.10.087.
[23] M. C. Romano *et al.*, "Process simulation of Ca-looping processes: review and guidelines," *Energy Procedia*, vol. 37, pp. 142–150, 2013, doi: 10.1016/j.egypro.2013.05.095.
[24] E. T. Santos *et al.*, "Investigation of a stable synthetic sol–gel CaO sorbent for CO2 capture," *Fuel*, vol. 94, pp. 624–628, Apr. 2012, doi: 10.1016/j.fuel.2011.10.011.
[25] I. Ahmed and H. De Lasa, "CO $_2$ Capture Using Chemical Looping Combustion from a Biomass-Derived Syngas Feedstock: Simulation of a Riser–Downer Scaled-Up Unit," *Ind. Eng. Chem. Res.*, vol. 59, no. 15, pp. 6900–6913, Apr. 2020, doi: 10.1021/acs.iecr.9b05753.
[26] D. Aaron and C. Tsouris, "Separation of CO $_2$ from Flue Gas: A Review," *Separation Science and Technology*, vol. 40, no. 1–3, pp. 321–348, Feb. 2005, doi: 10.1081/SS-200042244.
[27] A. Galadima and O. Muraza, "Catalytic thermal conversion of CO2 into fuels: Perspective and challenges," *Renewable and Sustainable Energy Reviews*, vol. 115, p. 109333, Nov. 2019, doi: 10.1016/j.rser.2019.109333.
[28] A. Cherevotan *et al.*, "*Operando* Generated Ordered Heterogeneous Catalyst for the Selective Conversion of CO $_2$ to Methanol," *ACS Energy Lett.*, vol. 6, no. 2, pp. 509–516, Feb. 2021, doi: 10.1021/acsenergylett.0c02614.
[29] L. C. Grabow and M. Mavrikakis, "Mechanism of Methanol Synthesis on Cu through CO $_2$ and CO Hydrogenation," *ACS Catal.*, vol. 1, no. 4, pp. 365–384, Apr. 2011, doi: 10.1021/cs200055d.
[30] G. A. Olah, G. K. S. Prakash, and A. Goeppert, "Anthropogenic Chemical Carbon Cycle for a Sustainable Future," *J. Am. Chem. Soc.*, vol. 133, no. 33, pp. 12881–12898, Aug. 2011, doi: 10.1021/ja202642y.
[31] X. Zhen and Y. Wang, "An overview of methanol as an internal combustion engine fuel," *Renewable and Sustainable Energy Reviews*, vol. 52, pp. 477–493, Dec. 2015, doi: 10.1016/j.rser.2015.07.083.
[32] R. Sadeghbeigi, "Chapter 8 - Products and Economics," in *Fluid Catalytic Cracking Handbook*, Third., 2012, pp. 169–189. [Online]. Available: https://doi.org/10.1016/B978-0-12-386965-4.00008-2
[33] A. Boretti, "Renewable hydrogen to recycle CO2 to methanol," *International Journal of Hydrogen Energy*, vol. 38, no. 4, pp. 1806–1812, Feb. 2013, doi: 10.1016/j.ijhydene.2012.11.097.
[34] A. Goeppert, M. Czaun, J.-P. Jones, G. K. Surya Prakash, and G. A. Olah, "Recycling of carbon dioxide to methanol and derived products – closing the loop," *Chem. Soc. Rev.*, vol. 43, no. 23, pp. 7995–8048, Jun. 2014, doi: 10.1039/C4CS00122B.
[35] L.-W. Su, X.-R. Li, and Z.-Y. Sun, "The consumption, production and transportation of methanol in China: A review," *Energy Policy*, vol. 63, pp. 130–138, Dec. 2013, doi: 10.1016/j.enpol.2013.08.031.
[36] P. Makoś, E. Słupek, J. Sobczak, D. Zabrocki, J. Hupka, and A. Rogala, "Dimethyl ether (DME) as potential environmental friendly fuel," *E3S Web Conf.*, vol. 116, p. 00048, 2019, doi: 10.1051/e3sconf/201911600048.

[37] S. H. Park and C. S. Lee, “Applicability of dimethyl ether (DME) in a compression ignition engine as an alternative fuel,” *Energy Conversion and Management*, vol. 86, pp. 848–863, Oct. 2014, doi: 10.1016/j.enconman.2014.06.051.
[38] M. L. Alcantara, K. A. Pacheco, A. E. Bresciani, and R. M. Brito Alves, “Thermodynamic Analysis of Carbon Dioxide Conversion Reactions. Case Studies: Formic Acid and Acetic Acid Synthesis,” *Ind. Eng. Chem. Res.*, vol. 60, no. 25, pp. 9246–9258, Jun. 2021, doi: 10.1021/acs.iecr.1c00989.
[39] C. Song, “Global challenges and strategies for control, conversion and utilization of CO2 for sustainable development involving energy, catalysis, adsorption and chemical processing,” *Catalysis Today*, vol. 115, no. 1–4, pp. 2–32, Jun. 2006, doi: 10.1016/j.cattod.2006.02.029.
[40] T. Biswal, K. P. Shadangi, P. K. Sarangi, and R. K. Srivastava, “Conversion of carbon dioxide to methanol: A comprehensive review,” *Chemosphere*, vol. 298, p. 134299, Jul. 2022, doi: 10.1016/j.chemosphere.2022.134299.
[41] K. Ahmad and S. Upadhyayula, “Greenhouse gas CO2 hydrogenation to fuels: A thermodynamic analysis,” *Environmental Progress & Sustainable Energy*, vol. 38, no. 1, pp. 98–111, 2019, doi: 10.1002/ep.13028.
[42] K. Li and J. G. Chen, “CO $_2$ Hydrogenation to Methanol over ZrO $_2$ -Containing Catalysts: Insights into ZrO $_2$ Induced Synergy,” *ACS Catal.*, vol. 9, no. 9, pp. 7840–7861, Sep. 2019, doi: 10.1021/acscatal.9b01943.
[43] M. D. Higham, M. G. Quesne, and C. R. A. Catlow, “Mechanism of CO $_2$ conversion to methanol over Cu(110) and Cu(100) surfaces,” *Dalton Trans.*, vol. 49, no. 25, pp. 8478–8497, 2020, doi: 10.1039/D0DT00754D.
[44] N. J. Azhari *et al.*, “Methanol synthesis from CO2: A mechanistic overview,” *Results in Engineering*, vol. 16, p. 100711, Dec. 2022, doi: 10.1016/j.rineng.2022.100711.
[45] Y.-F. Zhao, Y. Yang, C. Mims, C. H. F. Peden, J. Li, and D. Mei, “Insight into methanol synthesis from CO2 hydrogenation on Cu(111): Complex reaction network and the effects of H2O,” *Journal of Catalysis*, vol. 281, no. 2, pp. 199–211, Jul. 2011, doi: 10.1016/j.jcat.2011.04.012.
[46] Z. Shi, Q. Tan, and D. Wu, “Ternary copper-cerium-zirconium mixed metal oxide catalyst for direct CO2 hydrogenation to methanol,” *Materials Chemistry and Physics*, vol. 219, pp. 263–272, Nov. 2018, doi: 10.1016/j.matchemphys.2018.08.038.
[47] W. Wang, Z. Qu, L. Song, and Q. Fu, “Probing into the multifunctional role of copper species and reaction pathway on copper-cerium-zirconium catalysts for CO2 hydrogenation to methanol using high pressure in situ DRIFTS,” *Journal of Catalysis*, vol. 382, pp. 129–140, Feb. 2020, doi: 10.1016/j.jcat.2019.12.022.
[48] K. Pokrovski, M. Rhodes, and A. Bell, “Effects of cerium incorporation into zirconia on the activity of Cu/ZrO for methanol synthesis via CO hydrogenation,” *Journal of Catalysis*, vol. 235, no. 2, pp. 368–377, Oct. 2005, doi: 10.1016/j.jcat.2005.09.002.
[49] K. Pokrovski and A. Bell, “An investigation of the factors influencing the activity of Cu/CexZr1−xO2 for methanol synthesis via CO hydrogenation,” *Journal of Catalysis*, vol. 241, no. 2, pp. 276–286, Jul. 2006, doi: 10.1016/j.jcat.2006.05.002.
[50] C.-J. Yoo, D.-W. Lee, M.-S. Kim, D. J. Moon, and K.-Y. Lee, “The synthesis of methanol from CO/CO2/H2 gas over Cu/Ce1−xZrxO2 catalysts,” *Journal of Molecular Catalysis A: Chemical*, vol. 378, pp. 255–262, Nov. 2013, doi: 10.1016/j.molcata.2013.06.023.
[51] W. Wang, Z. Qu, L. Song, and Q. Fu, “CO2 hydrogenation to methanol over Cu/CeO2 and Cu/ZrO2 catalysts: Tuning methanol selectivity via metal-support interaction,” *Journal of Energy Chemistry*, vol. 40, pp. 22–30, Jan. 2020, doi: 10.1016/j.jechem.2019.03.001.
[52] B. Ouyang, W. Tan, and B. Liu, “Morphology effect of nanostructure ceria on the Cu/CeO2 catalysts for synthesis of methanol from CO2 hydrogenation,” *Catalysis Communications*, vol. 95, pp. 36–39, May 2017, doi: 10.1016/j.catcom.2017.03.005.
[53] J. Zhu, Y. Su, J. Chai, V. Muravev, N. Kosinov, and E. J. M. Hensen, “Mechanism and Nature of Active Sites for Methanol Synthesis from CO/CO $_2$ on Cu/CeO $_2$,” *ACS Catal.*, vol. 10, no. 19, pp. 11532–11544, Oct. 2020, doi: 10.1021/acscatal.0c02909.

[54] M. Rhodes and A. Bell, “The effects of zirconia morphology on methanol synthesis from CO and H2H2 over Cu/ZrO2Cu/ZrO2 catalystsPart I. Steady-state studies,” *Journal of Catalysis*, vol. 233, no. 1, pp. 198–209, Jul. 2005, doi: 10.1016/j.jcat.2005.04.026.
[55] M. Rhodes, K. Pokrovski, and A. Bell, “The effects of zirconia morphology on methanol synthesis from CO and H2 over Cu/ZrO2 catalystsPart II. Transient-response infrared studies,” *Journal of Catalysis*, vol. 233, no. 1, pp. 210–220, Jul. 2005, doi: 10.1016/j.jcat.2005.04.027.
[56] S. Poto, D. Vico van Berkel, F. Gallucci, and M. Fernanda Neira d’Angelo, “Kinetic modelling of the methanol synthesis from CO2 and H2 over a CuO/CeO2/ZrO2 catalyst: The role of CO2 and CO hydrogenation,” *Chemical Engineering Journal*, vol. 435, p. 134946, May 2022, doi: 10.1016/j.cej.2022.134946.
[57] H. Ren, C.-H. Xu, H.-Y. Zhao, Y.-X. Wang, J. Liu, and J.-Y. Liu, “Methanol synthesis from CO2 hydrogenation over Cu/γ-Al2O3 catalysts modified by ZnO, ZrO2 and MgO,” *Journal of Industrial and Engineering Chemistry*, vol. 28, pp. 261–267, Aug. 2015, doi: 10.1016/j.jiec.2015.03.001.
[58] C. Baltes, S. Vukojevic, and F. Schuth, “Correlations between synthesis, precursor, and catalyst structure and activity of a large set of CuO/ZnO/Al2O3 catalysts for methanol synthesis,” *Journal of Catalysis*, vol. 258, no. 2, pp. 334–344, Sep. 2008, doi: 10.1016/j.jcat.2008.07.004.
[59] M. Behrens *et al.*, “The Active Site of Methanol Synthesis over Cu/ZnO/Al $_2$ O $_3$ Industrial Catalysts,” *Science*, vol. 336, no. 6083, pp. 893–897, May 2012, doi: 10.1126/science.1219831.
[60] S. Kattel, P. J. Ramírez, J. G. Chen, J. A. Rodriguez, and P. Liu, “Active sites for CO $_2$ hydrogenation to methanol on Cu/ZnO catalysts,” *Science*, vol. 355, no. 6331, pp. 1296–1299, Mar. 2017, doi: 10.1126/science.aal3573.
[61] J. Nakamura, Y. Choi, and T. Fujitani, “On the issue of the active site and the role of ZnO in Cu/ZnO methanol synthesis catalysts,” *Topics in Catalysis*, pp. 3--4, Apr. 2003.
[62] T. Fujitani and J. Nakamura, “The effect of ZnO in methanol synthesis catalysts on Cu dispersion and the specific activity,” *Catalysis Letters*, vol. 56, pp. 119–124, Dec. 1998.
[63] E. L. Kunkes, “Hydrogenation of CO2 to methanol and CO on Cu/ZnO/Al2O3: Is there a common intermediate or not?,” *Journal of Catalysis*, p. 6, 2015.
[64] K. A. Ali, A. Z. Abdullah, and A. R. Mohamed, “Recent development in catalytic technologies for methanol synthesis from renewable sources: A critical review,” *Renewable and Sustainable Energy Reviews*, vol. 44, pp. 508–518, Apr. 2015, doi: 10.1016/j.rser.2015.01.010.
[65] X.-M. Liu, G. Q. Lu, Z.-F. Yan, and J. Beltramini, “Recent Advances in Catalysts for Methanol Synthesis via Hydrogenation of CO and CO $_2$,” *Ind. Eng. Chem. Res.*, vol. 42, no. 25, pp. 6518–6530, Dec. 2003, doi: 10.1021/ie020979s.
[66] M. Behrens, “Meso- and nano-structuring of industrial Cu/ZnO/(Al2O3) catalysts,” *Journal of Catalysis*, vol. 267, no. 1, pp. 24–29, Oct. 2009, doi: 10.1016/j.jcat.2009.07.009.
[67] I. Kasatkin, P. Kurr, B. Kniep, A. Trunschke, and R. Schlögl, “Role of Lattice Strain and Defects in Copper Particles on the Activity of Cu/ZnO/Al2O3 Catalysts for Methanol Synthesis,” *Angew. Chem. Int. Ed.*, vol. 46, no. 38, pp. 7324–7327, Sep. 2007, doi: 10.1002/anie.200702600.
[68] T. Lunkenbein, J. Schumann, M. Behrens, R. Schlögl, and M. G. Willinger, “Formation of a ZnO Overlayer in Industrial Cu/ZnO/Al $_2$ O $_3$ Catalysts Induced by Strong Metal-Support Interactions,” *Angew. Chem. Int. Ed.*, vol. 54, no. 15, pp. 4544–4548, Apr. 2015, doi: 10.1002/anie.201411581.
[69] I. Nakamura, H. Nakano, T. Fujitani, T. Uchijima, and J. Nakamura, “Evidence for a special formate species adsorbed on the Cu–Zn active site for methanol synthesis,” *Surface Science*, vol. 402–404, pp. 92–95, May 1998, doi: 10.1016/S0039-6028(97)00910-2.
[70] T. Fujitani, I. Nakamura, T. Uchijima, and J. Nakamura, “The kinetics and mechanism of methanol synthesis by hydrogenation of CO2 over a Zn-deposited Cu(111) surface,” *Surface Science*, vol. 383, no. 2–3, pp. 285–289, 1997.
[71] M. M. Günter *et al.*, “Implication of the microstructure of binary Cu/ZnO catalysts for their catalytic activity in methanol synthesis”.
[72] R. Burch, S. E. Golunski, and M. S. Spencer, “The role of copper and zinc oxide in methanol synthesis catalysts,” *Faraday Trans.*, vol. 86, no. 15, p. 2683, 1990, doi: 10.1039/ft9908602683.

[73] T. Fujitani and J. Nakamura, “The effect of ZnO in methanol synthesis catalysts on Cu dispersion and the specific activity,” *Catalysis Letters*, vol. 56, pp. 119–124, Dec. 1998.
[74] G. H. Graaf, E. J. Stamhuis, and A. A. C. M. Beenackers, “Kinetics of low-pressure methanol synthesis,” *Chemical Engineering Science*, vol. 43, no. 12, pp. 3185–3195, 1988, doi: 10.1016/0009-2509(88)85127-3.
[75] K. M. V. Bussche and G. F. Froment, “A Steady-State Kinetic Model for Methanol Synthesis and the Water Gas Shift Reaction on a Commercial Cu/ZnO/Al2O3Catalyst,” *Journal of Catalysis*, vol. 161, no. 1, pp. 1–10, Jun. 1996, doi: 10.1006/jcat.1996.0156.
[76] G. H. Graaf, H. Scholtens, E. J. Stamhuis, and A. A. C. M. Beenackers, “Intra-particle diffusion limitations in low-pressure methanol synthesis,” *Chemical Engineering Science*, vol. 45, no. 4, pp. 773–783, 1990, doi: 10.1016/0009-2509(90)85001-T.
[77] G. H. Graaf, P. J. J. M. Sijtsema, E. J. Stamhuis, and G. E. H. Joosten, “Chemical equilibria in methanol synthesis,” *Chemical Engineering Science*, vol. 41, no. 11, pp. 2883–2890, 1986, doi: 10.1016/0009-2509(86)80019-7.
[78] A. Y. Rozovskii, “Modern problems in the synthesis of methanoi,” *Russian Chemical Reviews*, 1989.
[79] “FactSage.” Thermfact Ltd in collaboration with CRCT and GTT-Technologies. [Online]. Available: https://www.factsage.com/
[80] A. De Visscher, “CALCULATION OF COMPLEX CHEMICAL EQUILIBRIA,” in *Lecture Notes in Chemical Engineering Kinetics and Chemical Reactor Design.*, Charleston: Self-Published, 2013.
[81] H. S. Fogler, *Elements of chemical reaction engineering*, 4th ed. in Prentice Hall PTR international series in the physical and chemical engineering sciences. Upper Saddle River, NJ: Prentice Hall PTR, 2006.
[82] R. H. Perry and D. W. Green, Eds., *Perry’s chemical engineers’ handbook*, 8th ed. New York: McGraw-Hill, 2008.
[83] S. M. Walas, *Reaction kinetics for chemical engineers*. in Butterworths series in chemical engineering. Boston: Butterworths, 1989.
[84] T. A. Adams, *Learn Aspen Plus in 24 hours*. New York: McGraw Education, 2018.
[85] “ASPEN PLUS® User Guide”.
[86] K. I. M. Al-Malah, *Aspen plus: chemical engineering applications*. Hoboken, New Jersey: Wiley, 2017.
[87] Y. Khojasteh-Salkuyeh, O. Ashrafi, E. Mostafavi, and P. Navarri, “CO2 utilization for methanol production; Part I: Process design and life cycle GHG assessment of different pathways,” *Journal of CO2 Utilization*, vol. 50, p. 101608, Aug. 2021, doi: 10.1016/j.jcou.2021.101608.

APPENDICES (OPTIONAL)

Appendix. A

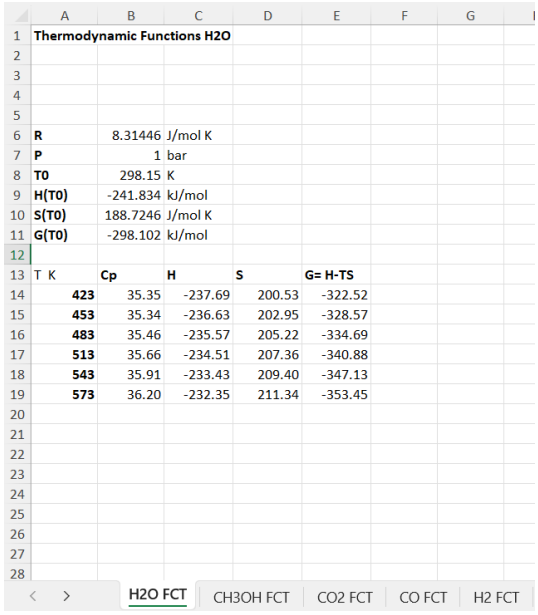

	A	B	C	D	E	F	G
1	**Thermodynamic Functions H2O**						
2							
3							
4							
5							
6	**R**	8.31446	J/mol K				
7	**P**	1	bar				
8	**T0**	298.15	K				
9	**H(T0)**	-241.834	kJ/mol				
10	**S(T0)**	188.7246	J/mol K				
11	**G(T0)**	-298.102	kJ/mol				
12							
13	**T K**	**Cp**	**H**	**S**	**G= H-TS**		
14	**423**	35.35	-237.69	200.53	-322.52		
15	**453**	35.34	-236.63	202.95	-328.57		
16	**483**	35.46	-235.57	205.22	-334.69		
17	**513**	35.66	-234.51	207.36	-340.88		
18	**543**	35.91	-233.43	209.40	-347.13		
19	**573**	36.20	-232.35	211.34	-353.45		
20							
21							
22							
23							
24							
25							
26							
27							
28							

H2O FCT | CH3OH FCT | CO2 FCT | CO FCT | H2 FCT

Figure 47-Thermodynamic functions of H_2O calculated via Fact Sage

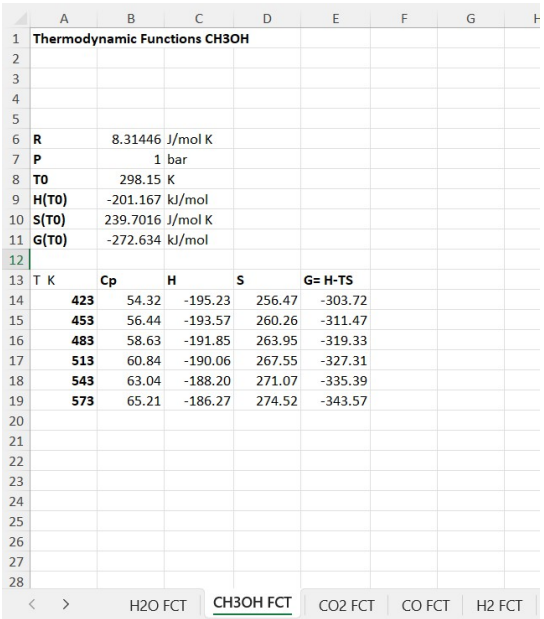

	A	B	C	D	E	F	G
1	**Thermodynamic Functions CH3OH**						
2							
3							
4							
5							
6	**R**	8.31446	J/mol K				
7	**P**	1	bar				
8	**T0**	298.15	K				
9	**H(T0)**	-201.167	kJ/mol				
10	**S(T0)**	239.7016	J/mol K				
11	**G(T0)**	-272.634	kJ/mol				
12							
13	**T K**	**Cp**	**H**	**S**	**G= H-TS**		
14	**423**	54.32	-195.23	256.47	-303.72		
15	**453**	56.44	-193.57	260.26	-311.47		
16	**483**	58.63	-191.85	263.95	-319.33		
17	**513**	60.84	-190.06	267.55	-327.31		
18	**543**	63.04	-188.20	271.07	-335.39		
19	**573**	65.21	-186.27	274.52	-343.57		
20							
21							
22							
23							
24							
25							
26							
27							
28							

H2O FCT | CH3OH FCT | CO2 FCT | CO FCT | H2 FCT

Figure 48-Thermodynamic functions of CH_3OH calculated via Fact Sage

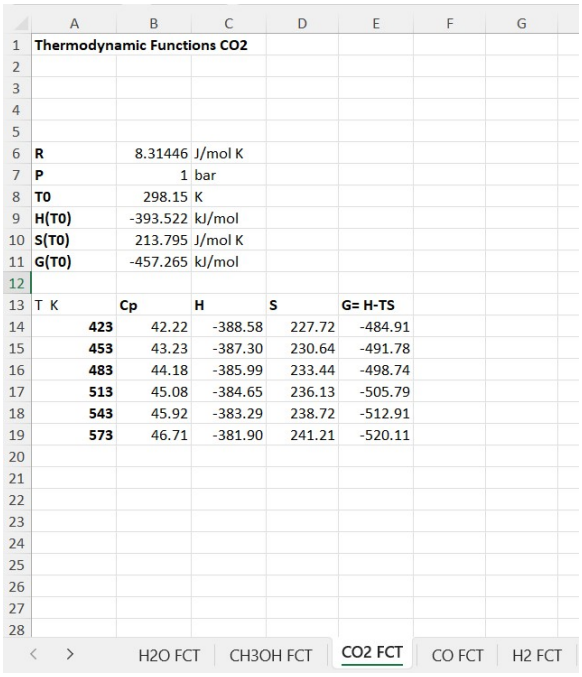

	A	B	C	D	E	F	G
1	**Thermodynamic Functions CO2**						
2							
3							
4							
5							
6	**R**	8.31446	J/mol K				
7	**P**	1	bar				
8	**T0**	298.15	K				
9	**H(T0)**	-393.522	kJ/mol				
10	**S(T0)**	213.795	J/mol K				
11	**G(T0)**	-457.265	kJ/mol				
12							
13	T K	**Cp**	**H**	**S**	**G= H-TS**		
14	**423**	42.22	-388.58	227.72	-484.91		
15	**453**	43.23	-387.30	230.64	-491.78		
16	**483**	44.18	-385.99	233.44	-498.74		
17	**513**	45.08	-384.65	236.13	-505.79		
18	**543**	45.92	-383.29	238.72	-512.91		
19	**573**	46.71	-381.90	241.21	-520.11		
20							
21							
22							
23							
24							
25							
26							
27							
28							

H2O FCT | CH3OH FCT | **CO2 FCT** | CO FCT | H2 FCT

Figure 49-Thermodynamic functions of CO_2 calculated via Fact Sage

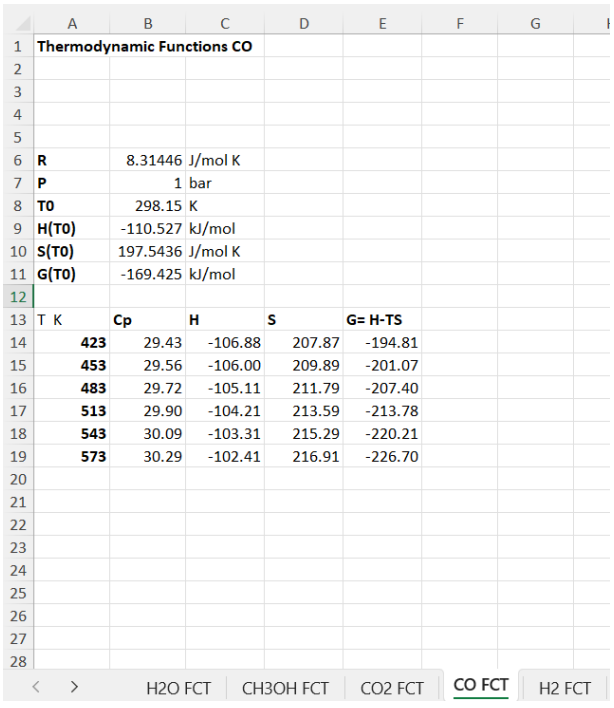

	A	B	C	D	E	F	G
1	**Thermodynamic Functions CO**						
2							
3							
4							
5							
6	**R**	8.31446	J/mol K				
7	**P**	1	bar				
8	**T0**	298.15	K				
9	**H(T0)**	-110.527	kJ/mol				
10	**S(T0)**	197.5436	J/mol K				
11	**G(T0)**	-169.425	kJ/mol				
12							
13	T K	**Cp**	**H**	**S**	**G= H-TS**		
14	**423**	29.43	-106.88	207.87	-194.81		
15	**453**	29.56	-106.00	209.89	-201.07		
16	**483**	29.72	-105.11	211.79	-207.40		
17	**513**	29.90	-104.21	213.59	-213.78		
18	**543**	30.09	-103.31	215.29	-220.21		
19	**573**	30.29	-102.41	216.91	-226.70		
20							
21							
22							
23							
24							
25							
26							
27							
28							

H2O FCT | CH3OH FCT | CO2 FCT | **CO FCT** | H2 FCT

Figure 50-Thermodynamic functions of CO calculated via Fact Sage

	A	B	C	D	E	F	G	H
1	**Thermodynamic Functions H2**							
2								
3								
4								
5								
6	**R**	8.31446	J/mol K					
7	**P**	1	bar					
8	**T0**	298.15	K					
9	**H(T0)**	0	kJ/mol					
10	**S(T0)**	130.5706	J/mol K					
11	**G(T0)**	-38.9296	kJ/mol					
12								
13	T K	**Cp**	**H**	**S**	**G= H-TS**			
14	**423**	29.21	3.63	140.85	-55.95			
15	**453**	29.23	4.51	142.85	-60.20			
16	**483**	29.25	5.39	144.73	-64.52			
17	**513**	29.26	6.26	146.49	-68.88			
18	**543**	29.28	7.14	148.15	-73.30			
19	**573**	29.30	8.02	149.73	-77.77			
20								
21								
22								
23								
24								
25								
26								
27								
28								

H2O FCT | CH3OH FCT | CO2 FCT | CO FCT | H2 FCT

Figure 51-Thermodynamic functions of H_2 calculated via Fact Sage

	A	B	C	D	E	F	G	H
1	**Equilibrium Calculations for Methanol Synthesis**							
2								
3	T	483	K					
4	p	40	bar					
5	R	8.31446	J/mol K					
6								
7	CO2	1						
8	CO	0						
9	H2	3						
10	H2O	0						
11	Sum	4		kJ/mol	**From delta G0**		**From partial pressures**	
12	#	**Reaction**		**delta G0**	K	ln K	ln K pred	Difference
13	1	CO2+3H2=CH3OH+H2O		3.83E+01	7.28252E-05	-9.52745	-9.527448055	-5.1989E-11
14	2	CO2+H2=CO+H2O		-2.12E+01	194.4405514	5.27013	5.270126468	0
15								
16								
17								
18	**mole**	**ln n**	**n**	**Partial Pressure**				
19	CO	-3.56117	2.84E-02	3.26E-01	C balance	8.24E-09		
20	CO2	-0.3355	7.15E-01	8.20E+00	H Balance	-5.09E-08		
21	CH3OH	-1.36018	2.57E-01	2.94E+00	O Balance	-1.37E-09		
22	H2	0.78925	2.20E+00	2.53E+01				
23	H2O	-1.2552	2.85E-01	3.27E+00				
24	Sum		3.49E+00	4.00E+01				
25								

Equilibrium Constant (40,483) | Equilibrium Constant (40,513) | Equilibrium Constant (40,543) | Equilibrium C

Solver Parameters

Set Objective: $H$13

To: Max Min Value Of: 0

By Changing Variable Cells: $B$19:$B$23

Subject to the Constraints:

$F$19 = 0
$F$20 = 0
$F$21 = 0
$H$14 = 0

Add | Change | Delete | Reset All | Load/Save

Make Unconstrained Variables Non-Negative

Select a Solving Method: GRG Nonlinear | Options

Solving Method

Select the GRG Nonlinear engine for Solver Problems that are smooth nonlinear. Select the LP Simplex engine for linear Solver Problems, and select the Evolutionary engine for Solver problems that are non-smooth.

Help | Solve | Close

Figure 52-Excel Solver configuration to solve the full equilibrium problem by fitting equilibrium constants at T= 483 K and P= 40 bars

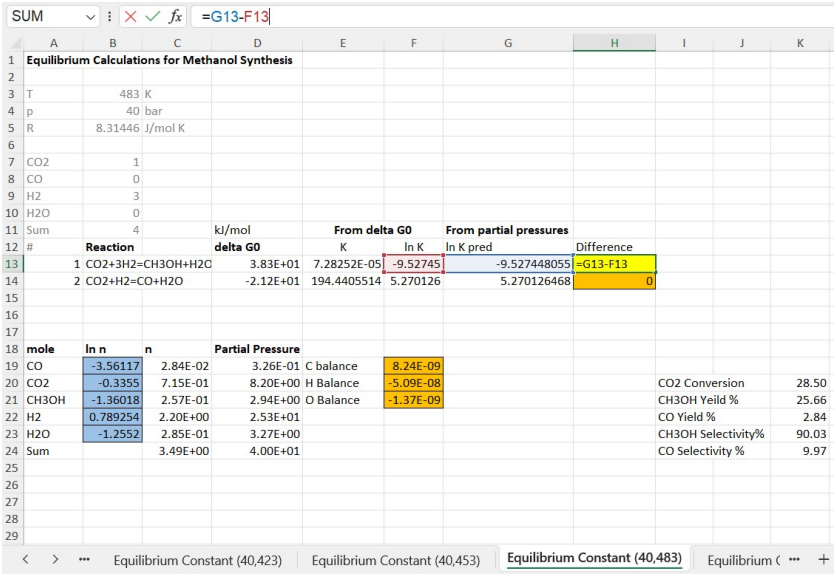

Figure 53-Full equilibrium calculation and results based on fitting equilibrium constants at T= 483 K and P= 40 bars

Appendix. B

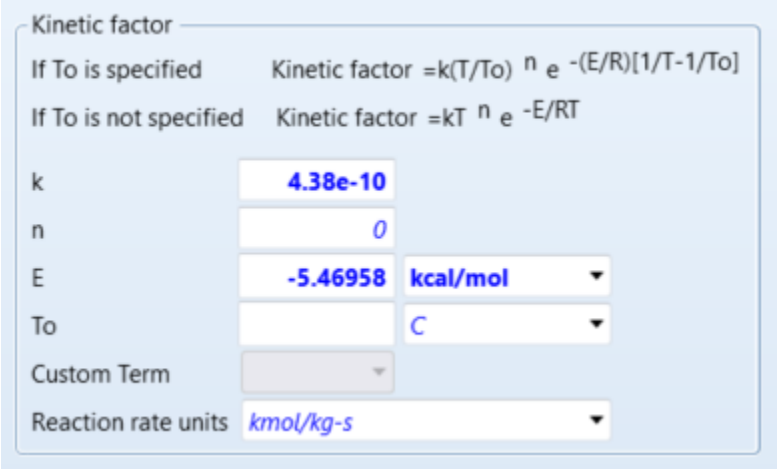

Figure 54-Kinetic Factor expression for the CO2 hydrogenation reaction

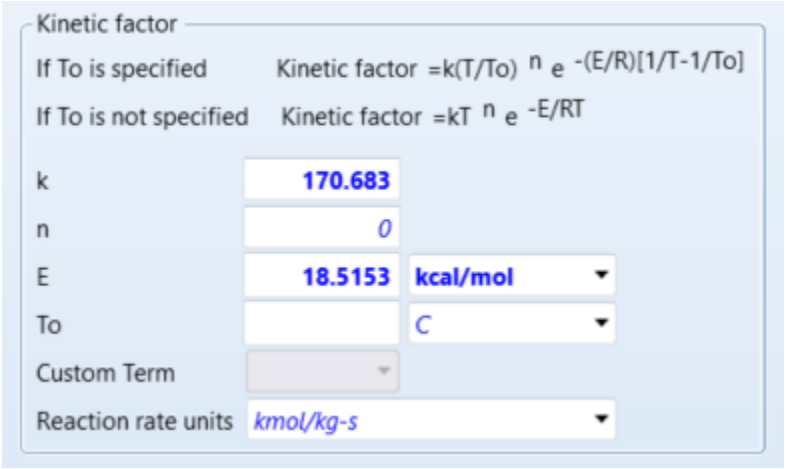

Figure 55-Kinetic Factor expression for the RWGS reaction

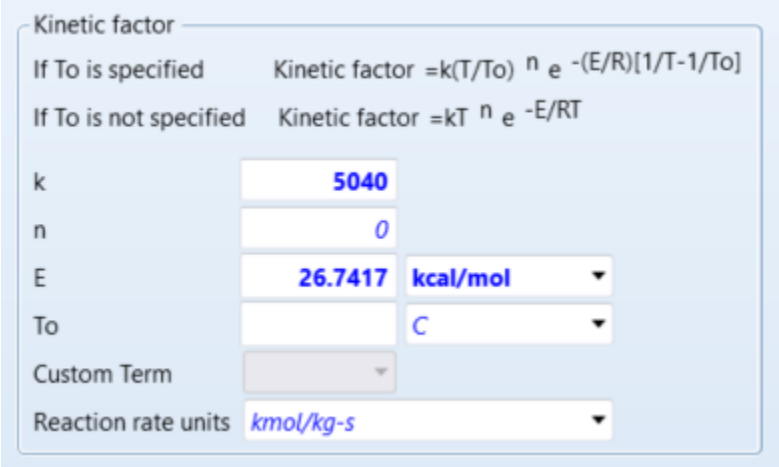

Figure 56-Kinetic Factor expression for the CO hydrogenation reaction

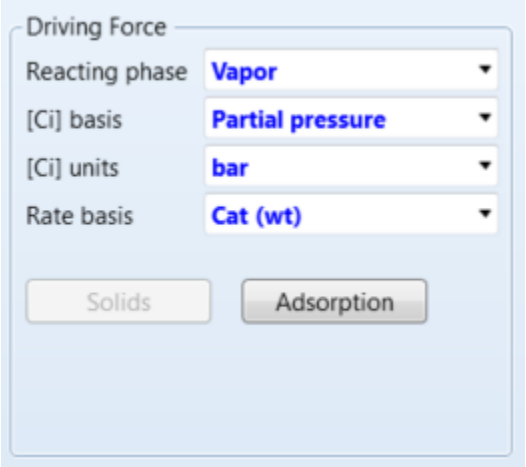

Figure 57-The reacting phase and rate basis considerations for the driving force in Aspen Plus.

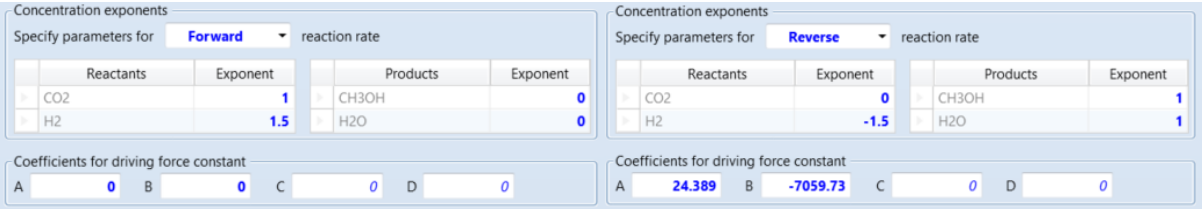

Figure 58-The driving force expression in Aspen Plus for the forward and backward direction of the CO2 hydrogenation reaction.

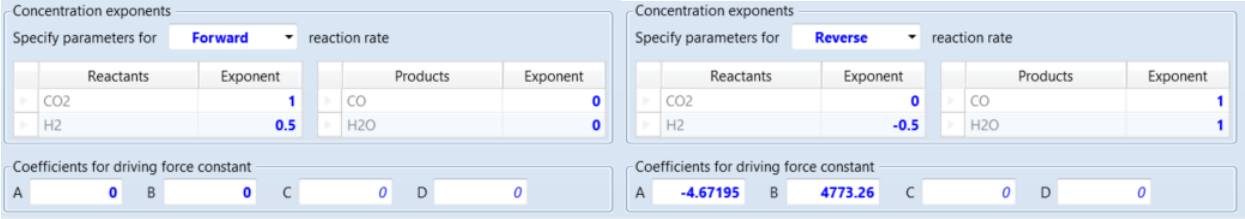

Figure 59-The driving force expression in Aspen Plus for the forward and backward direction of the RWGS reaction.

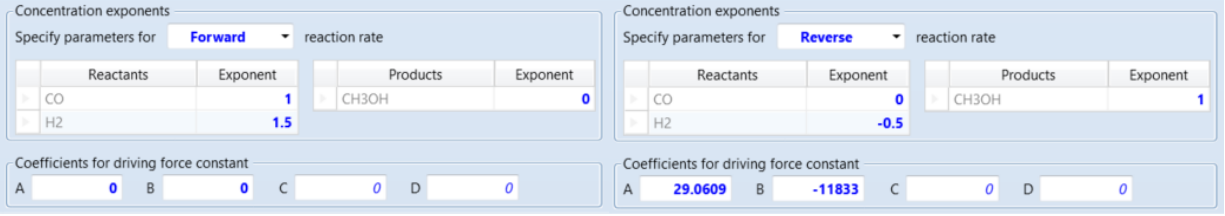

Figure 60-The driving force expression in Aspen Plus for the forward and backward direction of the CO hydrogenation reaction.

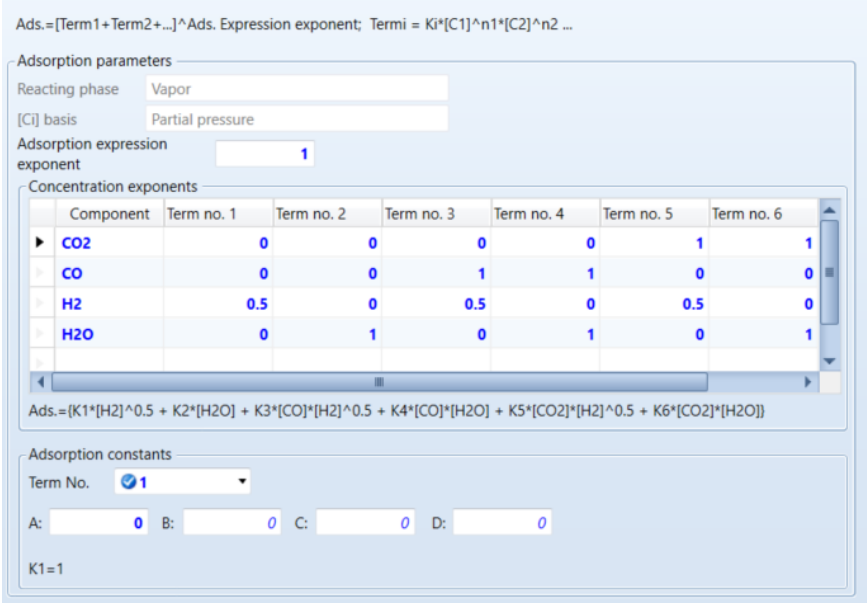

Figure 61-Adsorption expression representation in Aspen Plus.

As can be seen in Figure 60, the concentration exponents are deduced from the partial pressure (P_i) in the adsorption expression, and the adsorption coefficients A, B, C, and D for "Term no. 1" up to "Term no. 6" are evaluated by taking the logarithmic value of each adsorption term (b_i) found in our adsorption expression.

Table 58-Another Kinetic Model for the CO_2 hydrogenation considering all three reactions.

Kinetic Parameters	Values	Units
K_1	4.43E-10	(kmol/kg· s)
K_2	171	(kmol/kg· s)
K_3	5040	(kmol/kg· s)
E_1	-5.67487718	kcal/mol
E_2	18.5738751	kcal/mol
E_3	26.760958351	kcal/mol